Stony Brook University

OFFICIAL COPY

The official electronic file of this thesis or dissertation is maintained by the University Libraries on behalf of The Graduate School at Stony Brook University.

© All Rights Reserved by Author.

Solid State NMR and Pair Distribution Function Studies of Silicon Electrodes for Lithium-Ion Batteries

A Dissertation Presented

by

Baris Key

to

The Graduate School

in Partial Fulfillment of the Requirements

for the Degree of

Doctor of Philosophy

in

Chemistry

Stony Brook University

December 2010

Stony Brook University

Baris Key

We, the dissertation committee for the above candidate for the **Doctor of Philosophy** degree, hereby recommend acceptance of this dissertation.

Clare P. Grey, Ph. D., Advisor

Professor, Department of Chemistry, Stony Brook University

John B. Parise, Ph. D., Chairperson

Professor, Department of Geosciences, Stony Brook University

Benjamin Hsiao, Ph. D., Third Member

Professor, Department of Chemistry, Stony Brook University

John T. Vaughey, Ph. D., Outside Member

Research Team Leader, Chemical Sciences and Engineering Department, Argonne National Laboratory

This dissertation is accepted by the Graduate School.

Lawrence Martin

Dean of the Graduate School

Abstract of the Dissertation

Solid State NMR and Pair Distribution Function Studies of Silicon Electrodes for Lithium-Ion Batteries

by

Baris Key

Doctor of Philosophy

in

Chemistry

Stony Brook University

2010

The universally used negative electrode material in a LIB is carbon, because of its moderate capacity (372 $mAhg^{-1}$ for graphite), cyclability and high rate capability. However, new, low cost, safe electrode materials with higher capacities are still urgently required for both portable and transportation applications. Silicon anodes are particularly attractive alternatives to carbon with extremely high gravimetric energy densities (3572 $mAhg^{-1}$). Compared to graphite, silicon has a massive volumetric capacity of 8322 $mAhcm^{-3}$ (calculated based on the original volume of silicon) which is approximately ten times that graphite. At room temperature, upon electrochemical lithiation, silicon undergoes a crystalline to amorphous phase transition forming a lithiated amorphous silicide phase. Unfortunately, due to the amorphous nature of the lithiated silicides, it is not possible to monitor all the structural changes that occur during lithium insertion/removal with conventional methods such as diffraction. The short range order of the amorphous materials remains unknown, preventing attempts to optimize performance based on electrochemical-structure correlations. In this work, a combination of local structure probes, *ex-situ* ^{7}Li nuclear magnetic resonance (NMR) studies and pair distribution function (PDF) analysis of X-ray data was applied to investigate the changes in short range order that occur during the initial charge and discharge cycles. The distinct electrochemical profiles observed subsequent to the 1st discharge have been shown to be associated with the formation of distinct amorphous lithiated silicide structures. A (de)lithiation model consisting of four different mechanisms, each being valid for regions of the charge or discharge process is proposed to explain the hysteresis and the steps in the electrochemical profile observed during lithiation and delithiation of Si. A spontaneous reaction of the fully lithiated lithium silicide with the electrolyte is directly observed in the *in situ* NMR experiments; this mechanism results in self-discharge, and potentially capacity loss. The rate of this self-discharge process is much slower when CMC (carboxymethylcellulose) is used as the binder.

Previous work has shown that the electrochemical performance of nanoparticulate crystalline silicon is different from the bulk. The lithiation and delithiation mechanisms of nano-Si for lithium ion batteries are studied by using ex-situ solid state MAS NMR and PDF analysis. The main differences vs. bulk lithiation and delithiation are identified by characterizing the amorphous phases formed.

Table of Contents

List of Abbreviations

2D, 3D	two-dimensional, three-dimensional
BMS	bulk magnetic susceptibility
Carbon SP	carbon super P
C_2mIm	1-ethyl-3-methylimidazolium tetrafluoroborate
C_4mpyr TFSI	butyl-methylpyrrolidinium bis(trifluoromethanesulfonyl)imide
CMC	carboxymethyl cellulose
CMX	chemmagnetics
CPMG	carr purcells meibohm gill
CSIRO	commonwealth scientific and industrial research organization
CT	central transition
DBP	dibutyl phtalate
DFT	density functional theory
DMC	dimethyl carbonate
DOS	density of states
EC	ethylene carbonate
EFG	electric field gradient
EV	electric vehicle
EXAFS	extended X-ray absorption fine structure
FWHM	full width at half maximum
GITT	galvanostatic intermittent titration technique
HEV	hybrid electric vehicle
IP	image plate
LIB	Li-ion battery
MAS	magic angle spinning
MCMB	mesocarbon microbeads
ND	neutron diffraction
NMR	nuclear magnetic resonance
OCV	open circuit voltage
PC	propylene carbonate

PDF	pair distribution function
PHEV	plug-in hybrid electric vehicle
PTFE	polytetrafluoroethylene
PVDF	poly-vinylidene fluoride
QCC	quadrupolar coupling constant
RF	radio frequency
RMC	reverse Monte Carlo
SEI	solid electrolyte interphase
SEM	scanning electron microscopy
SOC	state of charge
SS	solid-state
TIP	temperature independent paramagnetism
TFSI	bis(trifluoromethanesulfonyl)imide
TMS	tetramethylsilane
VC	vinyldene carbonate
VSP	biologic potentiostat/galvanostat
XRD	X-ray diffraction

List of Symbols

α, β, γ	unit cell angles
$\delta, \delta^{'}$	non-stoichiometry variable
η	asymmetry parameter
λ	radiation wavelength
μ_0	permeability of the vacuum
μ_r	relative permeability of the metal
$\vec{\mu}_e$	magnetic moment of the unpaired electron
ν_r	rotor (sample) spinning frequency, s^{-1}
ω_0	Larmor frequency
ω_1	radio frequency strength
$\omega(x)$	field strength inside a metal
ρ	resistivity of the metal
$\rho\ (0)$	electron spin density at the observed nucleus
$\rho\ (r)$	microscopic pair density
ρ_{Li}	density of Li metal
χ_p	Pauli susceptibility
θ	diffracted angle
τ	duration variable in NMR timescale
τ_p	pulse width (radiofrequency duration)
Ω	volume per electron
a, b, c	unit cell parameters
B_0	external applied magnetic field strength
b_i,b_j	scattering length and the atomic factor at a given Q
C	coulomb
c_{ij}	occupational correlation coefficient between atoms i and j
C/h	charge or discharge rate
C_{th}	theoretical specific capacity
d_{hkl}	interplanar spacing
F	Faraday constant

f	frequency of the applied rf field
F_{hkl}	structure factor of *hkl* reflection
f_i	scattering power of the atom *i*
$G(r)$	pair distribution function
h	Planck's constant
h, k, l	Miller indices
I	nuclear spin number
I_μ	NMR signal intensity due to microstructure
$I_c(t)$	current at time t
I_{hkl}	intensity of the *hkl* reflection
$I(t)$	fractional change of NMR signal intensity
$I_{vol}(t)$	NMR signal intensity proportional to volume
K	Knight shift
M	molecular weight
M_μ	mass of microstructure
$M_{Li}(t)$	mass of lithium at time t
M_{SD}	mass of smoothly deposited or stripped metal
N_0	Avogadro's number
Q	magnitude of the scattering vector
R_{wp}	weighted profile *R*-factor
S	NMR signal intensity
S_0	NMR signal per unit volume of the metal
S_{bulk}	NMR signal from the entire volume of the metal
S_μ	NMR signal internsity from the microstructure
$S(Q)$	normalized scattering intensity
T_1	spin-lattice relaxation rate
U_{iso}	isotropic displacement parameter
U, V, W	Gaussian profile parameters
$V_\mu(t)$	total volume of the lithium microstructure
V_{xx}, V_{yy}, V_{zz}	principle components of the EFG tensor
X, Y	Lorentzian profile parameters

x, y, z	fractional atomic coordinates

List of Figures

Chapter 1

Chapter 2

Chapter 3

Chapter 4

Chapter 5

Acknowledgements

First and foremost, I would like to thank my advisor, Professor Clare P. Grey, for her guidance, vision and endless support. The time I've spent working with her as a graduate student contributed immensely to the foundations of the scientist I wish to become.

I also wish to thank my committee members: Professors John B. Parise, Benjamin Hsiao and Dr. John T. Vaughey for their encouragement and constructive criticism.

Jean-Marie Tarascon, Mathieu Morcrette and Adam S. Best, are acknowledged for fruitful discussions and collaborations. I am thankful for the assistance from the beamline scientists: Peter J. Chupas, Karena Chapman and John T. Vaughey, Christopher S. Johnson and Michael M. Thackeray (Argonne National Laboratory). The US Department of Energy, Office of FreedomCAR and Vehicle Technologies and NYSTAR have provided the financial support.

I would also like to thank the past and present group members: Won-Sub Yoon, Jordi Cabana Jiménez, Peter J. Chupas, Julien Breger, Meng Jiang, Paul Sideris, Hailong Chen, Nicole Trease, Rosa Robert, Riza Dervisoglu. I especially thank to Rangeet Bhattacharyya and Thomas Koester for their great help and support.

I also wish to thank SB Tennis Club to introduce a great sport into my life and keep me sane throughout my graduate studies.

Finally I would like to thank to my family back in Turkey for all their support and sacrifice, and to my dear wife, Fulya Dogan Key, who is also my colleague, friend, spouse and life. Thank you for being there for me, as I will always be there for you.

List of Publications

1. “Solid State NMR and PDF Studies on Nanoparticulate Crystalline Silicon” Key, B., Morcrette, M., Tarascon, J. M., and Grey, C. P., **2010**, manuscript in preparation

   basis of Chapter 4

2. “Pair Distribution Function Analysis and Solid State NMR studies of Silicon Electrodes for Lithium-ion Batteries: Understanding the (De)lithiation Mechanisms” Key, B., Morcrette, M., Tarascon, J. M., and Grey, C. P., **2010**, accepted to *Journal of the American Chemical Society*

   basis of Chapter 3

3. “*In situ* NMR Observation of the Formation of Metallic Microstructures in Lithium Batteries” Bhattacharyya, R., Key, B., Chen, H., Best, A. S., Hollenkamp, A. F., and Grey, C. P., **2010**, *Nature Materials*, 9, 504-510

   basis of Chapter 5

4. “Real-Time NMR Investigations of Structural Changes in Silicon Electrodes for Lithium-Ion Batteries” Key, B., Bhattacharyya, R., Morcrette, M., Seznec, V., Tarascon, J. M., and Grey, C. P., **2009**, *Journal of the American Chemical Society*, 131, 9239-9249

   basis of Chapter 3

5. “Electrochemical and Structural Study of the Layered, “Li-Excess” Lithium-Ion Battery Electrode Material $Li[Li_{1/9}Ni_{1/3}Mn_{5/9}]O_2$” Jiang, M., Key, B., Meng, Y. S., and Grey, C. P., **2009**, *Chemistry of Materials*, 21, 2733-2745

6. “Identifying the Local Structures Formed during Lithiation of the Conversion Material, Iron Fluoride, in a Li Ion battery: A Solid State NMR, X-ray Diffraction, and Pair Distribution Function Analysis Study” Yamakawa, N., Jiang, M., Key, B., and Grey, C. P., **2009**, *Journal of the American Chemical Society*, 131, 10525-10536

Chapter 1

Introduction

1. Motivation

Electrochemical cells and batteries are defined as primary (non-rechargeable, such as alkaline batteries) or secondary (rechargeable). Secondary batteries (such as Ni-Cd, Ni-MH and Li-ion) present high power densities and good temperature performances. Except for the Li-ion batteries (LIBs), their energy densities are poor compared to primary battery systems. Indeed, the LIBs can store more than twice the energy of other cells of the same mass and size, as shown in Figure 1.1 [1]. Therefore, the LIB technology is nowadays considered as one of the most advanced energy storage systems, and for this reason it has received a lot of attention in the past two decades. Rechargeable lithium-ion batteries are currently the most preferred energy storage devices in portable electronic devices, with the highest gravimetric and volumetric energy densities[1]. Their potential use in hybrid and plug-in hybrid electric vehicles, and all-electric vehicles (HEVs, PHEVs and EVs) make advances in this field the more significant, due to both economic and environmental implications. The universally used negative electrode material in a LIB is carbon, because of its moderate capacity (372 mAhg^{-1} for graphite), cyclability and high rate capability. However, new, low cost, safe electrode materials with higher capacities are still urgently required for both portable and transportation applications. To this end, Sn-based anodes with large theoretical volumetric and gravimetric capacities have recently been commercialized in Sony's NEXELION^{TM} cells. Silicon anodes are particularly attractive alternatives to carbon with extremely high gravimetric energy densities (3572 mAhg^{-1}). Compared to graphite, silicon has a massive volumetric capacity of 8322 mAhcm^{-3} (calculated based on the original volume of silicon) which is approximately ten times that graphite. However, the unusually high capacity is associated with large electrode volume changes of up to 300%, resulting in particle fracture and capacity retention issues, along with design challenges, since the expansion has to be managed in the cell.

At room temperature, silicon does not form any of the thermodynamically stable crystalline lithium silicide phases on electrochemical lithiation, but instead undergoes a crystalline to amorphous phase transition forming a lithiated amorphous silicide phase. This phase then recrystallizes at deep discharge to form a metastable phase, $Li_{15}Si_4$, which is isostructural to the thermodynamic phase $Li_{15}Ge_4$ [2]. This final composition provides the theoretical capacity of 3.75 Li per Si (3572 mAh/g). Interestingly, lithiated nanoparticles of crystalline and amorphous thin films less than 2µm thickness of silicon do not recrystallize at deep discharge[3,4]. Unfortunately, due to the amorphous nature of the lithiated silicides, it is not possible to monitor all the structural changes that occur during lithium insertion/removal with conventional methods such as diffraction. The short range order of the amorphous materials remains unknown, preventing attempts to optimize performance based on electrochemical-structure correlations. This close relation is the main motivation of the thesis work.

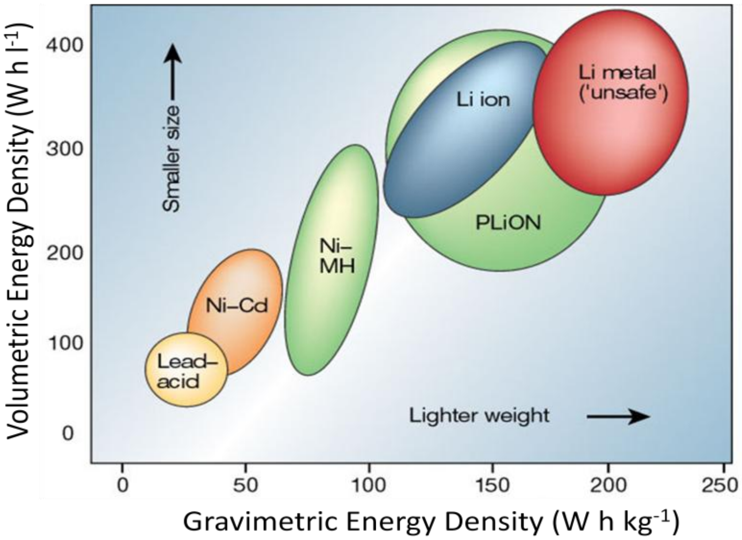

Figure 1.1. Comparison of the different battery technologies in term of volumetric and gravimetric energy densities (figure taken from reference [1])

The electrochemical performance of the battery is closely linked to the chemistry, i.e. the mechanism of lithiation and delithiation of the materials that are composing the electrodes. In this section, how a typical lithium electrochemical cell works will be explained and brief overview of available chemistries, specifically, negative electrodes will be given. Silicon as a high energy density negative electrode will be introduced and the importance of understanding the mechanism of lithiation and delithiation for the future commercialization of silicon for high energy negative electrodes for advanced lithium ion batteries will be explained.

1.1. Electrochemical Li Cells

A battery is a device that consists of several electrochemical cells which are connected in parallel and/or in series, to deliver the required capacity and voltage. It converts stored chemical energy into electrical energy, due to an electrochemical redox reaction. Each cell is composed of a positive electrode (or cathode), which is oxidized during the electrochemical reaction upon charge and a negative electrode (or anode), which is reduced during the reaction upon charge. These two electrodes are separated by an electrolyte, a non-aqueous ionic conductor in the case of a Li-ion battery containing dissociated salts, allowing the transfer of ions between the electrodes.

Figure 1.2 illustrates the electrochemical operation of a “rocking-chair” type battery during a charge or a discharge. In the case of the Sony cell, the two electrodes (graphite as negative and $LiCoO_2$ as positive) are separated by an electrolyte such as $LiPF_6$, dissolved in a non-aqueous solvent (for instance, ethylene carbonate, dimethyl carbonate or a combination of more than one organic carbonate). During the charge, an external power supply is used to increase the electrochemical potential of Li at the positive electrode. The Li ions are deintercalated from the positive electrode ($LiCoO_2$), diffuse through the electrolyte and are intercalated between the carbon layers in the negative electrode. In this case, this is accompanied by the oxidation of Co (from Co^{+3} to Co^{+4}) and the formation of $Li_{1-x}CoO_2$ ($0<x<1$). However the intercalation mechanism can be replaced by insertion mechanisms in cases of different battery chemistries as in the case of silicon negative electrode.

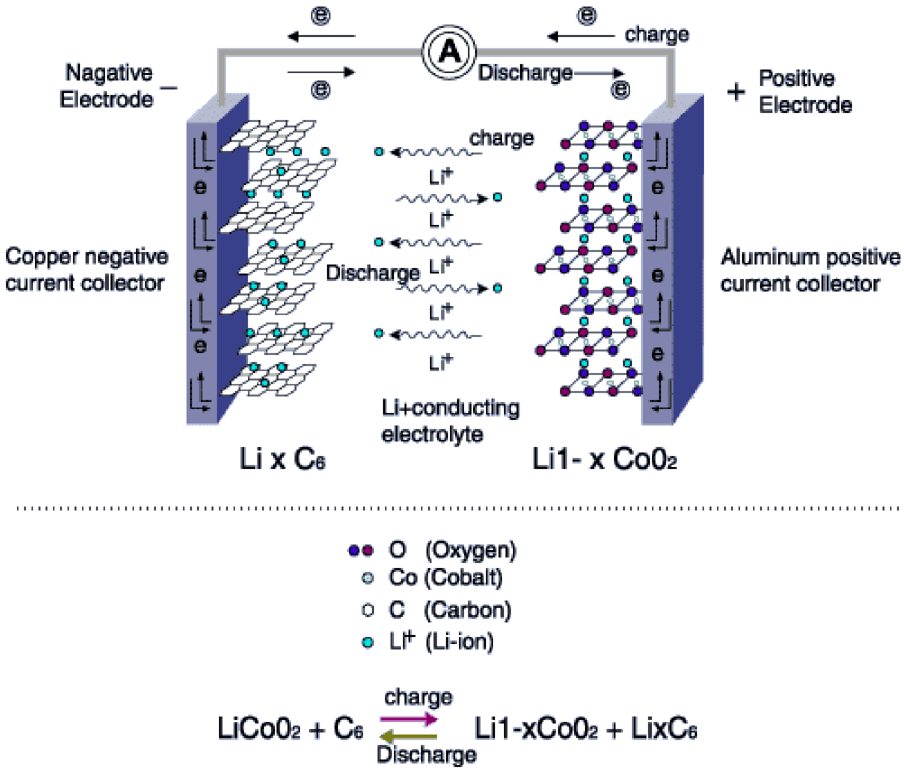

Figure 1.2. Electrochemical operation of a rechargeable Li-ion cell during charge and discharge with $LiCoO_2$ as positive electrode and graphite as negative electrode [5].

Discharge reverses this process, allowing the reformation of $LiCoO_2$. This process requires an equivalent number of e^- passing around the external circuit to the positive electrode, reducing the transition metal, with a release of electrical energy. Thus, the battery is, in this case, referred to as “rechargeable” because this process is reversible and the chemical energy can be restored by supplying electric power upon charge.

The choice of electrode materials is important since it will have an effect on the performance of the cell. The main criteria for a good electrode material are [6,7]:

- High gravimetric energy density (low formula mass)
- High volumetric energy density (low molar volume)
- High rate capability (power density)
- Long cycle life (reversibility of the process)
- Low cost
- Safety

- Low toxicity

The gravimetric (or volumetric) energy density is defined as the energy per unit weight in Whkg^{-1} (or per unit volume in WhL^{-1}). This is equal to the product of the cell voltage and the specific capacity. Therefore, these two key parameters also need to be high.

The cell voltage is given by the difference in the electrochemical potentials of Li between the two electrodes. Usually, transition metal oxides, which are used as intercalation compounds for the positive electrode, possess an open voltage (or OCV) around 3.5 V, when Li metal is used as a negative electrode. Most negative electrode materials, such as carbons, tin and silicon have an open voltage below 1.0 V, when cycled against lithium metal.

The theoretical specific capacity (in mAhg^{-1}) noted as C_{th}, represents the number of Li ions (or electrons) involved in the electrochemical process. It is given by the following equation:

$$C_{th} = \frac{\Delta x \cdot F}{M} \times \frac{1000}{3600} \qquad [1.1]$$

where Δx is the number of moles of Li that participate in the reversible electrochemical reaction, F is the Faraday constant which is equal to 96500 C, M is the molecular weight of the electrode compound or element.

The power density of a cell is defined as the battery power per unit mass (Wkg^{-1}). It is also the gravimetric density divided by the discharge time, and will reflect the rate capability of the Li cell. The charge/discharge rate of a cell can be defined using the theoretical specific capacity, and can be noted as *C/h*, meaning that a theoretical complete charge or discharge will take *h* hours. Thus, a 4C rate will theoretically lead to charge or discharge in 15 minutes whereas a C/20 rate will complete a charge or discharge in 20 hours. The power density usually depends on the factors affecting the cell impedance, such as the Li diffusion and electrical resistance of the electrode materials and is inherent to the cell design. Li diffusion and the (de)lithiation mechanism in electrode materials are believed to be a critical factor in the rate capability of a cell.

The cycle life is defined as the number of charge/discharge cycles that can be performed while delivering an acceptable capacity. It mostly depends on the structural stability of the electrode materials as well as presence of side reactions with the electrolyte and build-up of passivating layers such as the solid electrolyte interphase (SEI).

The cost and toxicity of the cell is usually governed by the choice of the materials used in the cell construction, while safety of the cell will also depend on the stability of the chosen materials.

1.2. Anodes

1.2.1. Lithium Metal

In principle, Li metal represents the ultimate LIB negative electrode (anode) having ten times higher specific energy density than lithiated graphite[1]. However, it suffers from at least one serious disadvantage: upon several charge and discharge cycles in non-aqueous electrolytes, dendritic and/or mossy structures of lithium metal are formed on the lithium metal anode, which poses a potentially disastrous safety issue. The dendritic structures — first reported as early as 1980 [8] — may disassociate from the anode and remain as floating structures in the electrolyte (known as dead lithium). These dead lithium fibers, along with fibers that grow directly from the electrode, may result in short circuits, causing spontaneous high-rate discharge [1]. This can result in rapid overheating of the battery leading to fire hazards associated with the flammable organic electrolyte [1]. These issues have been a significant impediment to the commercialization of lithium metal batteries. However, the comparatively low volumetric and gravimetric capacities of LIBs using a graphite anode have created a resurgence of interest in lithium metal batteries [9-11]. Indeed, the high capacities that are quoted for Li-air and Li-sulfur batteries [12], which have attracted considerable recent attention, are based on the use of Li-metal negative electrodes.

Considerable effort has been devoted to prevent moss and dendrite formation on lithium metal anodes during cycling [9,10,13-15] and to understand the negative impacts of dendritic growth on the various aspects of battery cycling. Orsini *et al.* showed, by using scanning electron microscopy (SEM) that there was a direct correlation between dendrite formation and the current density, with larger amounts of dendritic deposits forming at higher current densities (Figure 1.3) [7]. However the SEM method does not provide a way of accurately quantifying the amount of such micro-structures [13]. Studies of mossy or dendritic lithium often use the capacity loss and cycling efficiency as a measure of dendrite formation, although such observations can again only provide a qualitative estimate of the amount of this morphology [9,10]. There have been efforts to theoretically model the dendritic growth, through studies that focus on the morphology of dendritic whiskers (the size, shape and growth) [16-18] but experimental methods that allow *direct quantitative* estimates of mossy or dendritic structures remain elusive.

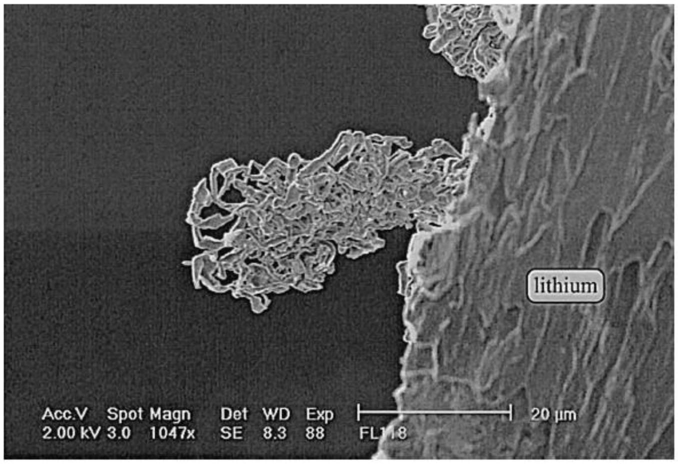

Figure 1.3. Dendrites formed in a lithium battery anode after only one charge step (image taken from reference [13])

1.2.2. Carbon

Rechargeable lithium batteries based on the intercalation concept were first suggested by Armand in 1977 [19]. Because of safety considerations, metal lithium has been replaced by alloys, oxides, chalcogenides and carbonaceous materials as anode materials [20]. In 1990, coke was used by SONY as an anode to solve the propylene carbonate co-intercalation problem [20]. After introducing ethylene carbonate into the non-aqueous electrolyte,[21] graphite can be used properly in Li-ion batteries. Later, graphitized mesophase microbeads (MCMBs) became more popular [22,23]. Graphite has a theoretical capacity of 372 mAhg^{-1} to form LiC_6. Since 1990, many efforts have been made to develop high capacity anode materials to replace graphite. Nongraphitized carbon materials, including soft carbon and hard carbon, have been studied widely [24-26]. Soft carbon materials show a very high reversible Li-storage capacity but a serious voltage hysteresis during delithiation [24-26]. Hard carbon shows a high capacity of 200 mAhg^{-1} over a voltage range of 1.5–0 V vs. Li/Li$^+$. The voltage profile is mainly composed of two regimes, a sloped regime in a voltage range of 1.0–0.1 V with a capacity around 150–250 mAhg^{-1}, and a plateau region with a capacity around 100–400 mAhg^{-1} [24-26]. Hard carbon materials have disadvantages such as low initial coulombic efficiency and low tap density. Spherical hard carbon materials are desirable, however, they are difficult to prepare through direct pyrolyzing of organic or polymer precursors.

1.2.3. Silicon

Carbon is the universally accepted negative electrode in a LIB because of its moderate capacity (372 mAhg^{-1}) and rate capability. However, new, low cost, safe electrode materials with higher capacities are still urgently required for both portable and transportation applications. To this end, tin based anodes with large, theoretical volumetric and gravimetric capacities have recently been commercialized in Sony’s NEXELION cells. Li-Sn system offers approximately eight times volumetric and three times gravimetric theoretical capacity compared to carbon (Figure 1.4). Silicon anodes on the other hand, are particularly attractive alternatives compared to graphite and tin, with a massive volumetric capacity of 8233 mAhcm^{-3} (calculated based on the original volume of crystalline silicon) and extremely high gravimetric theoretical capacity of 3572 mAhg^{-1} (Figure 1.4) as well as their low cost. However the unusually high capacity is associated with large volume changes up to 300% upon lithiation, resulting in particle fracture and capacity retention issues, along with design challenges, since the expansion has to be managed in the cell. Previous work has proposed two main solutions to overcome these problems: (i) using composite electrodes of silicon and carbon, coated with a binder such as carboxymethylcellulose (CMC), to maintain particle-particle contact after many charge/discharge cycles, (ii) limiting voltages over wich the material is cycled, thereby limiting the extent of volumetric expansion by sacrificing some capacity [2,27-29]. The use of nanoparticles of Si also appears to improve capacity retention [30-32]. Such attempts to improve the Si electrode performance and long-term capacity retention may result in the commercialization of a next generation of Li-ion batteries with silicon negative electrodes in the near future.

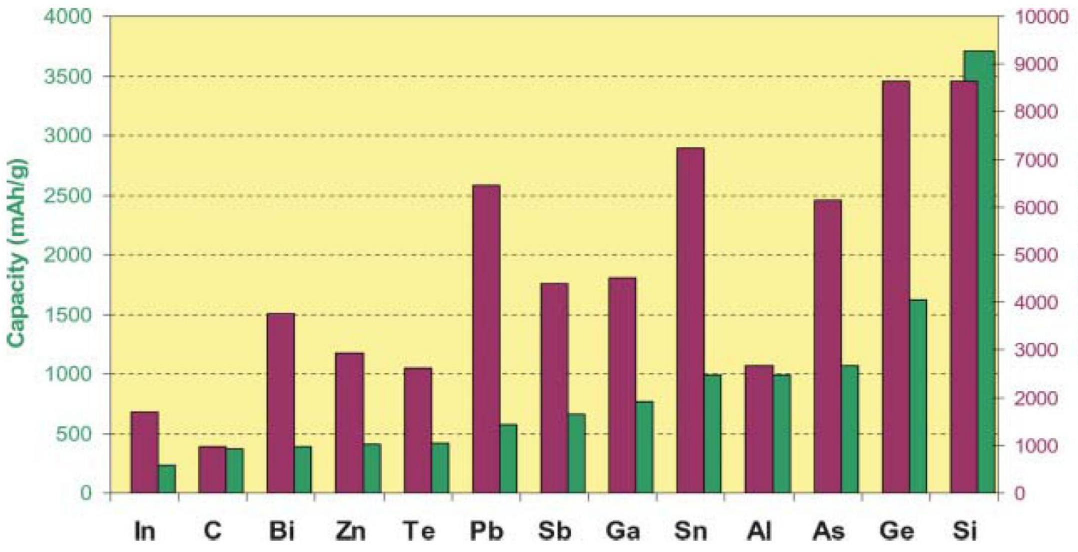

Figure 1.4. Gravimetric (green) and volumetric (purple) capacities of selected electrodes for negative LIB electrodes.

The binary phase diagram of Li-Si system consists of four reported crystalline lithium silicides, from $Li_{12}Si_7$, to the increasingly lithium rich phases Li_7Si_3, $Li_{13}Si_4$ and $Li_{21}Si_5$ (Figure 1.5) [33-37]. However at room temperature, silicon does not form any of these phases on electrochemical lithiation, but instead undergoes a crystalline to amorphous phase transition forming a lithiated amorphous silicide (Figure 1.6) [30]. This phase then recrystallizes at deep discharge to form a metastable phase, $Li_{15}Si_4$, which is isostructural to the thermodynamic phase $Li_{15}Ge_4$ [2]. This final composition provides the theoretical capacity of 3.75 Li per Si (3572 mAh/g). Interestingly, lithiated nanoparticles of crystalline and amorphous thin films less than 2μm thickness of silicon do not recrystallize at deep discharge [4,30]. Unfortunately, due to the amorphous nature of the lithiated silicides, it is not possible to monitor all the structural changes that occur during lithium insertion/removal with conventional methods such as diffraction. The short range order of the amorphous materials remains unknown, preventing attempts to optimize performance based on electrochemical-structure correlations.

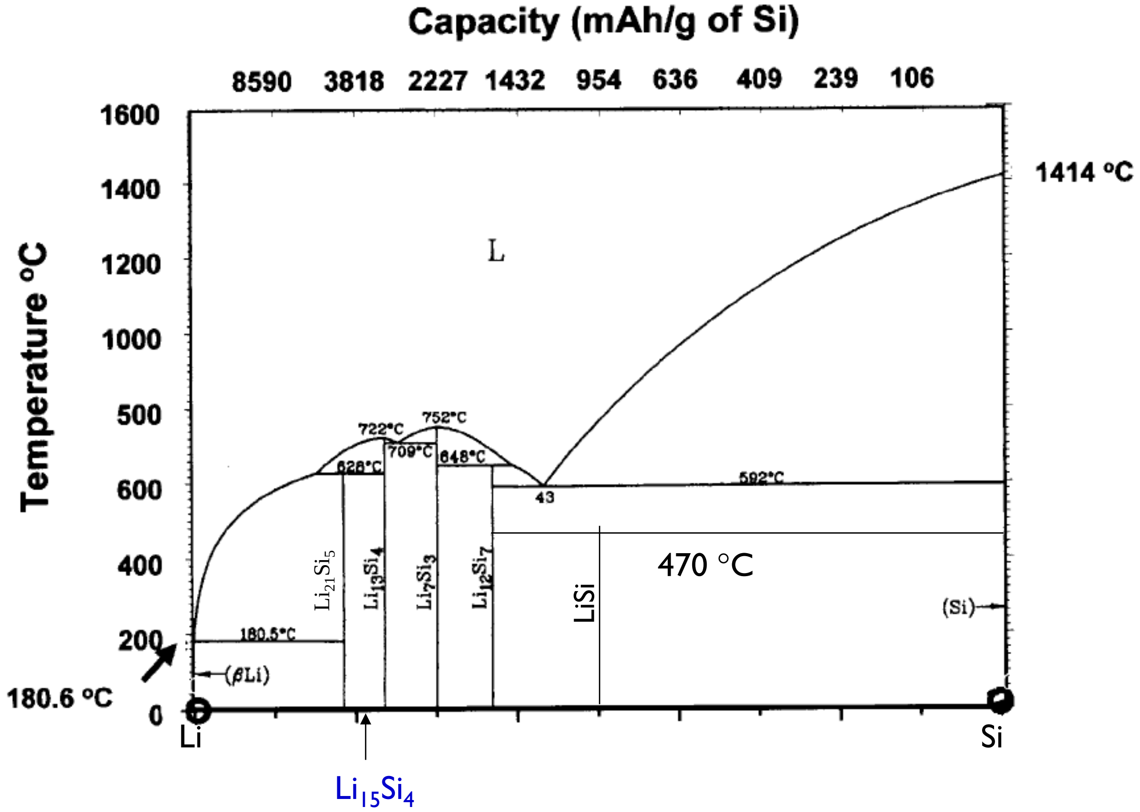

Figure 1.5. Li-Si binary phase diagram (Figure updated from ref. [38] by correcting $Li_{21}Si_5$ phase)

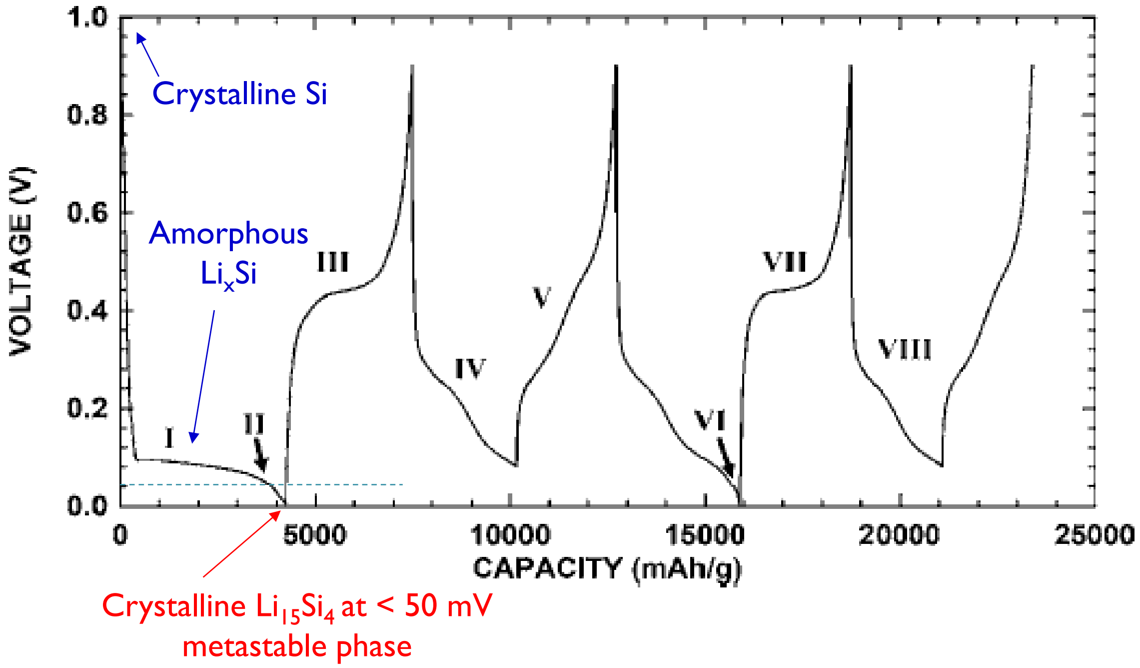

Figure 1.6. Electrochemical cycling profile of crystalline Si vs. Li/Li^+. Important processes involving phase transformations are marked with numbers (figure taken from reference [29])

In this study, the main goal is to investigate the structural changes that occur upon lithiation and delithiation of silicon electrodes by using local structure probes such as Solid State Nuclear Magnetic Resonance Spectroscopy and Pair Distribution Function Analysis, which are introduced in the subsequent sections of this chapter.

1.3. Solid-State Nuclear Magnetic Resonance (NMR) Spectroscopy

While long-range structural information can typically be obtained by conventional diffraction techniques, solid-state NMR is a powerful and useful technique for the study of local structures and electronic properties of positive electrode materials used in Li-ion batteries, even in highly disordered systems [39-41]. Since lithium ions are directly involved in the electrochemical processes, ^7Li and ^6Li nuclei are generally used as probes in solid state NMR of this type of materials. This method is both qualitative and quantitative and can be used to determine the type of Li environments formed upon discharge and removed upon charge and how the local structures change during cycling. Here, basic concepts of magic angle spinning (MAS) NMR along with more specific uses of solid-state NMR in order to investigate real battery samples and actual working batteries are briefly introduced.

1.3.1. Internal Interactions in NMR

In NMR the total interaction energy of the nucleus under observation is the sum of all interactions it experiences. The external magnetic field applied allows the spectroscopist to manipulate the spins. The information about the atomic scale surroundings of a nucleus is contained within the interactions between the nucleus and those surroundings.

In diamagnetic insulating solids, nuclei experience a range of interactions that include magnetic dipolar interaction through space with nearby magnetic moments, chemical shielding modification of the magnetic field at the nucleus due to surrounding electrons and indirect spin-spin coupling interaction of nuclear magnetic moments mediated by intermediate electron spins. In materials containing conducting electrons, these can interact with the nuclear spin via a contact interaction that produces both relaxation and a change in resonance position termed the Knight shift, which provide important information on the nature of the density of states at the Fermi surface. Nuclei with spin $I>1/2$ are also affected by the electric quadrupole interaction, an interaction between the nuclear electric quadrupole moment and the gradient in the electric field at the nucleus. The theory of these interactions is described elsewhere [42]. The interactions that are most valid for interpreting the NMR data during the course of this thesis work, such as chemical shielding and the Knight shift, are described below.

1.3.1.1. Chemical Shielding

The factor that turned NMR from simply an interesting physical observation of the nuclear magnetic moment into a widely useful technique in analytical and material sciences was the realization that the exact resonance depends on the chemical environment of the nucleus. This was termed the chemical shielding and means that the exact resonance frequency is an extremely sensitive discriminator of the chemical environment as it depends on the electron density and hence reflects the chemical bonding and local structure of the nuclei under observation [42]. The chemical shielding arises from the change in the actual magnetic field at the nucleus since the applied magnetic field induces changes in electrons about the nucleus and generates local fields. In non-conducting diamagnetic solids, this results in different resonance frequencies for different nuclear environments unless the internal interactions that broaden each resonance are larger than the resolution limit to distinguish two neighboring resonance frequencies. This phenomenon is the basis for identifying and monitoring the local structures observed in lithiated silicides in this work.

1.3.1.2. Knight Shift

In a conducting solid, the nucleus will couple to the paired electrons of the chemical bonds in the same manner as for diamagnetic insulating solids, but there is the additional effect of the conducting electrons. Unlike paramagnetic and diamagnetic solids, the electrons are delocalized forming a band. The conducting electrons occupy a Fermi distribution within the electronic states of the material, which are occupied in a pair-wise fashion due to the Pauli Exclusion Principle, from the lowest energy up to the Fermi energy. Under magnetic field, there is a shift in energy of the spin-up and spin-down states. The resulting imbalance in the number of these states leads to a net magnetization of the material and hence an associated susceptibility termed the Pauli susceptibility (χ_p).

$$K = 1.5\ \chi_p\ \Omega < |\psi(0)|^2 >_F \qquad [1.2]$$

The shift, K, depends on the wavefunction at the nucleus for electrons averaged over the Fermi surface, where Ω is the volume per electron. The effect is dominated by s-electrons for metals with partially occupied s bands since the s orbital is the only orbital with non-zero electron density at the nucleus. These shifts are positive and generally are much larger than chemical shift effects, for instance, Li – 0.025% (approximately 250 ppm). In other metals or metallic materials, the situation can be more complicated and overall contributions to the Knight shift can be either positive or negative. It also must be noted that sites with lower than cubic symmetry have anisotropic contributions to the electron-nucleus interaction which broaden the resonances observed [42]. Figure 1.7 illustrates the distribution in density of states at T>0 which is analogous to paramagnetism and called temperature induced paramagnetism. In a magnetic field, this will result in a population difference between the two spin states and determines the shift.

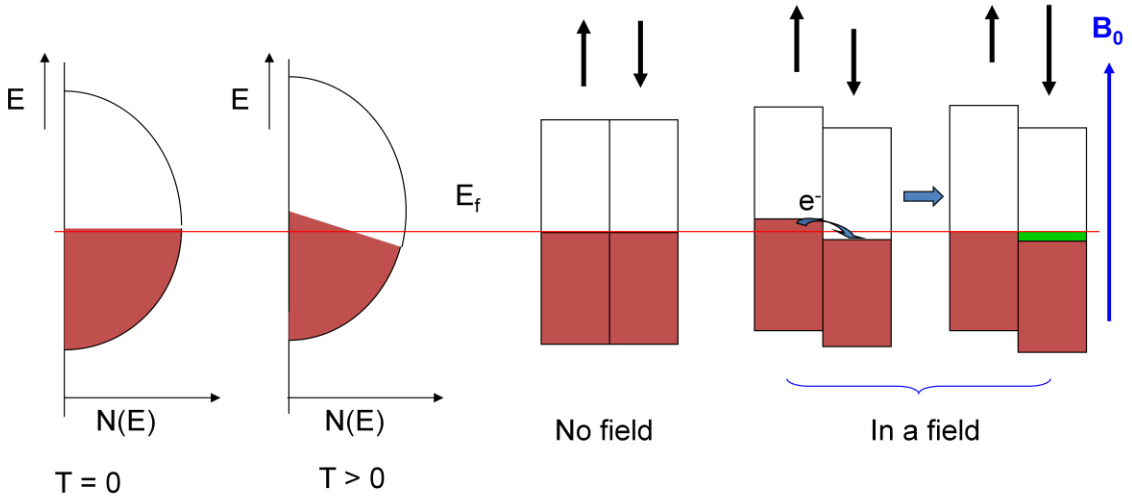

Figure 1.7. Band structure at the Fermi level for a metal. At T>0 the distribution in density of states for a metal will result in a population difference shown in no magnetic field and magnetic field cases.

1.3.1.3. Quadrupole Interaction

Quadrupolar nuclei have a spin > 1/2, and an asymmetric distribution of nucleons giving rise to a non-spherical positive electric charge distribution; this is in contrast to spin-1/2 nuclei, which have a spherical distribution of positive electric charge. The asymmetric charge distribution in the nucleus is described by the nuclear electric quadrupole moment, *eQ*, which is an instrinsic property of the nucleus, and is the same regardless of the environment. The interaction between quadrupole moment and electric field gradient (EFG) is called the quadrupolar interaction [42]. The EFG is caused by surrounding electrons distribution. The magnitude of the quadrupolar interaction is given by quadrupolar coupling constant QCC, which is defined in equation (1.3).

$$\mathrm{QCC} = eQ \cdot eq/\mathrm{h} \qquad [1.3]$$

The EFG at the quadrupolar nucleus can be described by an asymmetric traceless tensor, which can also be diagonalized. The principal components of the EFG tensor are defined as $|V_{xx}| \leq |V_{yy}| \leq |\mathrm{V}_{zz}|$. The asymmetry of the quadrupolar interaction is given by the asymmetry parameter:

$$\eta = (V_{xx} - V_{yy})/V_{zz} \quad (0 \leq \eta \leq 1) \qquad [1.4]$$

If $\eta = 0$, the EFG tensor is axially symmetric.

Effects of the first- and second-order interactions on the energy levels of a spin-5/2 nucleus are shown in Figure 1.7. The transition (1/2↔-1/2) is called central transition (CT), which is not affected by first order quadruple interaction. Other transitions such as (3/2↔1/2), (-1/2↔-3/2), (5/2↔3/2) and (-3/2↔-5/2) are called satellite transitions. In case of second order quadrupolar interaction the two energy levels m and -m are shifted by the same value but in the opposite directions. The central transition is, therefore affected and a broad quadrupole line shape is formed.

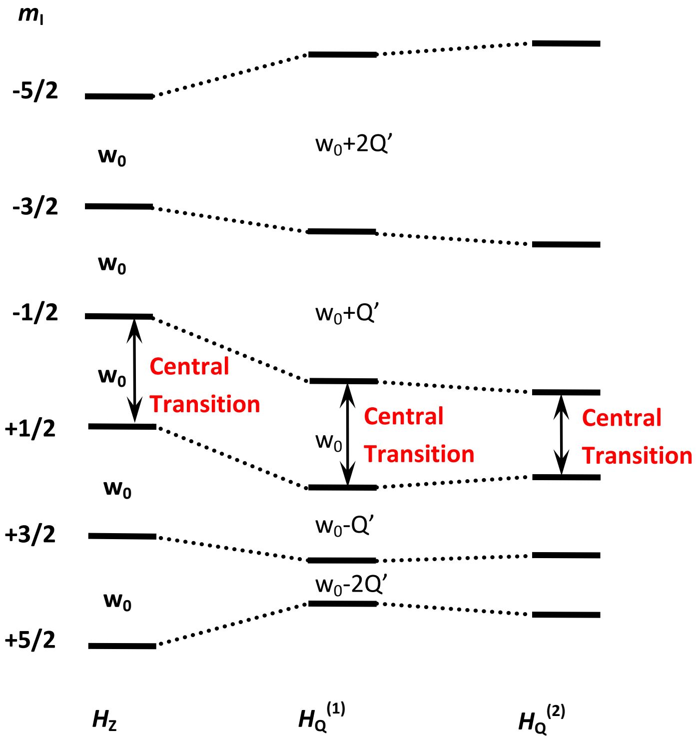

Figure 1.8. Effects of first and second-order quadrupolar interaction on a spin 5/2 nucleus. w_0 is the quadrupolar frequency and Q is the quadrupolar moment.

Many of the interactions relevant in NMR depend on the orientation of the sample in the magnetic field and thus have an angular dependence. Magic Angle Spinning which is discussed in the next section involves the physical rotation of the sample at magic angle of 54.74^o with respect to external magnetic field with a frequency in kHz range. The angle 54.74^o is the solution to the term $3\cos^2(\theta)–1$, the angular dependence in the above interactions. At the magic angle this term becomes zero removing the dipole dipole interaction and chemical shift anisotropy interactions (if the frequency of the interaction is smaller than the spinning frequency) and first order quadrupole interactions narrowing the NMR spectra. The broadening effects due to higher order interactions of the quadrupolar nuclei can be eliminate by the application of different NMR pulse sequences. However, the nuclei of interest in this study do not suffer from severe quadrupolar broadenings and simple NMR sequences such as Hahn-echo [42] with MAS technique are sufficient for detailed analysis of chemical environments.

1.3.2. Magic Angle Spinning (MAS) NMR

In solution NMR, fast molecular motion effectively removes all the anisotropic interactions present in a molecule and, as a result of that, sharp resonances can be observed with greater resolution. In solid-state NMR spectroscopy, the lack of molecular motion leads to broadening of all resonances. Therefore, efforts have been made to develop techniques to acquire high resolution NMR spectra of solids.

Magic Angle Spinning (MAS), which involves spinning the sample at high speeds at a “magic angle” θ of 54.736 with respect to the external magnetic field (Figure 1.8), was introducted to eliminate anisotropic interactions such as chemical shielding interaction, heteronuclear dipolar coupling and first order quadrupole coupling (for nuclei with spin $I > 1/2$). A detailed explanation of these NMR interactions can be found elsewhere [42].

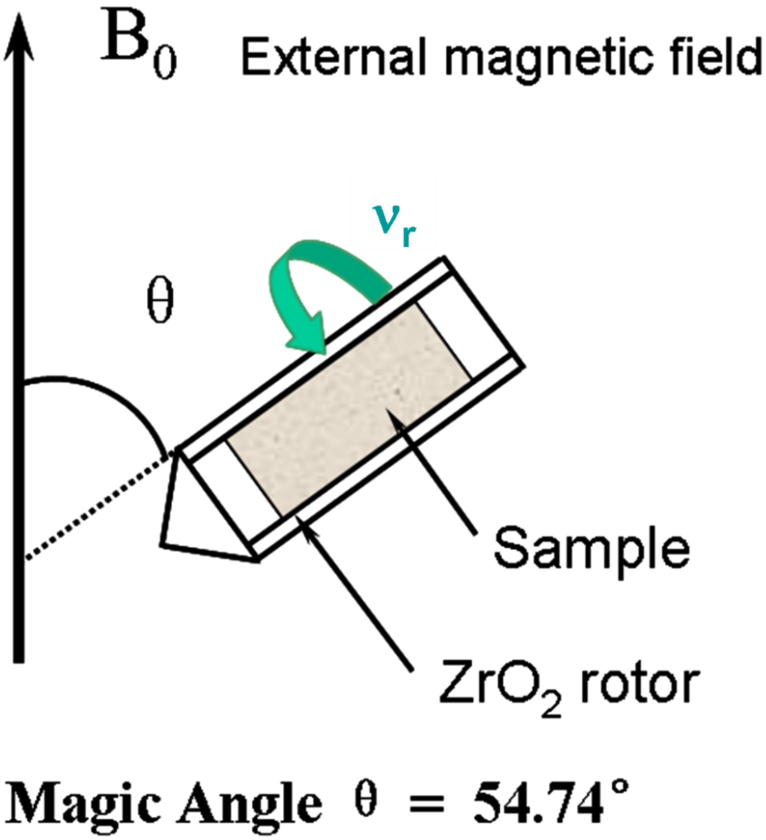

Figure 1.9. Schematic representation of the Magic Angle Spinning (MAS) technique, where θ is the angle between the rotor and the external magnetic field, and v_r is the spinning speed frequency.

When the spinning frequency v_r is faster than the size of the anisotropic interaction, only a single resonance can be observed; otherwise, the powder pattern is split into relatively narrow lines spaced at integer multiples of the sample rotation frequency (or MAS speed), which are called spinning sidebands. In practice, the spinning frequency is limited by the outer diameter of the spinner. The maximum spinning speed used in this work is 38 kHz using a 1.8 mm spinner (i.e. rotor) and is not enough to eliminate the spinning sidebands. When the sample is not rotated during NMR acquisition, the experiment is called “static” and as a result the resonances are significantly broadened. It must be pointed out that, in this work, both MAS technique and static NMR is used for characterization for reasons that will be covered in other chapters.

1.3.3. In-situ Static Solid-State NMR of Li-ion Batteries

Although nuclear magnetic resonance (NMR) spectroscopy has been used to obtain detailed local structural information from battery materials [41,43], it has not been widely used to study batteries under realistic operating conditions. The first *in situ* NMR experiments of batteries were performed by Gerald *et al.* [44] in where an NMR toroid cavity was used for both *in-situ* NMR and for imaging. However, a poor signal-to-noise ratio was obtained and furthermore, the toroid design was difficult to combine with a standard LIB. More recent *in situ* experiments were performed by Letellier *et al.* to examine the insertion reaction of Li in disordered carbon and graphitic anodes by ^{7}Li NMR spectroscopy making use of a so-called plastic lithium-ion battery [45,46]. This battery design is advantageous because the battery is flexible and does not require external pressure to maintain contact between the cathode, electrolyte and anode. Both sets of experiments (the toroid and plastic-bag designs) were performed in static mode, i.e., without magic angle spinning (MAS). The plastic bag design utilizing a conventional static NMR probe is found suitable for the experiments in this work and details of a new setup developed from previous work and results will be discussed in Chapter 3.

1.4. Powder Diffraction Methods and Rietveld Analysis

The most conventional experimental method for the structural determination of battery materials is powder diffraction. Analysis of the powder diffraction data can give information about the long range structure of the sample as well as determination of phase or phases present, unit cell dimensions, site occupancies, displacement parameters and atomic positions within the unit cell. The analysis requires fitting a model phase to the diffraction data and can be performed by a Rietveld refinement.

1.4.1. The Rietveld Method

The Rietveld analysis consists of a whole diffraction pattern fitting, by simulating the pattern using intensities computed from crystallographic models and various functions to account for experimental effects [47]. It is a powerful method for the determination of the average structure of a material, including atomic positions and site occupancies. The determination of structural information from a powder diffraction pattern utilizing the Rietveld method requires an initial structure model. Initial estimates of the cell parameters, space group, as well as experimental parameters, such as the wavelength, need to be known before the start of the Rietveld refinement procedure. The three important characteristics of the diffraction pattern that are modeled during a Rietveld refinement are the position, intensity and profile of each reflection.

The position of a reflection is given by Bragg's law, expressing the condition for the constructive interference of the diffracted beams. The Bragg equation is given as:

$$2d_{hkl}\sin\theta=\lambda \tag{1.5}$$

where h, k, l are the Miller indices, d is the interplanar spacing, θ is the diffraction angle and λ is the X-ray or neutron wavelength.

The intensity I_{hkl} of a reflection is proportional to the square of the structure factor F_{hkl}^2 and will depend on atomic information, such as site occupancy, atomic coordinates, atomic motion and atomic scattering factor.

The profile of each reflection is the third important characteristic of a diffraction pattern. In powder diffraction, the reflection profiles are typically not Gaussian, and a pseudo-Voigt function, which is a convolution of a Gaussian and a Lorentzian function, is typically used [48-54]. The pseudo-Voigt function has been widely used to model peak shapes in powder diffraction, and is typically modeled with angle dependent functions. One of the main profile parameters is the Full Width at Half Maximum or *FWHM*, which is given by for Gaussian on Lorentzian components:

$$FWHM_G^2 = U\tan^2\theta + V\tan\theta + \mathrm{W} \tag{1.6}$$

$$FWHM_L^2 = X\tan^2\theta + Y(\cos\theta)^{-1} \tag{1.7}$$

The parameters $U, V, W, X,$ and Y can be refined. V must be negative, while the others must be positive. Peak asymmetry generally results from the measurement geometry and is most severe at low scattering angles. Parameters that correct the peak asymmetry can also be refined [53,54].

1.5. Pair Distribution Function (PDF) Analysis

The Pair Distribution Function (PDF) analysis technique has been used with great success in the analysis of amorphous and disordered systems [55]. Recently, application to systems with greater crystallinity, like many battery compounds, has become possible due to several advances in experimental measurements [56,57].

In principle, PDF analysis is the real space analogue to the Rietveld refinement method, with an advantage that direct structural information, such as changes in coordination numbers or bond distances, can often be extracted. In this way, PDF analysis is comparable to Extended X-ray Absorption Fine Structure (EXAFS), but it can be applied to low atomic number samples and it is not limited to the first coordination shell. It will also show all the correlations in the compound, not only those involving the element whose edge is chosen in the EXAFS experiment.

PDF analysis is used to study the chemical short range order, which cannot be extracted from conventional diffraction patterns. Traditional diffraction uses only Bragg scattering, which contains information about the long range structure, whereas PDF uses the total scattering (both Bragg and diffuse scatterings).

1.5.1. Obtaining the PDF

The PDF $G(r)$ gives the probability of finding an atom at a given distance r from another atom and can be considered as a bond length distribution. It is obtained from the powder diffraction via a Fourier transform of the normalized scattering intensity $S(Q)$ [42]:

$$S(Q) = 1 + \left[I_{coh}(Q) - \sum_i c_i \left| f_i(Q) \right|^2 \right] \Big/ \left| \sum_i c_i f_i(Q)^2 \right| \qquad [1.8]$$

$$G(r) = 4\pi r[\rho(r) - \rho_0] = \frac{2}{\pi} \int_0^\infty Q[S(Q) - 1] \sin(Qr) dQ \qquad [1.9]$$

where I_{coh} is the coherent part of the scattering, c_i and f_i are the number/types of atoms and scattering factors respectively. $\rho(r)$ is the microscopic pair density, ρ_0 is the average number density and Q is the magnitude of the scattering vector ($Q=(4\pi\sin\theta)/\lambda$).

One problem with the Fourier transform is that it is not possible to measure data up to infinite Q. The cut-off at finite Q_{max} decreases the real space resolution of the PDF and causes termination ripples. A comparison of the resolution obtained by the Fourier transform of the corrected $S(Q)$ is shown in Figure 1.9. It is obvious that higher Q measurements give higher real space resolution. Thus $S(Q)$ must be measured to a high value of Q, typically more than 20 Å^{-1} for crystalline materials at 300 K. For both X-ray and neutron scattering experiments, high energies are required in order to access high values of Q_{max}. Data suitable for PDF analysis are obtained at high energy synchrotron X-ray or spallation neutron sources. For X-rays, in order to increase the range of observed Q, the sample is placed as close as possible to an image plate, which is the detector of choice. A picture of the X-ray PDF experimental setup is shown in Figure 1.10.

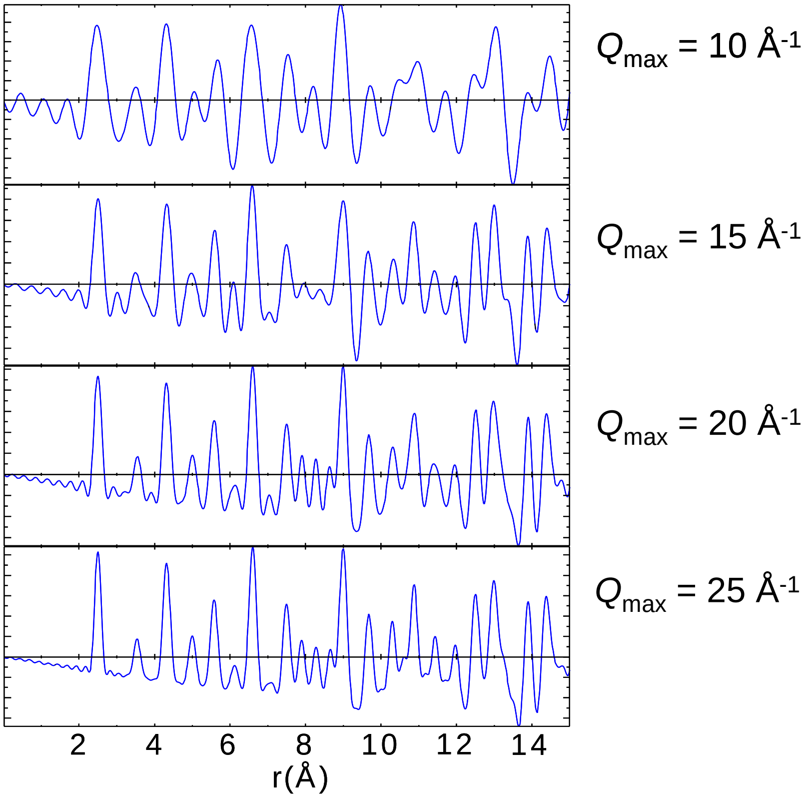

Figure 1.10. Illustration of the effect of a finite Q range on the real space resolution of the PDF determined for Ni metal. An obvious decrease in termination ripples is noticeable as the PDF is determined from a larger Q range [58].

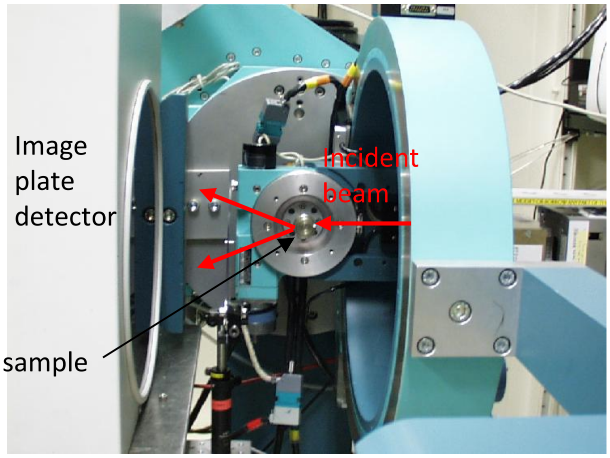

Figure 1.11. Picture of the experimental setup, showing the image plate mounted orthogonal to the beam path, as close as possible to the sample [58].

1.5.2. PDF Refinement

PDF data can be used to obtain direct information on bond distances in a sample. The intensity of the peaks also contains quantitative information about the number of bond distances of concern. It is also possible to calculate the PDF $G_c(r)$ in order to refine a structural model, using the relation [59]:

$$G_c(r) = \frac{1}{r}\sum_i \sum_j \left[\frac{b_i b_j}{\langle b \rangle^2} \delta(r - r_{ij}) \right] - 4\pi r \rho_0 \qquad [1.10]$$

The sum is performed over all pairs of atoms i and j separated by r_{ij}. The scattering power of the atom i is given by the value of b_i and $< b >$ is the average scattering power of the sample. The value of b_i is, in the case of neutrons and X-rays, given by the scattering length and the atomic factor given at a given Q.

The experimental PDFs can be refined in an analogous manner as the Rietveld method using least squares and have similar agreement factors.

$$R_w = \left[\frac{\sum_i w(r_i)[G_{obs}(r_i) - G_{calc}(r_i)]^2}{\sum_i w(r_i)[G_{obs}(r_i)]^2} \right]^{1/2} \qquad [1.11]$$

where G_{obs} and G_{calc} stand for the observed and calculated PDF, respectively. Direct modeling of a small repeating unit of simple crystalline structures is the preferred method of the determination of structure from the PDF.

1.6. Research Strategy

In this report we utilize a flexible plastic LIB design for *in situ* and a combination of static, *in-situ* and MAS, *ex-situ* ^{7}Li and ^{29}Si NMR spectroscopy and X-ray PDF analysis as local structural probes in order to monitor/identify the changes in the short range order that occur during electrochemical cycling of crystalline silicon in an actual working LIB. We demonstrate that *in-situ* ^{7}Li NMR experiments can be used to capture changes that cannot be readily seen by ex-situ methods. In order to correlate Li NMR shifts with specific local environments, we first acquire the ^{7}Li MAS NMR spectra of the crystalline phases $Li_{12}Si_7$, Li_7Si_3, $Li_{13}Si_4$, $Li_{15}Si_4$ and $Li_{21}Si_5$. The Li NMR shifts associated with specific Li local environments and types of silicon clusters are then used to help determine the structural changes that occur on discharge of the Si-Li battery. The developed static *in situ* NMR setup allowed investigation other systems such as Li metal batteries. As an extension of the main work that is discussed in the following chapters, in Chapter 5, a quantitative study on the Li microstructures formed upon cycling of Li metal batteries will be described.

1.7. References

(1) Tarascon, J. M.; Armand, M. *Nature* **2001**, *414*, 359.

(2) Obrovac, M. N.; Christensen, L. *Electrochem. Solid-State Lett.* **2004**, *7*, A93.

(3) Li, H.; Huang, X.; Chen, L.; Zhou, G.; Zhang, Z.; Yu, D.; Mo, Y. J.; Pei, N. *Solid State Ionics* **2000**, *135*, 181.

(4) Hatchard, T. D.; Dahn, J. R. *J. Electrochem. Soc.* **2004**, *151*, A838.

(5) Breger, J., *Ph.D. Thesis*, Stony Brook University, NY, 2006.

(6) Bruce, P. G. *Chemical Communications* **1997**, 1817.

(7) Megahed, S.; Scrosati, B. *Journal of Power Sources* **1994**, *51*, 79.

(8) Epelboin, I.; Froment, M.; Garreau, M.; Thevenin, J.; Warin, D. *Proc. - Electrochem. Soc.* **1980**, *80*, 417.

(9) Sannier, L.; Bouchet, R.; Grugeon, S.; Naudin, E.; Vidal, E.; Tarascon, J. M. *J. Power Sources* **2005**, *144*, 231.

(10) Wang, C.; Wang, D. L.; Dai, C. S. *Journal of the Electrochemical Society* **2008**, *155*, A390.

(11) Xu, J. Q.; Yang, J.; NuLi, Y.; Wang, J. L.; Zhang, Z. S. *Journal of Power Sources* **2006**, *160*, 621.

(12) Ogasawara, T.; Debart, A.; Holzapfel, M.; Novak, P.; Bruce, P. G. *Journal of the American Chemical Society* **2006**, *128*, 1390.

(13) Orsini, F.; Du Pasquier, A.; Beaudoin, B.; Tarascon, J. M.; Trentin, M.; Langenhuizen, N.; De Beer, E.; Notten, P. *J. Power Sources* **1998**, *76*, 19.

(14) Saint, J.; Best, A. S.; Hollenkamp, A. F.; Kerr, J.; Shin, J. H.; Doeff, M. M. *J. Electrochem. Soc.* **2008**, *155*, A172.

(15) Howlett, P. C.; MacFarlane, D. R.; Hollenkamp, A. F. *Electrochemical and Solid State Letters* **2004**, *7*, A97.

(16) Yamaki, J.; Tobishima, S.; Hayashi, K.; Saito, K.; Nemoto, Y.; Arakawa, M. *Journal of Power Sources* **1998**, *74*, 219.

(17) Monroe, C.; Newman, J. *Journal of the Electrochemical Society* **2003**, *150*, A1377.

(18) Chazalviel, J. N. *Phys. Rev. A* **1990**, *42*, 7355.

(19) Armand, M.; Touzain, P. *Materials Science and Engineering* **1977**, *31*, 319.

(20) Arico, A. S.; Bruce, P.; Scrosati, B.; Tarascon, J.-M.; van Schalkwijk, W. *Nat. Mater.* **2005**, *4*, 366.

(21) Xu, K. *Chem. Rev. (Washington, DC, U. S.)* **2004**, *104*, 4303.

(22) Yamaura, J.; Ozaki, Y.; Morita, A.; Ohta, A. *J. Power Sources* **1993**, *43*, 233.

(23) Mabuchi, A. *Tanso* **1994**, *165*, 298.

(24) Dahn, J. R.; Zheng, T.; Liu, Y.; Xue, J. S. *Science (Washington, D. C.)* **1995**, *270*, 590.

(25) Azuma, H.; Imoto, H.; Yamada, S.; Sekai, K. *Journal of Power Sources* **1999**, *81*, 1.

(26) Tirado, J. L. *Materials Science & Engineering R-Reports* **2003**, *40*, 103.

(27) Li, J.; Christensen, L.; Obrovac, M. N.; Hewitt, K. C.; Dahn, J. R. *J. Electrochem. Soc.* **2008**, *155*, A234.

(28) Hochgatterer, N. S.; Schweiger, M. R.; Koller, S.; Raimann, P. R.; Woehrle, T.; Wurm, C.; Winter, M. *Electrochem. Solid-State Lett.* **2008**, *11*, A76.

(29) Obrovac, M. N.; Krause, L. J. *J. Electrochem. Soc.* **2007**, *154*, A103.

(30) Limthongkul, P.; Jang, Y.-I.; Dudney, N. J.; Chiang, Y.-M. *J. Power Sources* **2003**, *119-121*, 604.

(31) Chan, C. K.; Peng, H.; Liu, G.; McIlwrath, K.; Zhang, X. F.; Huggins, R. A.; Cui, Y. *Nat. Nanotechnol.* **2008**, *3*, 31.

(32) Holzapfel, M.; Buqa, H.; Hardwick, L. J.; Hahn, M.; Wuersig, A.; Scheifele, W.; Novak, P.; Koetz, R.; Veit, C.; Petrat, F.-M. *Electrochim. Acta* **2006**, *52*, 973.

(33) Nesper, R.; Von Schnering, H. G.; Curda, J. *Chem. Ber.* **1986**, *119*, 3576.

(34) Nesper, R.; Von Schnering, H. G. *J. Solid State Chem.* **1987**, *70*, 48.

(35) Nesper, R. *Prog. Solid State Chem.* **1990**, *20*, 1.

(36) Frank, U.; Mueller, W.; Schaefer, H. *Z. Naturforsch., Teil B* **1975**, *30B*, 10.

(37) Klemm, W.; Struck, M. *Z. Anorg. Allg. Chem.* **1955**, *278*, 117.

(38) Stearns, L. A.; Gryko, J.; Diefenbacher, J.; Ramachandran, G. K.; McMillan, P. F. *Journal of Solid State Chemistry* **2003**, *173*, 251.

(39) Grey, C. P.; Lee, Y. J. *Solid State Sciences* **2003**, *5*, 883.

(40) Lee, Y. J.; Grey, C. P. *Journal of Physical Chemistry B* **2002**, *106*, 3576.

(41) Grey, C. P.; Dupre, N. *Chem. Rev. (Washington, DC, U. S.)* **2004**, *104*, 4493.

(42) MacKenzie, K. J. D. *Multinuclear Solid-State Nuclear Magnetic Resonance of Inorganic Materials*, 2002.

(43) Key, B.; Bhattacharyya, R.; Morcrette, M.; Seznec, V.; Tarascon, J. M.; Grey, C. P. *Journal of the American Chemical Society* **2009**, *131*, 9239.

(44) Gerald, R. E.; Klingler, R. J.; Sandi, G.; Johnson, C. S.; Scanlon, L. G.; Rathke, J. W. *J. Power Sources* **2000**, *89*, 237.

(45) Chevallier, F.; Letellier, M.; Morcrette, M.; Tarascon, J. M.; Frackowiak, E.; Rouzaud, J. N.; Beguin, F. *Electrochem. Solid-State Lett.* **2003**, *6*, A225.

(46) Letellier, M.; Chevallier, F.; Morcrette, M. *Carbon* **2007**, *45*, 1025.

(47) Rietveld, H. M. *Journal of Applied Crystallography* **1969**, *2*, 65.

(48) Young, R. A.; Prince, E.; Sparks, R. A. *Journal of Applied Crystallography* **1982**, *15*, 357.

(49) Caglioti, G.; Paoletti, A.; Ricci, F. P. *Nuclear Instruments & Methods* **1958**, *3*, 223.

(50) Thompson, P.; Cox, D. E.; Hastings, J. B. *Journal of Applied Crystallography* **1987**, *20*, 79.

(51) Howard, C. J. *Journal of Applied Crystallography* **1982**, *15*, 615.

(52) Finger, L. W.; Cox, D. E.; Jephcoat, A. P. *Journal of Applied Crystallography* **1994**, *27*, 892.

(53) Stephens, P. W. *Journal of Applied Crystallography* **1999**, *32*, 281.

(54) McCusker, L. B.; Von Dreele, R. B.; Cox, D. E.; Louer, D.; Scardi, P. *Journal of Applied Crystallography* **1999**, *32*, 36.

(55) Egami, T. *Materials Transactions* **1990**, *31*, 163.

(56) Breger, J.; Dupre, N.; Chupas, P. J.; Lee, P. L.; Proffen, T.; Parise, J. B.; Grey, C. P. *Journal of the American Chemical Society* **2005**, *127*, 7529.

(57) Chupas, P. J.; Qiu, X. Y.; Hanson, J. C.; Lee, P. L.; Grey, C. P.; Billinge, S. J. L. *Journal of Applied Crystallography* **2003**, *36*, 1342.

(58) Chupas, P. J.; *Ph.D. Thesis*, Stony Brook University, NY, 2003.

(59) Egami, T.; Billinge, S. J. L.; *Underneath the Bragg Peaks: Structural Analysis of Complex Materials*, 2003.

Chapter 2

Solid State NMR and PDF Studies of Crystalline Lithium Silicide Model Compounds

Abstract

Crystalline lithium silicides, $Li_{12}Si_7$, Li_7Si_3, $Li_{13}Si_4$, $Li_{15}Si_4$ and $Li_{21}Si_5$, have been synthesized from lithium and silicon precursors and characterized by solid state MAS NMR and X-ray PDF analysis. The local structure of crystalline model compounds has been investigated in order to construct a set of trends in lithium and silicon NMR signals, which in turn is used as a key to investigate the types of local structures of the phases observed in battery samples. The ^{7}Li NMR signal obtained by ex-situ MAS NMR has shown a clear trend; as lithium concentration increases the lithium signal shifts upfield. A similar and opposite trend is observed for the ^{29}Si NMR signal. The lithium environments around isolated silicon clusters and bonded silicon clusters have shown distinct shifts that are used to identify the type of local ordering in actual battery samples.

The PDF studies have shown distinct local environments for Li-Li, Li-Li and Si-Si correlations. Li-Li and Li-Si correlations have been found to be in the range of 2.5-2.7Å whereas Si-Si correlations, depending on the type of Si-Si bonding, found to vary between 2.33 Å and 4.75 Å. The metastable $Li_{15}Si_4$ phase and $Li_{21}Si_5$ have been found to contain no Si-Si direct bonding.

2.1. Introduction

The binary phase diagram of Li-Si system consists of four reported crystalline lithium silicides, from $Li_{12}Si_7$, to the increasingly lithium rich phases Li_7Si_3, $Li_{13}Si_4$ and $Li_{21}Si_5$ (Figure 1.5) [1-5]. LiSi, on the other hand, is another crystalline phase that can only be synthesized under high pressure [6]. At room temperature, silicon does not form any of these phases on electrochemical lithiation, but instead undergoes a crystalline to amorphous phase transition forming a lithiated amorphous silicide. This phase then recrystallizes at deep discharge to form a metastable phase, $Li_{15}Si_4$, which is isostructural to the thermodynamic phase $Li_{15}Ge_4$ [7]. This final composition provides the theoretical capacity of 3.75 Li per Si (3572 mAh/g). Unfortunately, due to the amorphous nature of the lithiated silicides, it is not possible to monitor all the structural changes that occur during lithium insertion/removal with conventional methods such as diffraction. The short range order of the amorphous materials remains unknown, preventing attempts to optimize performance based on electrochemical-structure correlations.

The crystallographic structures and the silicon connectivities of model compounds are shown in Figure 2.1. It is clear that lithium environments are closely associated with type of silicon clustering in the structure. Basic understanding of the electronic and local structure of each phase helps in understanding known lithium silicon local structures which will be used to investigate and characterize amorphous lithium silicides that are formed upon lithiation of silicon in the following chapters.

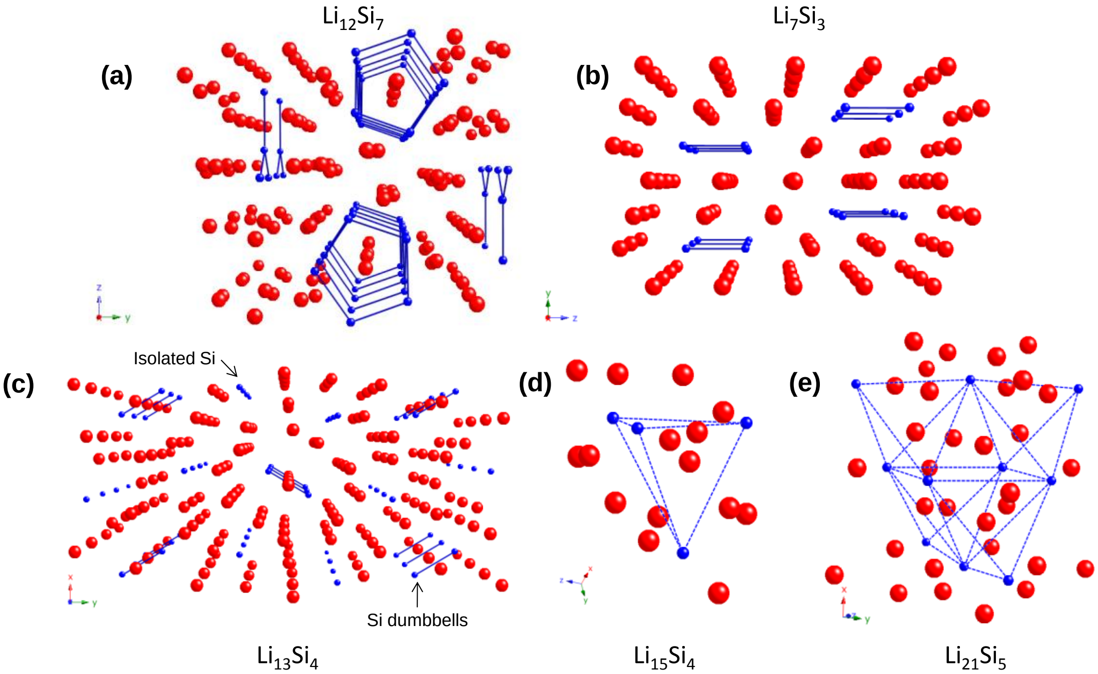

Figure 2.1. Structural representations of **(a)** $Li_{12}Si_7$, 13 Li and 9 Si crystallographic sites, (Si-Si distances in rings and stars, 2.35 – 2.40 Å) [2,3], **(b)** Li_7Si_3, 3 Li and 1 Si sites, (Si-Si dumbbell distances, 2.332 Å) [3,5], **(c)** $Li_{13}Si_4$, 8 Li and 2 Si sites, (Si-Si dumbbells, 2.383Å and isolated silicon ions) [3,4], **(d)** $Li_{15}Si_4$, 2 Li and 1 Si sites (isolated silicon ions, Si-Si distances > 4.5 Å) [7] and **(e)** $Li_{21}Si_5$, 16 Li and 4 Si sites, (Si – Si distances > 4.6 Å) [1,3]. (Li and Si atoms are shown in red and blue, respectively; blue lines: Si-Si bonds; blue dashed lines: closest Si-Si contacts > than 3.0 Å).

2.2. Experimental Methodology

2.2.1. Synthesis of Model Compounds

The lithium silicides were synthesized by mixing stoichiometric amounts of lithium metal and silicon 325 (Aldrich) mesh powder in an argon glove box. The mixtures were sealed in an inert atmosphere and ball-milled out of the glove box for 8 hours. The containers were transferred back into the glove box, sealed in inox (stainless-steel) containers, and then annealed at 450 °C for $Li_{12}Si_7$ and $Li_{21}Si_5$ and at 500 °C for Li_7Si_3 and $Li_{13}Si_4$, for 12 hours. $Li_{15}Si_4$, however, was not annealed since it is a metastable phase; annealing led to the decomposition of this material forming a mixture of unidentified (likely, metastable) phases. These samples were prepared by Dr. V. Seznec at CNRS, Amiens, France.

2.2.2. Diffraction and PDF

All the diffraction patterns of the model compounds were acquired with a Bruker D8 advance diffractometer (Cu K_α radiation, Θ-2Θ geometry, Vantec counter). An airtight swagelok cell with a beryllium window was used (details of the setup described elsewhere [8]). Total scattering patterns (Bragg diffraction patterns and diffuse scattering data) were acquired with 2D detectors (GE a-Si and Perkin Elmer a-Si 2D image plates) at the Advanced Photon Source in Argonne National Lab, IL (60 and 90 keV beam energies). 2D images were converted into 1D Q-space vs. Intensity plots by FIT2D program by using CeO_2 calibration standard and PDF patterns (G(r)) were obtained with the PDFGetX2[9] software. The data range used was up to 23 A^{-1} Q. The PDFGui software[10] was used to fit the data.

2.2.3. NMR

^7Li MAS NMR spectra were acquired at 77.63 MHz using a CMX-200 MHz spectrometer, with a 1.8 mm MAS probe at a 38 kHz spinning speed. All the ^7Li spectra were referenced to a 1M LiCl solution at 0 ppm. Rotor-synchronized spin-echoes ($90^o - \tau - 180^o - \tau -$ acq) were used to acquire the spectra, where the values of τ were chosen, such that they were equal to the rotor period (i.e. $\tau = 1$ / spinning frequency). A recycle delay of 0.2 s was used to collect a total of 32000 scans for each sample. ^{29}Si MAS NMR spectra were acquired at 71.55 MHz using a CMX-360 MHz spectrometer with a 4.0 mm MAS probe at a 14 kHz spinning speed. The ^{29}Si NMR spectra were referenced to tetramethylsilane (TMS) (at 0 ppm) as an external reference. Spin-echoes ($90^o - \tau - 180^o - \tau -$ acq) were used to acquire the spectra. The sequence was rotor synchronized with the value of τ being chosen, such that it was equal to the rotor period (i.e. $\tau = 1$ / frequency of spinning). A recycle delay of 1 s was used. The one pulse spectra took approximately 2 days to acquire, due to the low natural abundance of ^{29}Si (4.67%). To maximize the signal-to-noise level, the spectral width of each spectrum was minimized so as to cover only the range containing the resonances.

2.3. Results

2.3.1. Diffraction

The diffraction patterns of all the model compounds and profile fittings of selected compound are shown in Figure 2.2. The majority of the synthesized compounds were largely impurity free except the minor unreacted Si phase in $Li_{15}Si_4$, and very minor impurities (including Li_2Si) in $Li_{12}Si_{7.}$ $Li_{13}Si_4$, however, does contains a number of impurities, including $Li_{21}Si_5$, $Li_{12}Si_7$ and a weaker unidentified (unreported) impurity phase(s).

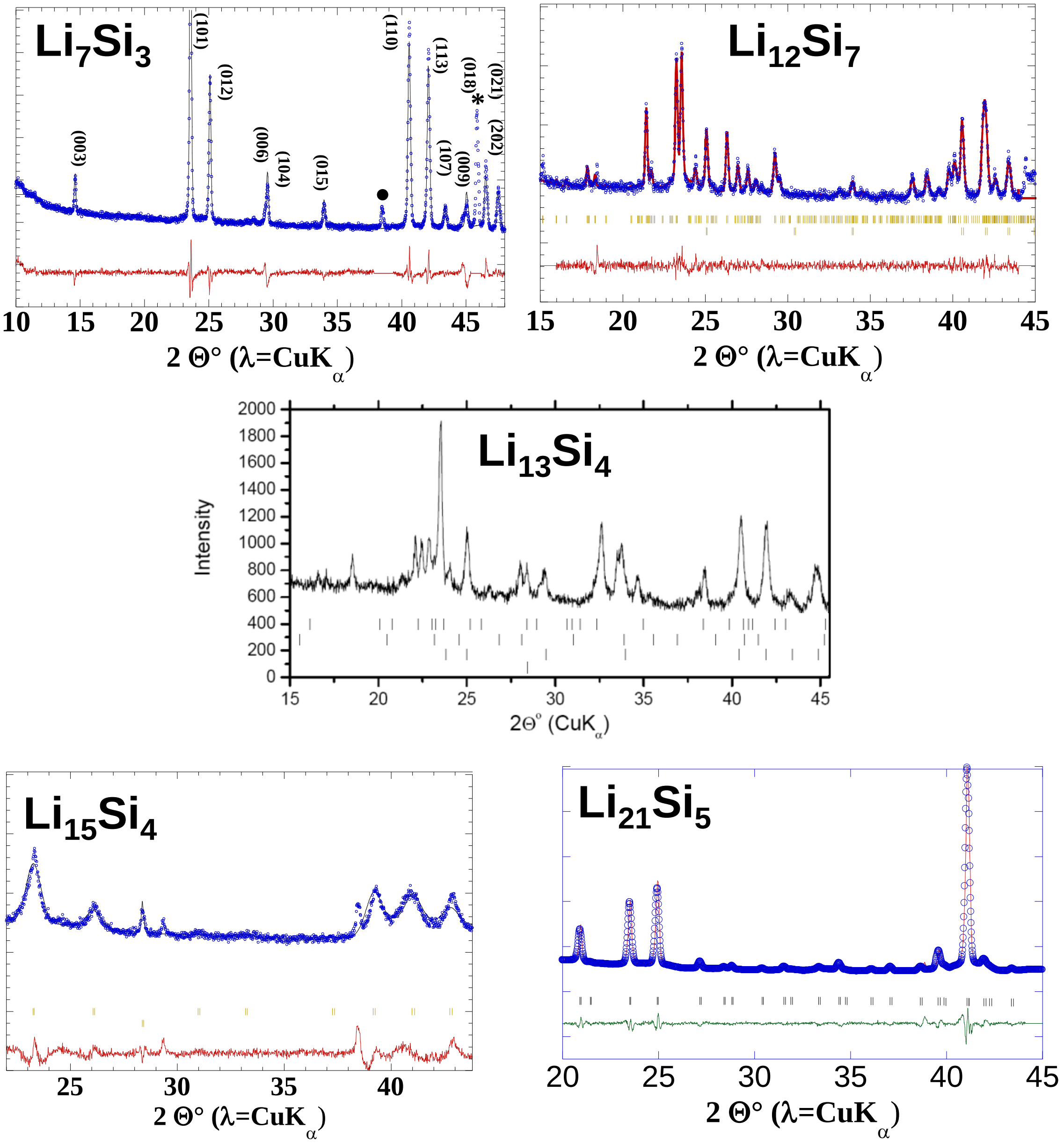

Figure 2.2. X-ray diffraction patterns of lithium silicide intermetallic compounds. Fittings of four of the patterns, performed using the *Fullprof* software in profile-matching mode, are shown; the difference between the experimental data and the fit is shown underneath each pattern. The tick marks represent the reflections for respective structure models and impurity phases. The 2nd set of tickmarks in $Li_{15}Si_4$ and $Li_{12}Si_7$ represent Si and Li_2Si. For $Li_{13}Si_4$, tickmarks are shown for the $Li_{13}Si_4$ (top; major phase), $Li_{21}Si_5$ (top middle), Li_7Si_3 (bottom middle) and Si (bottom); the remaining unindexed peaks correspond to unknown phases. * = Be; filled circle = Al.

2.3.2. NMR

The ^{7}Li MAS NMR spectra of the model compounds $Li_{12}Si_7$, to the increasingly lithium rich phases Li_7Si_3, $Li_{13}Si_4$, $Li_{15}Si_4$ and $Li_{21}Si_5$ are shown in Figure 2.3. These materials lie on the border between so-called Zintl phases and intermetallic compounds. Their structures cannot be easily rationalized by using simple Zintl-Klemm electron counting concepts, as discussed in a recent review [3], but contain additional orbital(s) delocalized over multiple lithium ions [3]. Theoretical studies help understand their electronic and crystallographic structures. These theoretical studies have shown that additional electron density is located in so-called "cage orbitals" that are distributed over numerous Li ions. For example, applying Zintl-Klemm ideas to $Li_{21}Si_5$ requires 20 electrons to form 5 Si^{4-} ions (completing the octet) leaving an excess of one electron per formula unit. Previous theoretical studies suggest that the material may be viewed as containing two types of units $[Li_{22}Si_4]^{4+}$ and $[Li_{20}Si_6]^{4-}$ [1,3] (Figure 2.1) the cage orbitals being located on some of the Li ions in the $[Li_{22}Si_4]^{4+}$ units. Among the known thermodynamic phases, $Li_{21}Si_5$ is the only phase that is reported to be metallic, the others being semiconductors [3]. The large shifts of the broad, overlapping resonances (at approx. 100 – 60 ppm) (Figure 2.3) seen in this material are ascribed to the Knight shift. The two dominant broad resonances in the spectrum of this material at 93.7 and 70.5 ppm are tentatively assigned to these Li ions in the 2 units, respectively, based on their relative intensities of these resonances, but further NMR shift calculations are required to validate this proposal. The weaker resonances centered at approx. 4.8 ppm are due to Li in more shielded and/or less metallic/semi-conducting environments and are ascribed to impurity phases. ^{7}Li-NMR pre-saturation experiments were performed to confirm this hypothesis, by irradiating either the 70 – 94 ppm peaks or the 4 – 0 ppm groups of peaks with a weak radio frequency field. This method saturates all the signals from environments that are in close spatial proximity (and thus magnetically coupled, e.g., via ^{7}Li-^{7}Li dipolar couplings). In either case, irradiation of one set of peaks (even for as much as 20 ms) did not affect the other set of peaks, suggesting that they are not part of the same phase. Although no impurity Li-containing phases were seen by XRD for this material phase, the presence of additional NMR resonances in its ^{7}Li spectrum is ascribed to amorphous components not seen by XRD, and the formation of new phases on partial exposure of the materials to trace amounts of oxygen that may have leaked into the rotor during the NMR experiment. We note however, that we were careful to examine the NMR spectra of all of the materials studied in this work immediately and then following more extended data acquisition, to ensure that the spectra presented in this paper were not affected by oxygen contamination. Furthermore, we ran the spectra of the model compounds and many of the battery samples discussed below on at least two occasions to ensure reproducibility. Only the spectra of $Li_{21}Si_5$ showed some evidence for possible contamination/decomposition of the sample.

All of the other lithium silicides exhibit resonances at much lower frequencies than those of $Li_{21}Si_5$, indicating quite different electronic properties (Figure 2.3). A clear trend is observed for these resonances, their shifts moving to lower frequencies as the Li/Si ratio increases and the shielding (electron density) on the Li ion increases. The most lithium deficient phase $Li_{12}Si_7$ gives rise to resonances centered at approximately 18.5 ppm. The peaks at 2 ppm and –17.6 ppm are ascribed to minor impurities, presumably amorphous phases. The spectrum is dominated by a narrow peak with a peak maximum at 18.5 ppm, which contains at least two overlapping resonances. The silicon ions in this material are present in either pentagonal rings or trigonal planar “star type” clusters with Si- Si bond distances of around 2.4 Å (Figure 2.1), resulting based on theoretical calculations, in two different clusters, $(Li^{6+}{}_{6}[Si_5]^{6-})_2$ and $(Li^{10+}{}_{12}[Si_4]^{10-})$ [2,3]. The two clusters are associated with *formal* charges of 1.0 and 0.83 of the Li^+ ions, which likely gives rise to a distribution of Li shifts and the two groups of resonances at 18.5 and 16.5 ppm, the more shielded Li environments presumably resonating at lower frequencies. Li_7Si_3 contains Si_2 dumbbells (Figure 2.1), the average partial charges on the Li ions decreasing [3,5], causing a shift of the center of mass of this spectrum to 16.5 ppm. According to Zintl electron counting rules, for the Si dumbbells with short Si-Si distances of only 2.323 Å (Figure 2.1), the partial formal charge of lithium ions in $Li_{14}{}^{12+}[Si_2]_3{}^{12-}$ system is +0.86 and this gives rise to slightly more shielded local lithium environments. $Li_{13}Si_4$ contains both Si-Si dumbbells and isolated silicon Si^{4-} ions [4] (Figure 2.1) and the shift of the NMR signal to lower frequencies (11.5 ppm) is consistent with the increase in the Li/Si ratio. Presumably a combination of slow lithium-ion motion, residual ^{7}Li dipolar coupling, and possibly disorder prevents resolution of the resonances from the three crystallographic sites. The NMR signal from $Li_{15}Si_4$ is not affected by the large Knight shifts that were observed in $Li_{21}Si_5$ spectrum. Instead, the homogeneous distribution of Si ions in the Li matrix gives rise to the most shielded Li environment(s) resulting in a broad resonance at 6.0 ppm. Thus, in conclusion, the most deshielded Li environments with peaks around 16-18 ppm are found in structures containing Si-Si bonds (rings/clusters/dumbbells), while the more shielded environments found for isolated silicon ions resonate at around 6.0 ppm, intermediate shifts being observed for compounds containing both types of structural motifs. These correlations are used in Chapters 3 and 4 to help elucidate the structural changes that occur on electrochemical lithiation of Si.

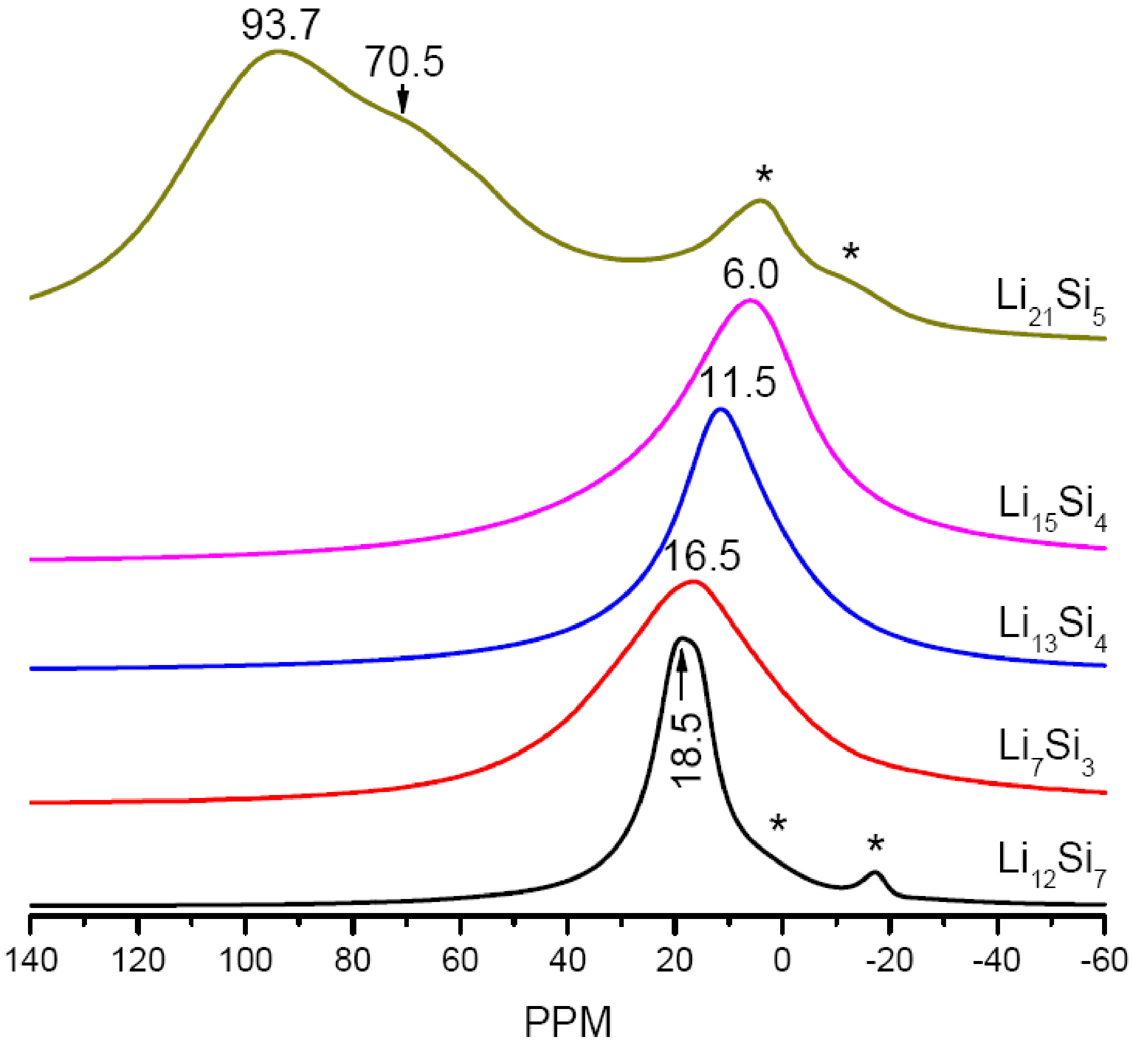

Figure 2.3. ^{7}Li MAS NMR spectra of $Li_{12}Si_7$, Li_7Si_3, $Li_{13}Si_4$, $Li_{15}Si_4$ and $Li_{21}Si_5$ at spinning speed of 38 kHz. Impurity phases are marked with asterisks (*).

The ^{29}Si NMR spectra of the crystalline lithium silicides and pure crystalline silicon (325 mesh) are shown in Figure 2.4. The pure silicon matrix spectrum contains only one resonance at -80 ppm due to one crystallographic Si site in the cubic structure. The silicon ions in this $Li_{12}Si_7$, on the other hand, are present in either pentagonal rings or trigonal planar "star type" clusters with Si- Si bond distances of around 2.4 Å (Figure 2.1), resulting in $(Li^{6+}{}_6[Si_5]^{6-})_2$ and $(Li^{10+}{}_{12}[Si_4]^{10-})$ clusters, therefore experience less shielding than Si in Si diamond matrix that give rise to ^{29}Si NMR shifts from 60 ppm to 360 ppm. The NMR spectra shows at least 7 sharp resonances due to 7 crystallographic sites for this phase. The electronic density transfer from Si ions to Li ions causes the deshielding as lithium content increases in the structure. Li_7Si_3, which has only 1 Si site and composed of Si-Si dumbbells with a distance of 2.332 Å (Figure 2.1), has a single ^{29}Si NMR resonance appearing at 337 ppm. The average shielding estimated from the electronic structure for this for this compound (with Li-Si cluster of $Li_{14}^{12+}[Si_2]_3^{12-}$) is lower than for $Li_{12}Si_7$ therefore the center of mass of the shift appears at a higher frequency compared to the center of mass of the shifts of $Li_{12}Si_7$. The trend observed for ^{7}Li NMR is reversed as expected in the case of ^{29}Si NMR. $Li_{13}Si_4$ which contains isolated Si and Si-Si dumbbells (Figure 2.1) gives rise to a broad range of resonances covering a frequency range from 750 to -350 ppm and a sharp resonance at 313 ppm. The former broad resonance is probably due to isolated Si while the latter is ascribed to Si-Si dumbbells. $Li_{15}Si_4$, on the other hand, consists only of isolated Si environments (Figure 2.1) and gives rise to an extremely broad resonance (1000 to -750 ppm) centered approximately at 250 ppm. In terms of silicon connectivity, $Li_{21}Si_5$ is similar to $Li_{15}Si_4$, and has isolated Si environments only. Thus, similarly, only a broad resonance centered at 277 ppm is observed for $Li_{21}Si_5$.

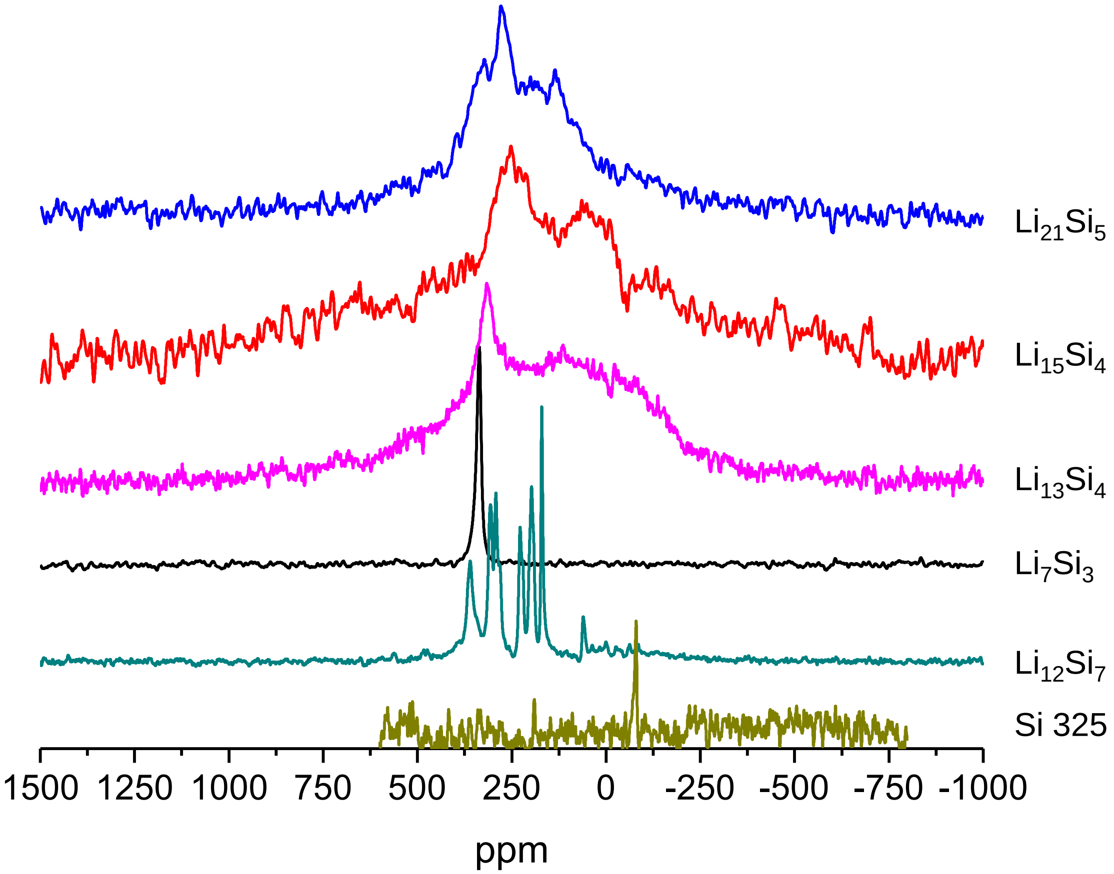

Figure 2.4. ^{29}Si MAS NMR spectra of lithium silicide model compounds and pure crystalline silicon.

2.3.3. PDF

The pair distribution function data of the selected model compounds is shown in Figure 2.5. The peaks appearing at less than 3.5 Å correspond to highly overlapping Li-Li, Li-Si and Si-Si closest contacts. High short and long range of crystalline model compounds results in distinguishable peaks between 2.0 Å and 3.0 Å. $Li_{13}Si_4$ and $Li_{15}Si_4$ which have isolated Si environments which are not bonded to any other Si produce a characteristic Si – Si atomic distance of 4.75 Å. $Li_{21}Si_5$ has a high Li content and no Si-Si bonding and thus the PDF pattern is dominated by wiggles (noise) and is poorest in quality. The major distinguishable bond distances are for Li-Si and Li-Li close contacts appearing at 2.5 and 2.8 Å. Si-Si ordering is not as evident for $Li_{21}Si_5$ as it is for all other model compounds. These observations agree with NMR studies on lithium silicides [11]. It must be noted that the presence of wiggles and noise becomes evident in lithium rich model compounds ($Li_{15}Si_4$ and $Li_{21}Si_5$) primarily because of a fluorescencing element at the X-ray energies used such as tungsten (possibly introduced into the sample in trace amounts during ball milling) which makes fitting the PDF for these phases difficult.

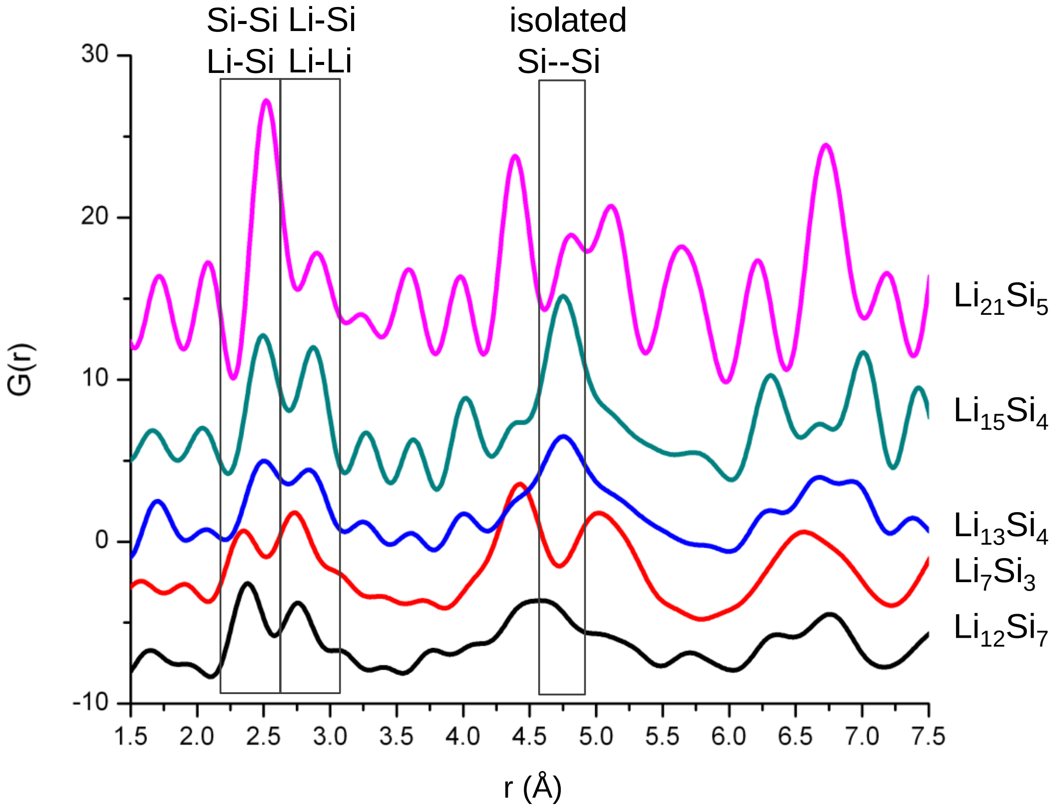

Figure 2.5. PDF patterns of lithium silicide model compounds. Sections indicate pair-pair correlation assignments.

2.4. Conclusions

Crystalline lithium silicides, $Li_{12}Si_7$, Li_7Si_3, $Li_{13}Si_4$, $Li_{15}Si_4$ and $Li_{21}Si_5$, have been synthesized from lithium and silicon precursors and characterized by solid state MAS NMR and X-ray PDF analysis. The local structure of crystalline model compounds has been investigated in order to construct a set of trends in lithium and silicon NMR signals, which in turn is used as a key to investigate the types of local structures of the phases observed in battery samples. The ^{7}Li NMR signal obtained by ex-situ MAS NMR has shown a clear trend; as lithium concentration increases the lithium signal shifts upfield. A similar and opposite trend is observed for the ^{29}Si NMR signal. The lithium environments around isolated silicon clusters and bonded silicon clusters have shown distinct shifts that are used to identify the type of local ordering in actual battery samples. The PDF studies have shown distinct local environments for Li-Li, Li-Li and Si-Si correlations. Li-Li and Li-Si correlations have been found to be in the range of 2.5-2.7 Å whereas Si-Si correlations, depending on the type of Si-Si bonding, found to vary between 2.33 Å and 4.75 Å. The metastable $Li_{15}Si_4$ phase and $Li_{21}Si_5$ have been found to contain no Si-Si direct bonding.

2.5. References

(1) Nesper, R.; Von Schnering, H. G. *J. Solid State Chem.* **1987**, *70*, 48.

(2) Nesper, R.; Von Schnering, H. G.; Curda, J. *Chem. Ber.* **1986**, *119*, 3576.

(3) Nesper, R. *Prog. Solid State Chem.* **1990**, *20*, 1.

(4) Frank, U.; Mueller, W.; Schaefer, H. *Z. Naturforsch., Teil B* **1975**, *30B*, 10.

(5) Klemm, W.; Struck, M. *Z. Anorg. Allg. Chem.* **1955**, *278*, 117.

(6) Stearns, L. A.; Gryko, J.; Diefenbacher, J.; Ramachandran, G. K.; McMillan, P. F. *Journal of Solid State Chemistry* **2003**, *173*, 251.

(7) Obrovac, M. N.; Christensen, L. *Electrochem. Solid-State Lett.* **2004**, *7*, A93.

(8) Morcrette, M.; Chabre, Y.; Vaughan, G.; Amatucci, G.; Leriche, J. B.; Patoux, S.; Masquelier, C.; Tarascon, J. M. *Electrochim. Acta* **2002**, *47*, 3137.

(9) Qiu, X.; Thompson, J. W.; Billinge, S. J. L. *J. Appl. Crystallogr.* **2004**, *37*, 678.

(10) Farrow, C. L.; Juhas, P.; Liu, J. W.; Bryndin, D.; Bozin, E. S.; Bloch, J.; Proffen, T.; Billinge, S. J. L. *J. Phys. Condens. Matter* **2007**, *19*, 335219/1.

(11) Key, B.; Bhattacharyya, R.; Morcrette, M.; Seznec, V.; Tarascon, J. M.; Grey, C. P. *Journal of the American Chemical Society* **2009**, *131*, 9239.

Chapter 3

Pair Distribution Function Analysis and Solid State NMR studies of Silicon Electrodes for Lithium-ion Batteries: Understanding the (De)lithiation Mechanisms

Abstract

Lithium-ion batteries (LIBs) containing silicon negative electrodes have been the subject of much recent investigation, because of the extremely large gravimetric and volumetric capacities of silicon. The crystalline-to-amorphous phase transition that occurs on electrochemical Li insertion into crystalline Si, during the first discharge, hinders attempts based on diffraction to link structure in these systems with electrochemical performance. Here, a combination of local structure probes, *ex-situ* ^{7}Li nuclear magnetic resonance (NMR) studies and pair distribution function (PDF) analysis of X-ray data was applied to investigate the changes in short range order that occur during the initial charge and discharge cycles. The distinct electrochemical profiles observed subsequent to the 1st discharge are been shown to be associated with the formation of distinct amorphous lithiated silicide structures. A (de)lithiation model consisting of four different mechanisms, each being valid for regions of the charge or discharge process is proposed to explain the hysteresis and the steps in the electrochemical profile observed during lithiation and delithiation of Si. A spontaneous reaction of the fully lithiated lithium silicide with the electrolyte is directly observed in the *in situ* NMR experiments; this mechanism results in self-discharge, and potentially capacity loss. The rate of this self-discharge process is much slower when CMC (carboxymethylcellulose) is used as the binder.

3.1. Introduction

Silicon anodes are attractive alternatives as anode materials for lithium ion batteries. Unlike carbon, the lithiation and delithiation mechanisms of Si are still unclear, due to the crystalline-to-amorphous phase transition that takes place during the 1st discharge of crystalline silicon[1,2], the inability of conventional characterization methods such as diffraction hindering research efforts to study the structures of these largely amorphous systems.

The approximate composition of the lithiated amorphous silicon phase has been extracted from *in situ* XRD studies and ^{119}Sn Mossbauer studies of Sn-doped silicon have been used to probe the local structure around Sn, and thus indirectly provide insight into the silicon local structures[1,3-5]. In the previous chapter (Chapter 2), by using *ex-situ* NMR, spectra from both the crystalline lithium phases within the lithium-silicon phase diagram and the amorphous lithiated phases are studied. It is demonstrated that the ^{7}Li NMR shifts found for the crystalline lithium silicide phases ($Li_{12}Si_7$, Li_7Si_3, $Li_{13}Si_4$, $Li_{15}Si_4$ and $Li_{21}Si_5$) are correlated with specific local environments (see Chapter 2), lithium ions nearby silicide clusters and isolated silicon anions giving rise to lithium resonances in distinct chemical shift ranges. $Li_{12}Si_7$ (containing $SiSi_3$ stars and Si_5 rings, Figure 3.1(b)) and Li_7Si_3 (Si-Si dumbbells/dimers, Figure 3.1(c)) give rise to ^{7}Li NMR resonances at approximately 18 ppm, while Li nearby the isolated Si ions found in $Li_{15}Si_4$ gives rise to signals at 6 to - 10 ppm, the exact value depending on the state of lithiation of this phase (Figure 2.3 [6]). The Li signal of $Li_{13}Si_4$, which contains both Si dumbbells and isolated ions, is at 12 ppm, intermediate between the two extremes. These shifts were then used to assign the lithium NMR resonances seen both *in situ* and from samples extracted from a battery at different states of charge (i.e., *ex-situ*). This information combined with the information gained from PDF analysis was used to gain insight into the lithiation mechanism of crystalline silicon during the 1st discharge and subsequent charge and discharge steps [6].

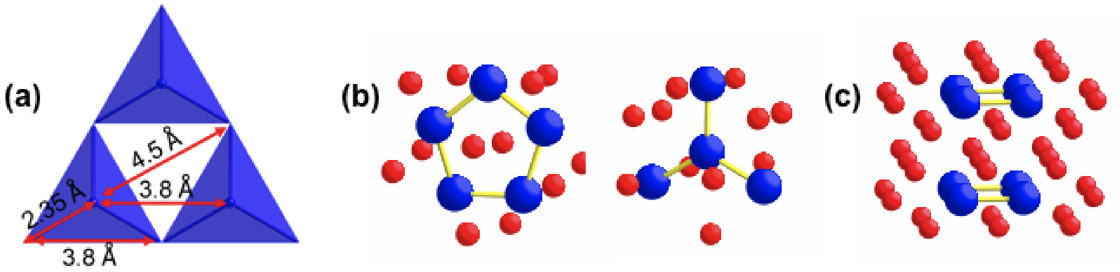

Figure 3.1. Local structures found in (a) crystalline silicon, (b) $Li_{12}Si_7$ (rings and $SiSi_3$ "stars") and (c) Li_7Si_3 (dimers). The closest Si – Si contacts are marked with arrows in (a). Blue and red balls represent Si and Li, respectively.

3.2. Experimental Methodology

3.2.1. Electrochemistry

A series of samples were prepared for *ex-situ* analysis by using 2032 type coin cells and by following a standard assembly procedure: The positive electrode was crystalline silicon powder (325 mesh, Aldrich), mixed with super P carbon in 1:1 weight ratio, and the negative electrode was lithium metal (0.38 mm thickness). 1 M $LiPF_6$ dissolved in a 1:1 volumetric mixture of anhydrous ethylene carbonate (EC) and anhydrous dimethyl carbonate (DMC) was used as the electrolyte (Merck, Selectipur^{TM}). A porous borosilicate glass fiber soaked with the electrolyte was used as the separator. The cells were assembled in an argon glove box and cycled galvanostatically either between 3.0 and 0.0 V or between 3.0 and 85 mV potential limits at a C/100 discharge rate with an Arbin Instrument galvanostat/potentiostat at room temperature. After electrochemical cycling, the cells were disassembled in the glove box where the active materials were extracted, dried and packed into 1.8 mm diameter zirconia rotors for MAS NMR analysis and into 1 mm diameter polyimide capillaries sealed with epoxy resin for x-ray scattering experiments at the synchrotron. The NMR spectra of the samples were run a few days after extraction. One 0 mV sample, called "0 mV washed", was extracted quickly from a cell and washed with DMC to investigate the lithium environments prior to any significant degradation of the lithium silicides, due to reactions with the electrolyte (a self-charge reaction). The second 0 mV "non-washed" sample was treated in the same manner as all the other higher voltage samples, a few hours passing between the end of discharge and the extraction of the sample from the battery. The PDF experiments were conducted days to weeks after the samples were extracted, and some so it is possible that some side reactions may have occurred.

3.2.2. Diffraction and PDF

Total scattering patterns (Bragg diffraction patterns and diffuse scattering data) were acquired with 2D detectors (GE a-Si and Perkin Elmer a-Si 2D image plates) at the Advanced Photon Source in Argonne National Lab, IL (60 and 90 keV beam energies). 2D images were converted into 1D Q-space vs. Intensity plots by FIT2D program by using CeO_2 calibration standard and PDF patterns (G(r)) were obtained with the PDFGetX2[7] software. The data range used was up to 23 A^{-1} Q. The PDFGui software[8] was used to fit the data. No attempt was made to subtract the PDF signal from the carbon and the binder.

3.2.3. NMR

3.2.3.1. *ex situ* NMR

^7Li MAS NMR spectra were acquired at 77.63 MHz using a CMX-200 MHz spectrometer, with a 1.8 mm MAS probe at a 38 kHz spinning speed. All the ^7Li spectra were referenced to a 1M LiCl solution at 0 ppm. Rotor-synchronized spin-echoes ($90^o – \tau – 180^o – \tau –$ acq) were used to acquire the spectra, where the values of τ were chosen, such that they were equal to the rotor period (i.e. $\tau = 1$ / spinning frequency). A recycle delay of 0.2 s was used to collect a total of 32000 scans for each sample. ^{29}Si MAS NMR spectra were acquired at 71.55 MHz using a CMX-360 MHz spectrometer with a 4.0 mm MAS probe at a 14 kHz spinning speed. The ^{29}Si NMR spectra were referenced to tetramethylsilane (TMS) (at 0 ppm) as an external reference. Spin-echoes ($90^o – \tau – 180^o – \tau –$ acq) were used to acquire the spectra. To enhance the signal-to-noise of some samples, the CPMG (Carr Purcell Meibohm and Gill) experiment [9], with a pulse sequence comprising of a series of spin-echoes ($90^o – \tau – n\times[180^o –$ acquisition$(2\tau)])$ was used. The number of 180^o pulses (n) was chosen to acquire the maximum number of echoes permitted by the spin-spin relaxation time (T_2). The sequence was rotor synchronized with the value of τ being chosen, such that it was equal to the rotor period (i.e. τ = 1 / frequency of spinning). A recycle delay of 1 s was used. The one pulse spectra took approximately 2 days to acquire, due to the low natural abundance of ^{29}Si (4.67%), the CPMG spectra taking only 36 hours. To maximize the signal-to-noise level, the spectral width of each spectrum was minimized so as to cover only the range containing the resonances.

3.2.3.2. *in situ* NMR

For the *in-situ* NMR studies, a flexible battery design, modified from Bellcore's plastic lithium-ion battery technology [10] was used. The positive electrodes were prepared by mixing 37:37:10:16 weight ratio of crystalline silicon (325 mesh, Aldrich), super P carbon, poly-vinylidene fluoride (PVDF) and dibutyl phthalate (DBP). The mixture was mixed with acetone to prepare a slurry, which was then spread evenly (1 mm) over a flat surface. The dried film of approximate 150 µm thickness (and area 12 x 10 mm) was then laminated on carbon coated copper wire mesh (by heating at 135 ^{o}C with 20 psi vertical pressure), leaving unlaminated copper mesh at one end to serve as the battery leads. A small strip was cut from the larger electrode with area approximately 3 x 10 mm. The negative electrode was prepared by pressing lithium metal (0.38 mm thickness) onto copper wire mesh, in a glove box, again leaving bare copper mesh for the battery leads (Figure 3.2 (a)). The electrolyte used in this study was 1 M $LiPF_6$ dissolved in a 1:1 volumetric mixture of anhydrous ethylene carbonate (EC) and anhydrous dimethyl carbonate (DMC). A porous glass fiber soaked with the electrolyte was used as a separator.

The cell components were assembled in a polyethylene bag (Figure 3.2 (a)) which was hermetically sealed inside an argon glove box. The final dimensions of the cell electrodes were 10 x 4 mm (area) x approx. 2 mm (height). The flexible cell was then placed tightly inside the 5 mm coil of a conventional CMX static probe (Figure 3.2(b)). An Arbin Instruments galvanostat/potentiostat was used for cycling the battery *in-situ*. Low pass filters (50 MHz) were used to filter the high frequency noise coming from the cycler to improve the signal to noise ratio of the NMR spectrum [10]. The *in-situ* cell was cycled galvanostatically between 3.0 and 0.0 V during the spectral acquisition.

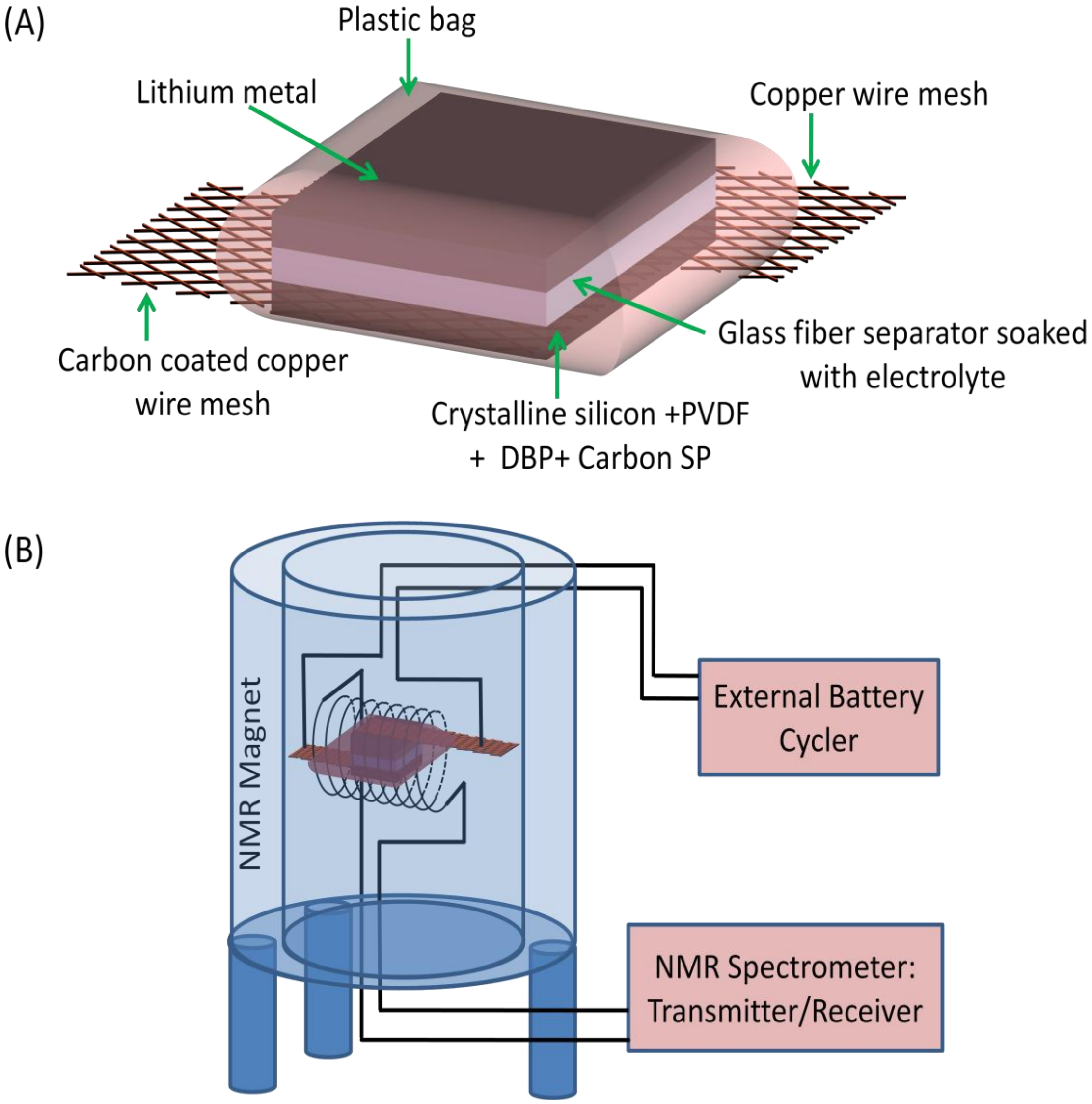

Figure 3.2. (a) The schematics of the flexible plastic battery used for the *in-situ* static NMR experiment and (b) the in-situ static NMR setup

3.3. Results and Discussion

3.3.1. Electrochemistry

3.3.1.1. Galvanostatic Cycling

An electrochemical profile that is typical of those from samples extracted from a series of different batteries is presented in Figure 3.3. The 1st (irreversible) process that occurs at approx. 0.8 V is primarily due to the reaction with the carbon in the Si/C composite. The lithiation of pristine crystalline silicon is accompanied by a long flat (slightly decaying) voltage region at approximately 125 mV. A non-stoichiometric $Li_{15+\delta}Si_4$ metastable phase has been shown to crystallize at the end of the 1st discharge, i.e., on discharging to below 50 mV [1,6,11]. The subsequent charge (Fig. 3.3a) is associated with a single, long plateau-like region at approximately 375 mV [1]. Galvanostatic intermittent titration technique, GITT, experiments (see the subsequent section, 3.3.1.2), demonstrate that the processes on both discharge and charge are not true plateau, but are rather associated with gradual, sloping potentials. Two distinct processes are seen in the 2nd discharge profile of silicon (Figure 3.3a), at approximately 250 mV and 100 mV, consistent with previous results [2] and GITT results (see the subsequent section, 3.3.1.2). The origin of these two processes is still not understood. Previous ^{119}Sn Mossbauer spectroscopy of Sn-doped amorphous Si electrodes, materials that also show steps in the voltage composition curve, may provide indirect insight into the Si processes:[4] at a composition of $Li_{2.3}Si$ (at the end of the 1st process) the environment of the Sn becomes more symmetric, suggesting that each Sn (and thus *possibly* Si) atom is surrounded by only Li ions – i.e., no clusters or Si-Sn directly bonded contacts remain.

Full lithiation during the 2nd and any subsequent discharges to 0 V (Figure 3.3a) results in the crystallization of the non-stoichiometric $Li_{15+\delta}Si_4$ metastable phase, and a charge profile that is similar to that seen on the 1st charge. A charge profile following a partial discharge to 85 mV (Figure 3.3b) now results in two processes centered at 300 mV and 450 mV in the electrochemical profile, which can also be resolved in the GITT measurements (see the subsequent section, 3.3.1.2) and whose origin again remain unclear. To throw some light into these issues, two series of samples were investigated with NMR and PDF, the 1st to investigate the structural changes that occur following full discharge and charge steps, and the 2nd to explore the effect of partial discharge to 85 mV.

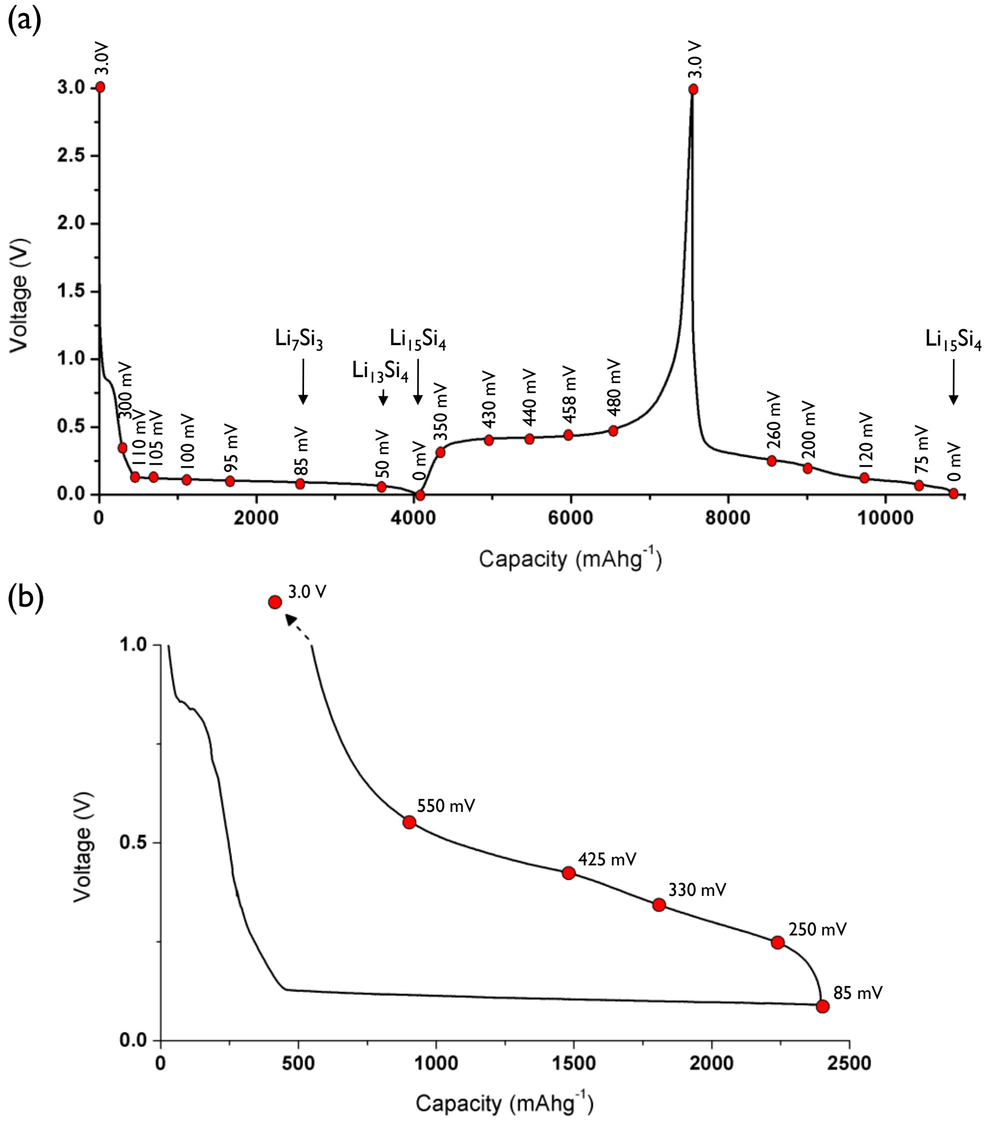

Figure 3.3. (a) The electrochemical profiles for the 1st discharge, 1st charge and 2nd discharge of crystalline silicon (voltage cutoffs between 3 V and 0 V and with a C/100 current rate; approximate lithium silicide compositions are marked with arrows). (b) The electrochemical charge profile following partial discharge to 85 mV. The last data point is collected at 3.0 V for (b), but the y-axis is limited to 1 V so as to observe the two distinct processes more clearly. The red points indicate the samples collected for *ex-situ* PDF and NMR studies.

3.3.1.2. GITT measurements

GITT method is used to reveal electrochemical processes that are hidden due to overpotential. Figure 3.4 shows the electrochemical GITT experiment profile of crystalline silicon, cycled between 3 V and 0 V. A single discharge potential process centered at approximately 125 mV and a single charge process centered at approximately 375 mV is observed for the 1st cycle. Two discharge processes of equal length are observed during the 2nd discharge, which are centered at approximately 250 mV and 100 mV respectively. The 2nd discharge is followed by a single charge process identical to that observed in the 1st charge. Subsequent cycles are found to be identical with the 2nd cycle. Although the different processes are associated with distinct potentials, the potentials are not flat and hence these are not true plateau. This is perhaps not surprising since all of these processes involve insertion between at least one amorphous phase, namely a phase with a distribution of local environments.

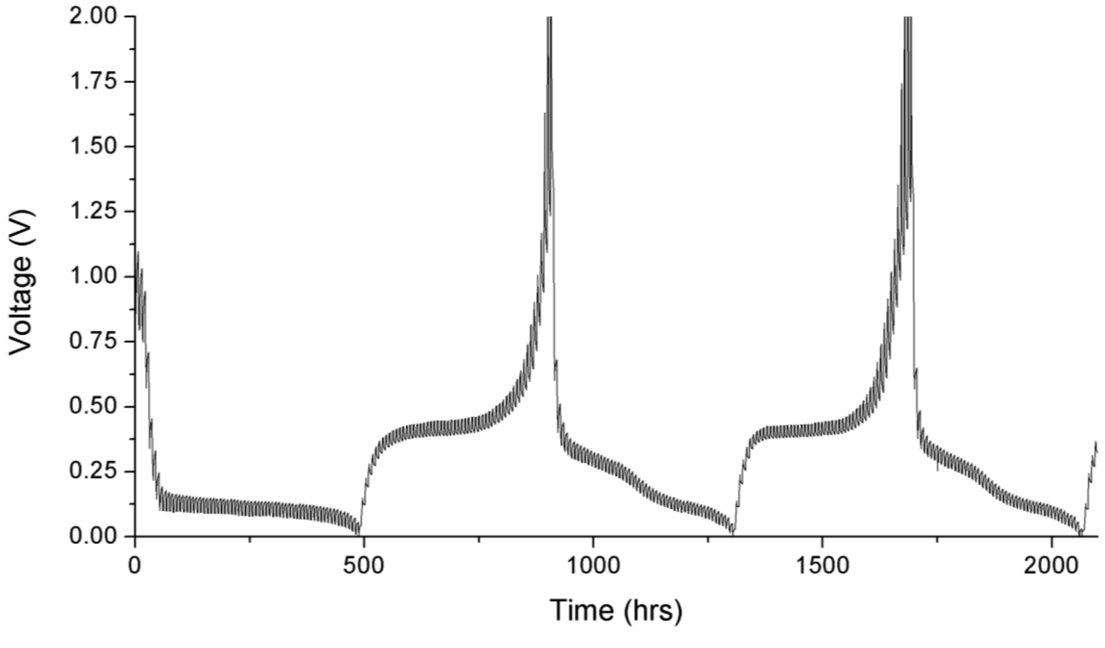

Figure 3.4. Electrochemical profile of crystalline silicon cycled vs. lithium metal between 3 and 0 V with GITT cycling conditions (2 hour cycling at C/75 regime followed by 5 hour rest period)

Figure 3.5 shows the electrochemical GITT experiment profile of crystalline silicon, cycled between 3 V and 85 mV. A single discharge process centered at approximately 130 mV, followed by two charge processes of equal length centered at approximately 250 and 375 mV, are observed for the 1st cycle. Two discharge processes of equal lenght are observed during the 2nd discharge, which are centered approximately at 250 and 100 mV respectively. The 2nd discharge is followed by a single charge process identical to the 1st charge. Subsequent cycles are found to be identical with the 2nd cycle.

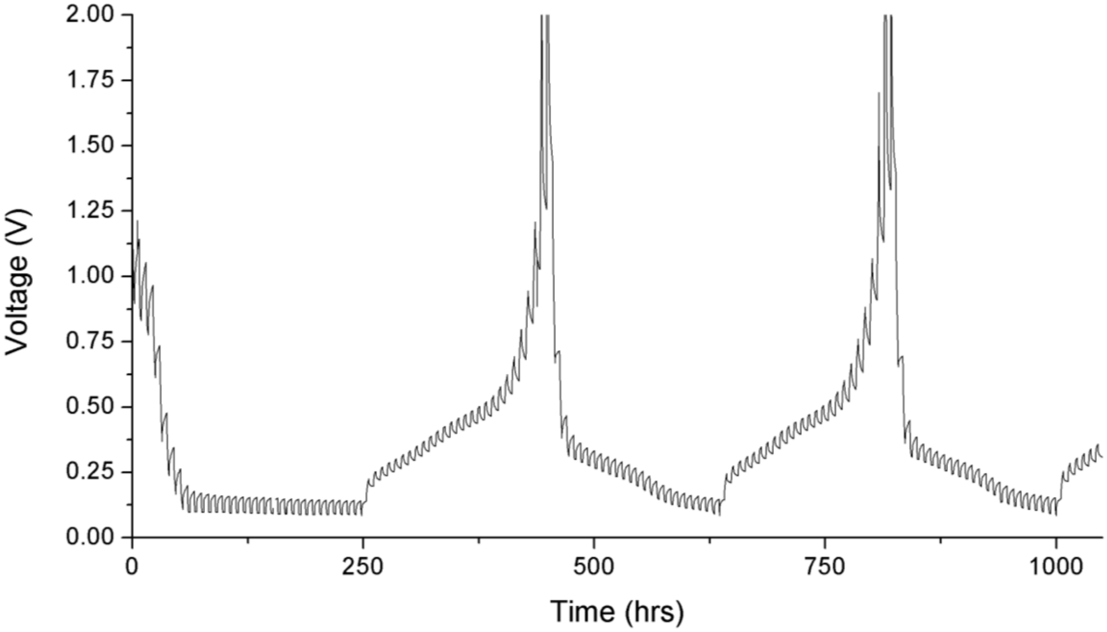

Figure 3.5. Electrochemical profile of crystalline silicon cycled vs. lithium metal between 3 V and 85 mV with GITT cycling conditions (2 hour cycling at C/75 regime followed by 5 hour rest period)

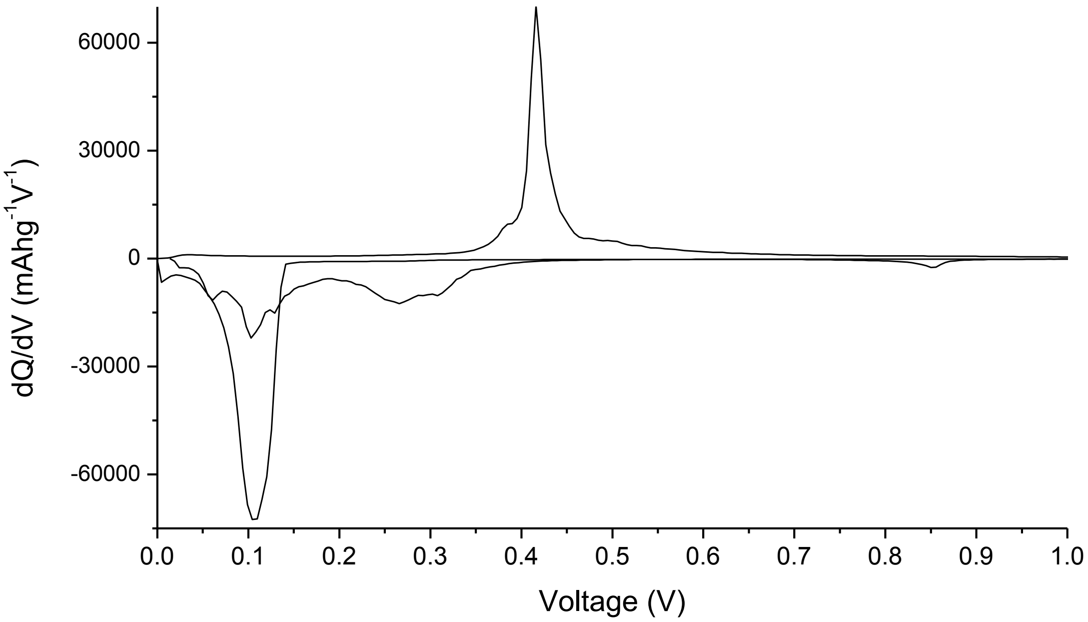

Figure 3.6. Plot of differential capacity vs. potential for the 1st full discharge, 1st full charge and the 2nd full discharge of crystalline silicon

3.3.2. PDF and NMR Studies

In the current work, a combination of *ex-situ* ^{7}Li MAS NMR and X-ray PDF analyses was used to study the 1st and 2nd cycles, and identify local structures that are correlated with specific electrochemical signatures. Joint magic angle spinning (MAS) nuclear magnetic resonance (NMR) spectroscopy and X-ray and neutron pair distribution function (PDF) analyses have recently been successfully used to investigate short range order in lithium ion battery electrode materials [6,12-16]. The combination of the two techniques should allow for an in depth analysis of lithiation and delithiation mechanisms. Although X-rays are less sensitive to light elements, due to the Z dependence of x-ray scattering lengths, the X-ray PDF method will be sensitive to correlations involving silicon. By using a second local structure probe, PDF, the aim is to extract further details concerning the silicon environments, in order to support the lithium NMR results, which provide information concerning the local structures centered around lithium. Then this information is combined to construct a model of lithiation and delithiation of silicon in the 1st and subsequent charge-discharge cycles.

3.3.2.1. *ex situ* ^{7}Li MAS NMR (1st discharge)

To investigate the different voltage regions upon 1st discharge in detail with ^{7}Li MAS NMR spectroscopy, nine coin cells composed of crystalline silicon as the positive electrode and lithium metal as the negative electrode were stopped at different potentials and the electrode materials were extracted (Figure 3.7). The batteries arrested at 300 and at 110 mV, give rise to a resonance at -0.3 ppm (Figure 3.7), which is assigned to diamagnetic environments for Li in carbon (Li_xC), in the (dried) electrolyte solution, in the solid electrolyte interphase (SEI) and possibly in environments created due to reaction with oxides on the surface of the silicon. The -0.3 ppm resonance is present in NMR spectra of all of the electrode samples extracted from actual batteries (Figure 3.7).

Below 110 mV, the reaction of crystalline silicon with lithium takes over and new ^{7}Li resonances start to appear (Figure 3.7). At 105 mV (250 mAhg^{-1}, after the capacity of the carbon process has been accounted for; i.e., 0.26 Li inserted per Si) two distinct peaks are observed at 18.0 and 6.0 ppm, which are assigned to lithium ions surrounding small Si clusters (i.e., structures containing Si-Si bonds as found in chains/rings/dumbbells) and lithium ions near isolated silicon ions, respectively, which are formed on breaking up the crystalline silicon diamond structure. Based on the sizes of the clusters in the model compounds, and the similarity of their NMR shifts to those seen here, this suggests that clusters first formed on lithiation similarly contain 2 – 5 silicon atoms. Based on the relative areas of the two resonances, lithium ions nearby the isolated silicon ions dominate over Li nearby Si-Si clusters. On further lithiation, the 18 ppm peak grows significantly until a potential of 95 mV is reached (1200 mAh/g, 1.25 Li inserted per Si) whereas the 6.0 ppm peaks grows only slightly, suggesting that both isolated silicon and the clusters form right in the beginning of the formation of the amorphous phase, but that as the lithiation continues, the rupturing of the Si lattice proceeds via the formation of smaller clusters. After 95 mV, the 18 ppm peak starts to shift to lower frequencies and decreases in intensity. This is consistent with the reaction of the Si-Si clusters with further Li to form more isolated Si ions. The presence of both clusters and isolated silicon anions in the 50 mV sample is consistent with the estimated Li content of the amorphous phase ($Li_{3.4\pm0.2}Si$), which based on the structure of the model compound with the closest lithium content, $Li_{13}Si_4$, will contain both these species. As the lithiation proceeds below 50 mV more Si-Si bonds are broken and the spectrum of the sample extracted from the 0.0 V battery (3600 mAh/g, 3.75 Li inserted per Si), is dominated by the resonance at 6.0 ppm due to the isolated Si ions, consistent with the formation of the crystalline $Li_{15}Si_4$ phase (Figure 3.7).

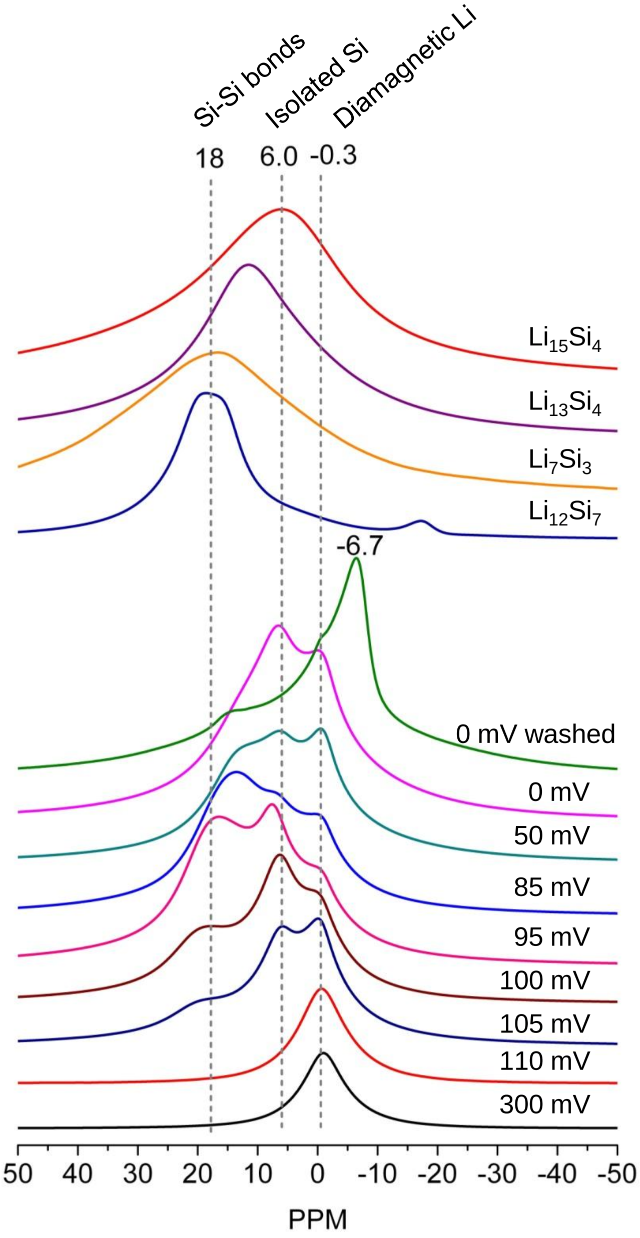

Figure 3.7. *ex situ* ^{7}Li NMR of battery samples stopped during the 1st discharge of crystalline silicon. (Figure adapted from that shown in reference [6]) Two samples were prepared at 0 mV, the one entitled “0 mV washed” corresponding to a sample extracted very rapidly from a cell and washed, so as to limit the side reactions that are prevalent in this system, particularly for the fully lithiated phases.

3.3.2.2. PDF (1st Discharge)

The PDF studies of the crystalline lithium silicide phases clearly show distinct Si-Si and Li-Si atom-atom correlations, and thus, interatomic distances (see Chapter 2). The data do show a noticeable decrease in the Si-Si bond distance of Li_7Si_3, the phase that contains Si-Si dimers with multiple bond character (see Chapter 2, 2.380 Å for $Li_{12}Si_7$, 2.345 Å for Li_7Si_3). A more detailed direct analysis of Si-Si and Li-Si correlations was, however, attempted for the 1st discharge of crystalline silicon (Figure 3.8). While only the correlations to 9 Å are plotted Figure 3.8, for the crystalline Si starting material, a series of correlations are observed that extend out to more than 40 Å. The first, second and third peaks, at 2.35, 3.8 and 4.5 Å correspond to the Si-Si bonds, the Si-Si contacts within the silicon tetrahedra (Si tet), and the Si-Si contacts between tetrahedra of the silicon diamond structure (Figure 3.1), respectively. As the discharge proceeds, the intensity of all the Si-Si peaks decreases, but the correlations between more distant Si atoms decrease much faster than the correlations due to directly bound Si, and Si in the 2nd coordination shell.

On discharging to 50 mV, all of the correlations at 4.5 Å have essentially disappeared, while the peaks at approximately 2.35 (Si-Si) and 3.8 Å (Si tet.) still remain. The total loss of long-range order indicates that almost complete amorphization of crystalline silicon lattice occurs beyond 85 mV. The presence of the 1st two correlations, but the absence of the 4.5 Å peak, suggests that while some silicon tetrahedra or other smaller clusters remain, the long range correlations between tetrahedra are destroyed. The 2.35 Å (Si-Si) correlation has shifted to 2.27 Å indicating significant Si-Si multiple bond character, and thus that a large contribution to this correlation now most likely originates from Si-Si dimers.

The appearance of a broad peak at 4.75 Å in both the “washed” and “non-washed” 0 mV samples is due to non-bonded Si – Si correlation, while the weak peak at 2.85 Å is ascribed to Li-Si correlations, both being consistent with the formation of a $Li_{15+\delta}Si_4$-like phase at the end of the 1st long plateau-like region. Si correlations are also present indicating incomplete reaction of some of the Si in this sample. Both samples produced similar PDF patterns indicating similar local structures. Clearly the relaxation process seen by NMR, due to the side reactions with the electrolyte, does not significantly affect the silicon correlations. Since differences between the relaxed and non-relaxed samples likely arise from disorder in the lithium sub-lattice, a future neutron PDF study may provide more insight into the structure of the lithium sublattice and any disorder.

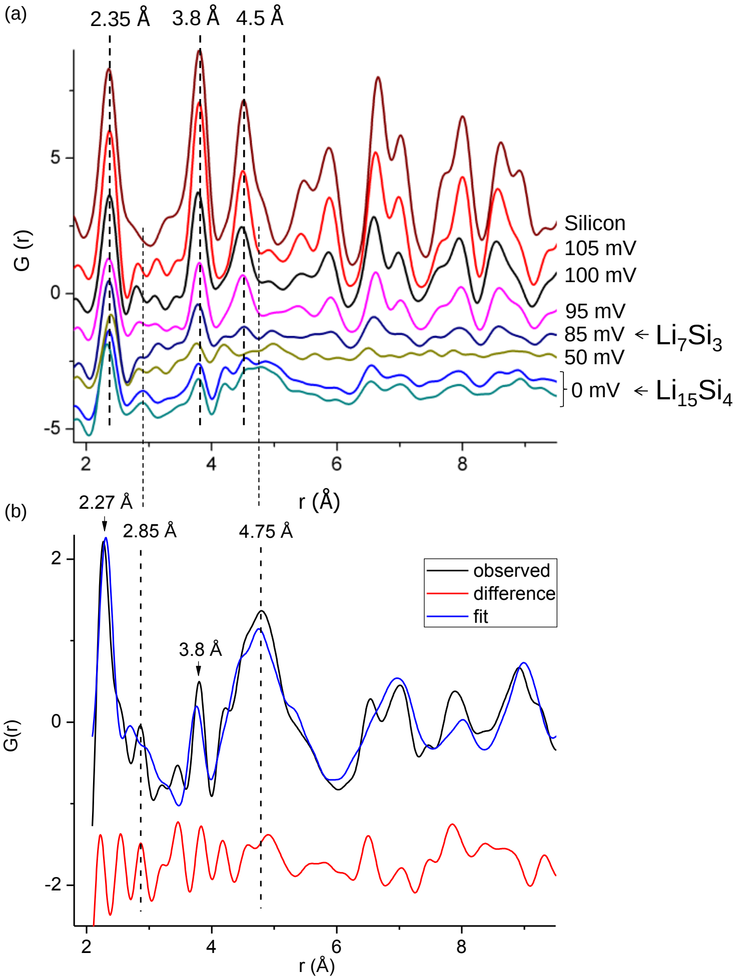

Figure 3.8. (a) *ex situ* Pair distribution function of battery samples collected during the 1st discharge. The dashed lines correspond to the 1st, 2nd and 3rd coordination shell Si—Si distances in a Si diamond matrix. Two 0 mV samples are included, the data shown in blue (top) representing the unwashed sample while the data shown in teal (bottom) represents the washed sample. Approximate lithium silicide compositions are marked with arrows. (b) PDF data and fit (R_w= 43%) of the washed 0 mV sample. The dashed lines at 2.85 and 4.75 Å, connecting (a) and (b), show characteristic $Li_{15}Si_4$ correlations.

The integrated areas under the 2.35, 3.8 and 4.5 Å peaks are plotted in Figure 3.9. Although the closest two Si-Si contacts still remain at the end of the discharge, the 3.8 Å Si-Si correlation, which corresponds to the edge of a Si tetrahedron (Figure 3.1) is almost completely lost. These peaks are the weakest in the battery discharged to 50 mV, which may reflect more complete reaction of the Si in this particular battery, due to a better cell construction. In contrast, the batteries discharged to 0 V contain unreacted Si, either due to poor cell construction. In addition, some decomposition of the $Li_{15}Si_4$ phase formed at this state of discharge, before the battery could be disassembled, or in the polyimide tubes used in the PDF experiments likely occurs, these side-reactions may possibly reform some Si-Si species, a phenomenon that is noted in the *in situ* NMR section (see section 3.3.2.4) [6]. A fit to the PDF data of the 0 mV sample (washed), performed using the crystalline structure of $Li_{15}Si_4$ is acceptable (Figure 3.8b) for distances greater than 3.8 Å; it is clear, however, that the crystalline structure does not capture all of the local distortions in this phase and the material appears to contain considerable disorder. In order to provide an acceptable fit at short distances, silicon has been introduced as a second phase, but with a very large damping factor of 5.32 Å. The factor, which is also called nanoparticle amplitude correction parameter, dampens the calculated PDF appropriately according to the refined average nanoparticle diameter. This factor indicates that there are silicon-like clusters, which are on average no greater than 5.2 Å in size. There is also some residual crystalline Si, which can be seen in the difference plots, at longer distances (e.g., the peak at 6.5 Å).

In order to provide further insight into the mechanism by which silicon reacts with lithium, the theoretical decreases in the intensities of the 1st three PDF correlations, if Si were to react via the two reactions,

(i) $7\,Li + 3\,Si \rightarrow Li_7Si_3$, ($Li_{2.33}Si$),

(i.e., to form the phase containing $[Si{=}Si]^{4-}$ dumbbells, Figure 3.1 (c)), and

(ii) $15\,Li + 4\,Si \rightarrow Li_{15}Si_4$

(green dashes), are plotted (Figure 3.9). The first reaction should, in principle, be complete at a theoretical capacity of 2340 $mAhg^{-1}$, at which point Si-Si 2.35 Å correlations should still be present with approximately one quarter of the intensity of the same correlation in pristine Si. Alternatively, the direct, two-phase reaction of Si to form $Li_{15}Si_4$ should lead to a monotonic, simultaneous decrease of all of the Si – Si correlations along the path of the green dashed line. Except perhaps in the initial stage between 110 and 105 mV, where no clear difference (within the signal-to-noise ratio) is observed in the rate of change in the intensity of the 1st three correlations, both proposed reaction mechanisms do not describe the experimental change in intensity of the Si correlations, on discharge. The PDF data of the 100 and 85 mV samples (i.e., prior to approximately 2500 $mAhg^{-1}$) indicate that Si proceeds via the formation of clusters rather than the formation of isolated Si ions *only*, since the longer-range, non-bonded correlations drop more rapidly than expected for reaction (i). The decrease of the correlations is similar, or even larger, than predicted by a model wherein Si reacts directly to form Li_7Si_3 (reaction (ii)) until after 95 mV. Thereafter, the absolute numbers of both the 2.35 and 3.8 Å correlations are larger than predicted by the "Li_7Si_3" model. The behavior after 95 mV suggests that either (a) side-reactions occur, so that the reaction proceeds more slowly than indicated by the current measured via the electrochemical measurements, and/or (b) clusters that are larger than a simple dumb-bell are also present. Larger clusters are likely to be responsible for weaker correlations at 3.8 and 4.2 Å. For example, the Si – Si distances in the 4 membered $Si(Si)_3$ "stars" in the crystalline material $Li_{12}Si_7$ (Figure 3.1 (b)) contain Si-Si non-bonded distances of 4.05 – 4.19 Å, and thus may contribute to the intensity of the 4.2 Å correlations. Assuming that the side-reactions are not significant, at least above 50 mV, then if the cluster hypothesis, (b), holds true, at 85 mV (i.e., at approximately the Li_7Si_3 stoichiometry) these clusters must also be accompanied silicon environments that are richer in Li (i.e., environments that contain more Li in their local coordination shell, as found for isolated Si ions) than present in the thermodynamic phase for this composition (Li_7Si_3). Since the Li rich regions or clusters are in a more reduced state, this either implies a degree of compositional inhomogeneity across the electrode, or that the activation energy associated with Si-Si bond-breaking is not sufficiently large to allow the system to reach local equilibrium, so that non-equillibrium structures (clusters) can persist, even in close proximity to each other. Most likely, both are true for this system.

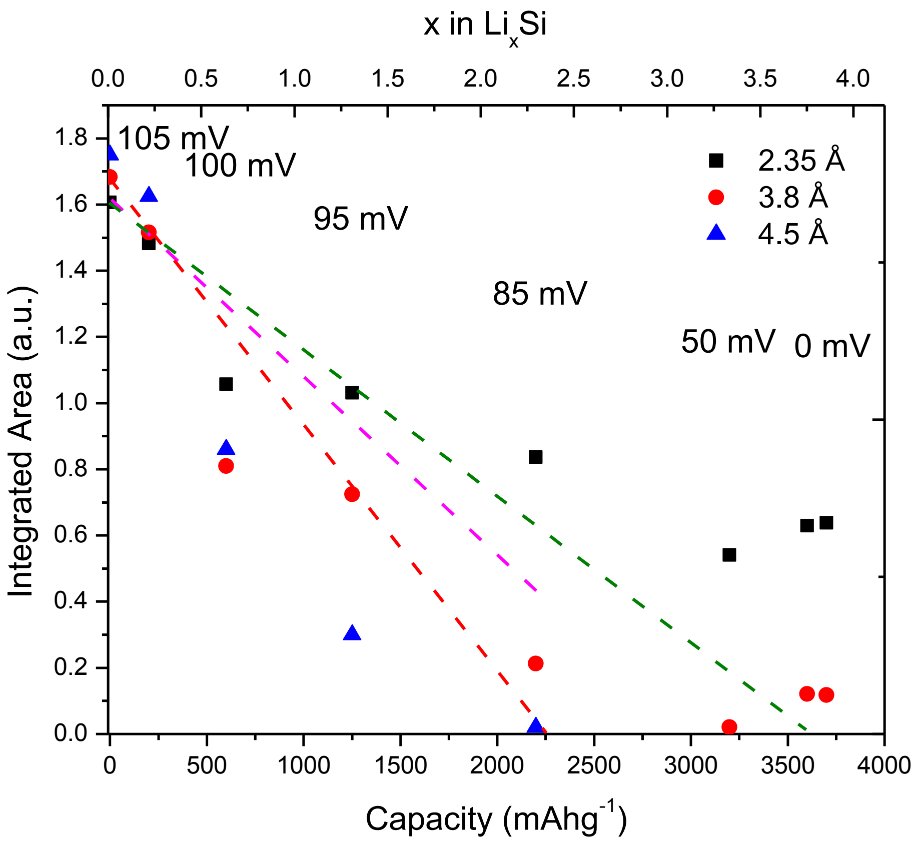

Figure 3.9. Integrated area under the peaks from the 1st and 2nd Si-Si coordination shells, obtained from PDF of battery samples stopped during the 1st discharge at different indicated potentials. (For the two samples stopped at 0 mV >3500 mAhg^{-1}, the points on the left and right correspond to the unwashed and washed electrode, respectively). The green dashed line indicates the intensity loss predicated for both the 2.35 and 3.8 Å peaks assuming a 2 phase reaction from crystalline silicon to the $Li_{15+\delta}Si_4$ phase, while the magenta and red dashed lines correspond to the intensity loss predicted for the same two correlations, respectively, for a two phase reaction to form the Li_7Si_3 phase.

3.3.2.3. Discussions on the NMR and PDF data

The PDF results are now compared with the previous NMR results *on the same samples:* Two ^{7}Li NMR resonances were seen for the 105 mV sample at 18 and 6 ppm suggesting the presence of Li nearby Si-Si clusters (18 ppm) and Li nearby isolated silicon clusters (6 ppm). Both these resonances gain in intensity until 95 mV. If the system followed the thermodynamic pathway, *i.e.*, phases with small clusters were formed 1st, then no resonance at 6 ppm would be expected during this stage of the reaction. The PDF data of the 105 mV sample is in agreement with the NMR data at this point, and suggests the formation of both clusters and isolated Si ions, since the 1st three correlations appear to decrease in intensity together. The subsequent PDF data of the 100 and 95 mV samples do, however, suggest that lithiation of Si is largely proceeding via the formation of clusters, since the longer-range correlations drop more rapidly than the shorter-range correlations. This is consistent with the change in Li-NMR intensities seen in the 100, 95 and 85 mV spectra, where the Li cluster resonance is seen to grow more rapidly than the resonance due isolated Si. Note also that the NMR spectra, since they detect Li ions, will provide differently-weighted information than the PDF data: An isolated silicon anion will be surrounded by approximately 4 Li ions (3.75 in the $Li_{15}Si_4$ phase), while a silicon ion in the $Li_{12}Si_7$ or Li_7Si_3 phase will be nearby only 1.75 – 2.33 Li ions; more extended Si clusters will be nearby even fewer Li ions. Thus, the NMR data will overestimate the number of isolated anions. The significant concentration of Li nearby clusters in the 85 – 50 mV samples, as seen by NMR, is consistent with the PDF G(r), where Si-Si bonds are still observed. At the end of the 1st discharge, the ^{7}Li NMR spectra indicate that the sample is predominantly composed of Li nearby isolated silicons ions, again consistent with the PDF data.

3.3.2.4. *in situ* ^{7}Li static NMR and investigation of non-stoichiometry of the fully discharged phase

In order to directly monitor the changes that occur in the LIB in real time, a flexible *in-situ* crystalline silicon vs. Li/Li^+ battery (Figure 3.2 (a) and (b)) was fully discharged and then charged, with a C/75 rate, in a conventional static NMR probe, during ^{7}Li NMR data acquisition (Figure 3.10). A recycle delay of 0.2 s was chosen since it partially suppresses the signal from the diamagnetic Li due to salts in the electrolyte.. The initial spectrum at the beginning of the electrochemical cycle shows four small peaks at around at 0 - 8 ppm (Figure 3.10 (A1)). The smallest feature at lower frequency is due to the lithium ions in the electrolyte solution (black), and the two peaks (light blue and green) at higher frequencies are ascribed to lithium in passivation (SEI) layers on both the positive and negative electrodes [17] and in Li_xC (see subsection 3.3.2.4.1 for a fuller discussion concerning the peak fitting). Upon discharging, a broad peak appears at around at 18 ppm at approximately 500 $mAhg^{-1}$ (i.e., immediately following the carbon process), which is ascribed to the formation of small silicon clusters. The peak grows and shifts to lower frequencies along the electrochemical plateau until 0.08 V, where it reaches 14 ppm (2500 $mAhg^{-1}$, Figure 3.10 (A2)). A resonance is also observed at approx. 4.5 ppm, which grows steadily with time, particularly from 0 to 1250 $mAhg^{-1}$. This peak (magenta in A1-A3) is ascribed to the formation of isolated silicon clusters, but it also contains an (overlapping) contribution from resonances due to the SEI/Li_xC Li environments. The much stronger intensity of the 4.5 ppm resonance over that from the 18-14 ppm resonance in the range from 100 mV to 50 mV (see Figure 3.10 A1, A2 and A3) reflects the dominance of the formation of isolated Si atoms over the formation of Si-Si clusters. Even though the resolution is poorer in the static mode, as compared to the MAS NMR spectra, the data largely agrees with the *ex-situ* data, until close to the end of the discharge. The small shifts of some of the resonances between the two methods are ascribed to (a) the fact that the static peak maximum does not always correspond to the isotropic shift and (b) small susceptibility shifts of the ^{7}Li signals due largely to the presence of metal components in the LIBs such as the Li metal and current collectors.

At the bottom of the discharge (below 30 mV), i.e., when the crystalline phase $Li_{15}Si_4$ is seen by XRD, a new peak appears at -10 ppm (Figure 3.10 (A3)); this is accompanied by the loss of intensity of the 17 ppm resonance, and a noticeable slowing down of the growth in intensity of the 4.5 ppm resonance. The negative shift suggests the formation of a highly shielded lithium environment (relative to the environment of the reference Li environment, Li^+ (aq), which resonates at 0 ppm). The intensity of the -10 ppm resonance is enhanced relative to the other resonances due to the short relaxation time of this signal (approx. 33 ms). The intensity of the -10 ppm peak decreases extremely rapidly upon charging the battery in the *in-situ* NMR experiments, and upon removing only approx. 0.16 Li per formula unit (150 $mAhg^{-1}$) the voltage has increased to 300 mV and the intensities of both the resonances at approximately 4.5 and 17 ppm increase (see section 3.3.2.4.1).

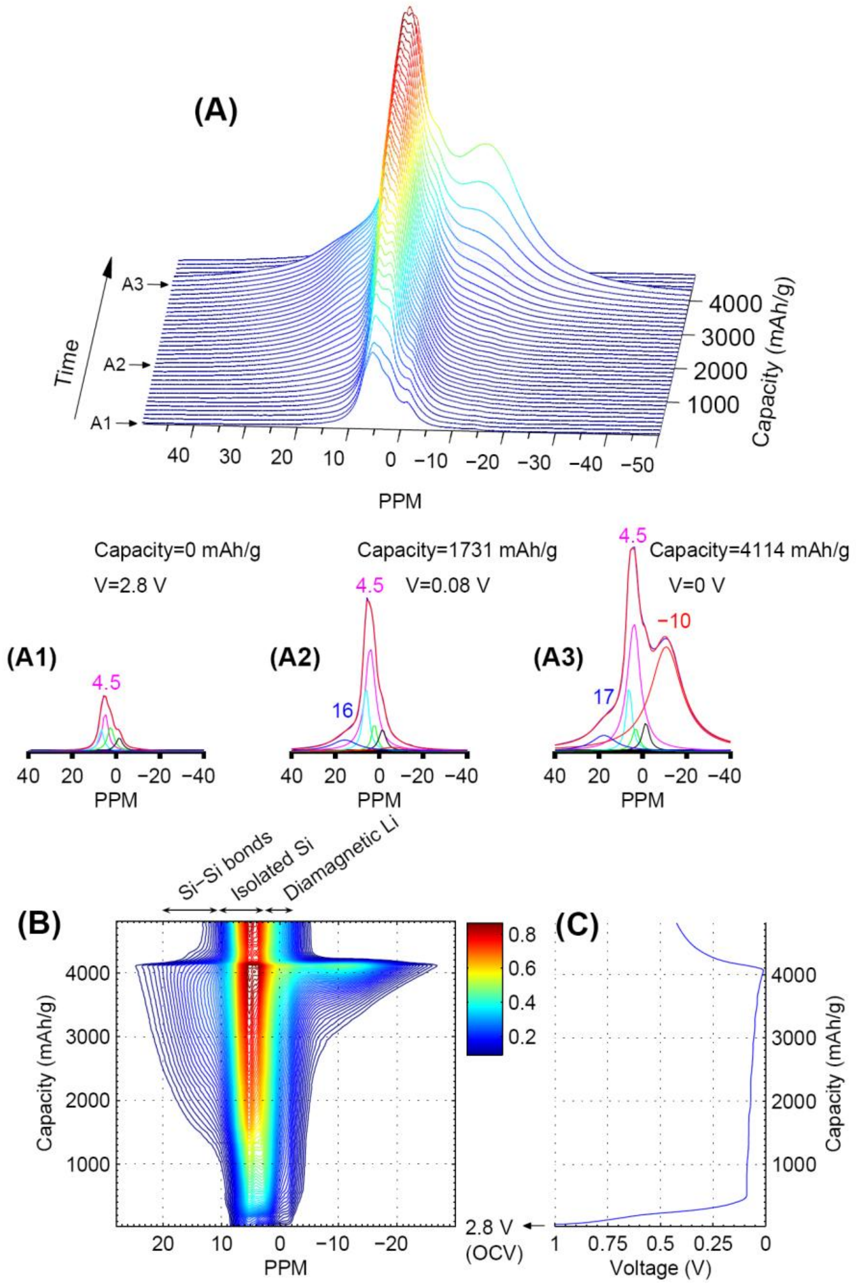

Figure 3.10. Stacked (A) and contour (B) plots of *in-situ* ^{7}Li static NMR spectra and electrochemical profile of the first discharge (C) of an actual crystalline Si vs. Li/Li$^+$ battery (the color bar shows the relative intensity scale for the spectra). A1-A3. Deconvoluted spectra at various discharge capacity values of interest.

3.3.2.4.1. Peak fitting: The *in situ* NMR data, shown in Figure 3.10 were deconvoluted and the results of the for the ~18 ppm (dark blue), ~4.5 ppm (magenta) and ~-10 ppm (red) peaks are plotted vs. capacity in Figure 3.11. A series of peaks were required to fit the complex, asymmetric lineshape of the spectral region from 0 – 8 ppm, as shown in the deconvolutions presented in the previous section, Figure 3.10 A1-A3. The lowest frequency peak (black) is due to the electrolyte. The intensities of the other three peaks (light blue, green and magenta) are not zero at capacity = 0 mAhg^{-1} confirming that they contain all contain contribution from the SEI (surface electrode interphase) on both the positive and negative electrodes. The light green peak remains constant with time and is tentatively assigned to the SEI only. The light blue peak grows slightly with time, particularly the early stages of the discharge, and clearly contains a large contribution from the Li_xC environments. The magenta peak appears to be dominated by the Li_xSi (isolated Si) environments, but does contain contributions from the SEI and possibly Li_xC environments. Therefore the evolution of the magenta peak with capacity is plotted. It is recognized that it is difficult to fit broad overlapping and asymmetric resonances and that there is no unique choice of peaks. Furthermore, the presence of weaker peaks at lower and higher frequencies of a main peak, may simply arise from broader components in the main lineshape. However, the rate of growth of the 4.5 ppm peak with discharge capacity is essentially independent of the choice of weaker peaks. Since the weaker peaks represent only a small fraction of the intensity in this spectral region, they have minimal impact on the conclusions of the paper.

The changes in the integrated peak areas and shifts of the ~4.5 and the ~18 ppm peaks during the discharge (Figure 3.11 (a) and (b)) closely follow the trend observed in the *ex-situ* NMR study discussed before. The fitting clearly shows a shift of the ~18 ppm peak to 14 ppm during the discharge. Furthermore, the drop in the intensity of the 18 ppm peak is simultaneous with the appearance of the -10 ppm peak. The maximum of the integrated peak area of the -10 ppm peak marks the end of the discharge.

The deconvolution results of the NMR spectra acquired while the battery was relaxing (Figure 3.12) show that the disappearance of the -10 ppm peak is associated with an intensity increase in both the approx. 4.5 ppm (2 ppm actual shift) and the 18 ppm peaks (12 ppm actual shift) (Figure 3.11 (c) and (d)). The decrease in intensity of the negative peak is steady with respect to time.

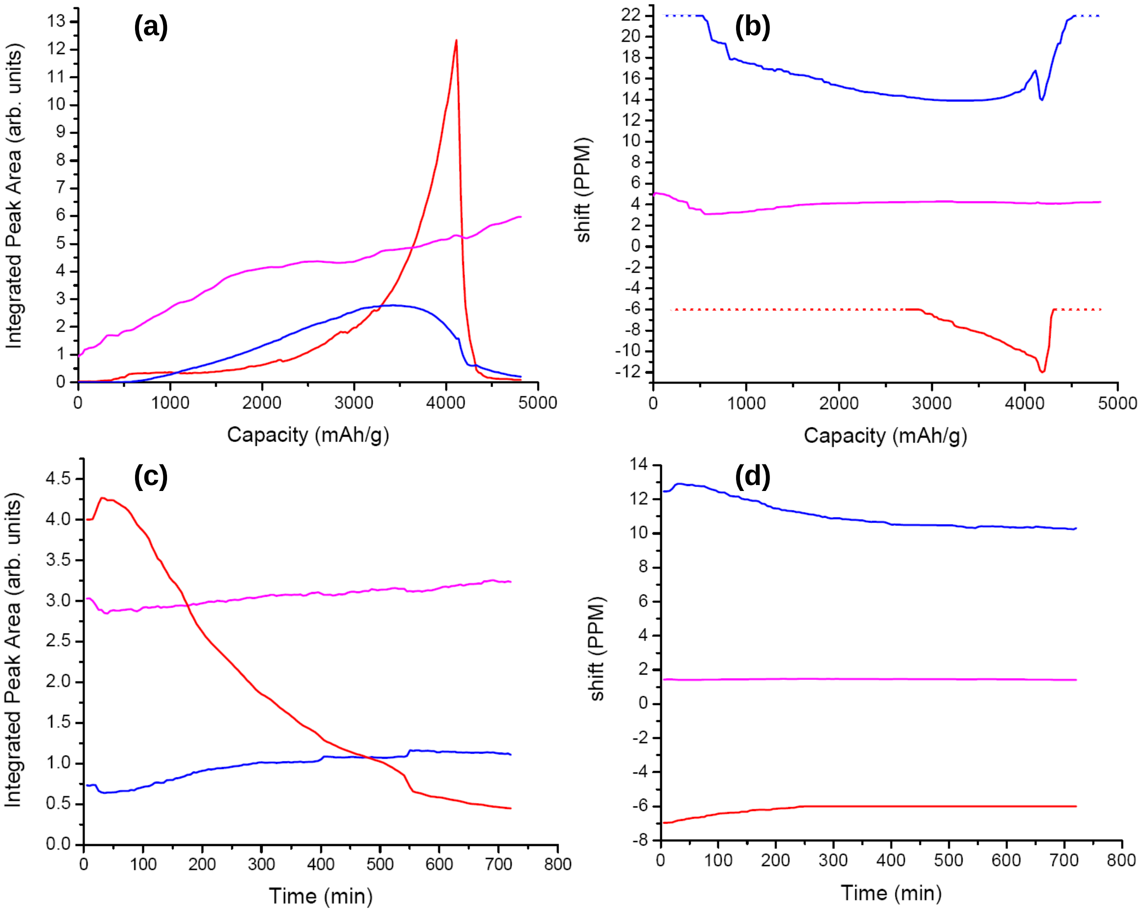

Figure 3.11. Integrated peak area (a) and peak position plots (b) of the 18 ppm (blue), 4.5 ppm (magenta) and -10 ppm (red) peaks observed in the *in-situ* discharge-charge ^{7}Li static NMR experiment *vs*. capacity. Integrated peak area (c) and peak position plots (d) of the 18 ppm (blue), 4.5 ppm (magenta) and -10 ppm (red) peaks, observed in the *in-situ* relaxation ^{7}Li static NMR experiment *vs.* time.

One major issue that must now be resolved is the apparent inconsistency between the *ex-* and *in-situ* results, at low voltages. This issue was resolved by investigating a second bag cell that had been fully discharged *ex-situ*. Upon stopping the discharge current at the bottom of the discharge (0.0 V), and monitoring the evolution of the resonances *in situ*, the environment giving rise to the -10 ppm resonance was seen to slowly disappear as the battery relaxes over a period of approximately 10 hours (Figure 3.12 (a)). This is ascribed to a reaction between the clearly very reactive, metastable, “$Li_{15}Si_4$” phase with the electrolyte, via a “self-charge” mechanism. [N.b., in a battery where silicon is the negative electrode (e.g., $LiCoO_2$ vs. Si) this will manifest itself as a self-discharge mechanism]. This signal returns on a subsequent discharge of the *same* battery.

Once this self-discharge process was identified, the short-lived, reactive phase was extracted from the coin cell battery by shorting the positive and the negative electrodes of the battery while transferring the battery into an inert atmosphere glovebox. The lithiated phase was then quickly extracted, washed and packed into rotors for *ex-situ* ^{7}Li MAS NMR analysis. Now the spectrum is dominated by a resonance at negative frequencies (-6.7 ppm), consistent with the *in-situ* NMR data (Figure 3.7, 0V washed).

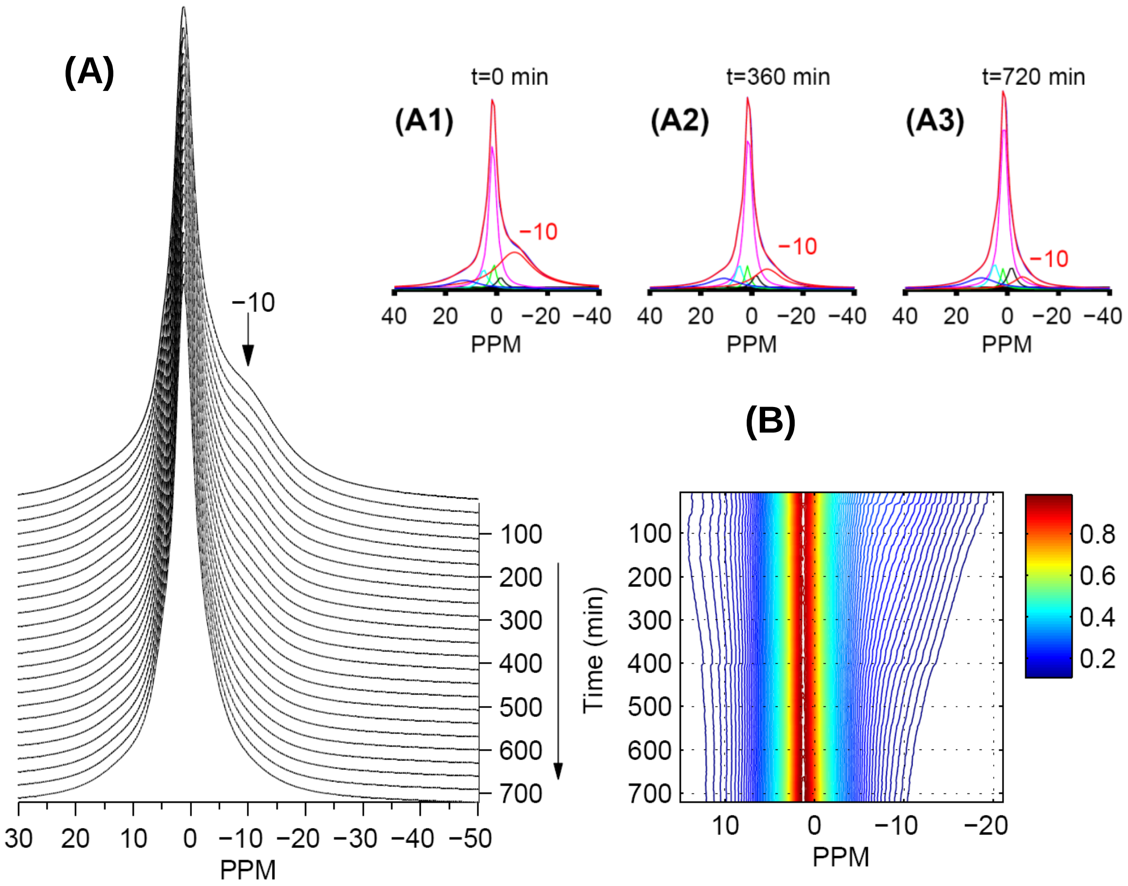

Figure 3.12. Stacked (A) and contour (B) plots of in-situ ^{7}Li static NMR spectra of the relaxation of a crystalline Si vs. Li/Li$^+$ battery stopped at the end of full discharge (0 V) (arrow shows the direction of increase in time axis during relaxation, the color bar shows the relative intensity scale for the spectra in the contour plot). Al-A3: Deconvoluted spectra at different relaxation times.

The ^{7}Li signal of $Li_{15}Si_4$ synthesized directly from the elements by ball-milling and the new phase formed electrochemically, clearly have different electronic structures, based on their very different NMR shifts. However, no obvious differences were seen in the diffraction patterns of the two compounds (data not shown), suggesting that the long-range ordering of at least the silicon is similar. Even after the self-discharge process, the "$Li_{15}Si_4$" crystalline phase is still seen in the XRD pattern (data not shown), however, the -10 ppm is no longer seen and the spectrum is similar to that observed in the *ex-situ* NMR experiment for the (unintentionally) relaxed cell (Figure 3.7, 0V). The isostructural material $Li_{15}Ge_4$ is a somewhat unusual, electron deficient phase, since it lacks one electron per formula unit ($Li^{+}{}_{15}Ge^{3.75-}{}_4$). The stability of $Li_{15}Ge_4$ was rationalized based only on relative instability of the nearby $Li_{21}Ge_5$ phase [18]. In contrast, isostructural $Li_{14}MgSi_4$ is a normal Zintl phase with the following formal charges $Li^{+}{}_{14}Mg^{2+}Si^{4-}{}_{4}$, suggesting that this structure type can accommodate excess charge. Our results suggest that "$Li_{15}Si_4$" is not a line phase but rather can accommodate some non-stoichiometry, in agreement with previous work [4,11]. The phase observed for the ball milled model compound and the one that first forms in a LIB has a stoichiometry corresponding to $Li_{15}Si_4$, or possibly $Li_{15-\delta'}Si_4$, if the initial phase is slightly Li deficient, while the phase associated with the resonance at -10 ppm is corresponding to $Li_{15+\delta}Si_4$, the range of non-stoichiometry being given by $\delta + \delta'$. This suggestion is explored below.

A number of methods were used to attempt to quantify the range of non-stoichiometry and reactivity of the metastable phase, "$Li_{15}Si_4$" formed electrochemically and by ball-milling. First, on the basis of the capacity required to remove the -10 ppm peak seen in the *in-situ* NMR experiments on charging the cell (Figure 3.10 (B) and (C)), the non-stoichiometry corresponds to approximately 0.16 Li per formula unit (per Si). A previous diffraction study has shown that the $Li_{15}Si_4$ crystalline phase is still present at this composition [19]. In a second method, a coin cell battery was discharged fully and then rested for 320 hours. The open circuit potential (OCV) is plotted vs. time in Figure 3.13. The initial rise in the OCV up to 0.12V over 10 hours is attributed to the reaction of the metastable phase, $Li_{15}Si_4$ with the electrolyte. After the rest step, the cell was discharged fully a second time, requiring an additional 100 mAh/g, corresponding to 0.11 Li per Si, i.e., $(\delta + \delta') = 0.4 – 0.6$. This excess discharge capacity is presumably required to compensate for the loss of Li from the metastable phase during the rest step. N.b., the unstable OCV even after the 320 hours rest-step suggests that the reaction may still be incomplete, consistent with the slightly lower lithium non-stoichiometry that is obtained from this method, in comparison to that estimated based on the capacity associated with the loss of the – 10 ppm resonance, as seen by *in situ* NMR spectroscopy.

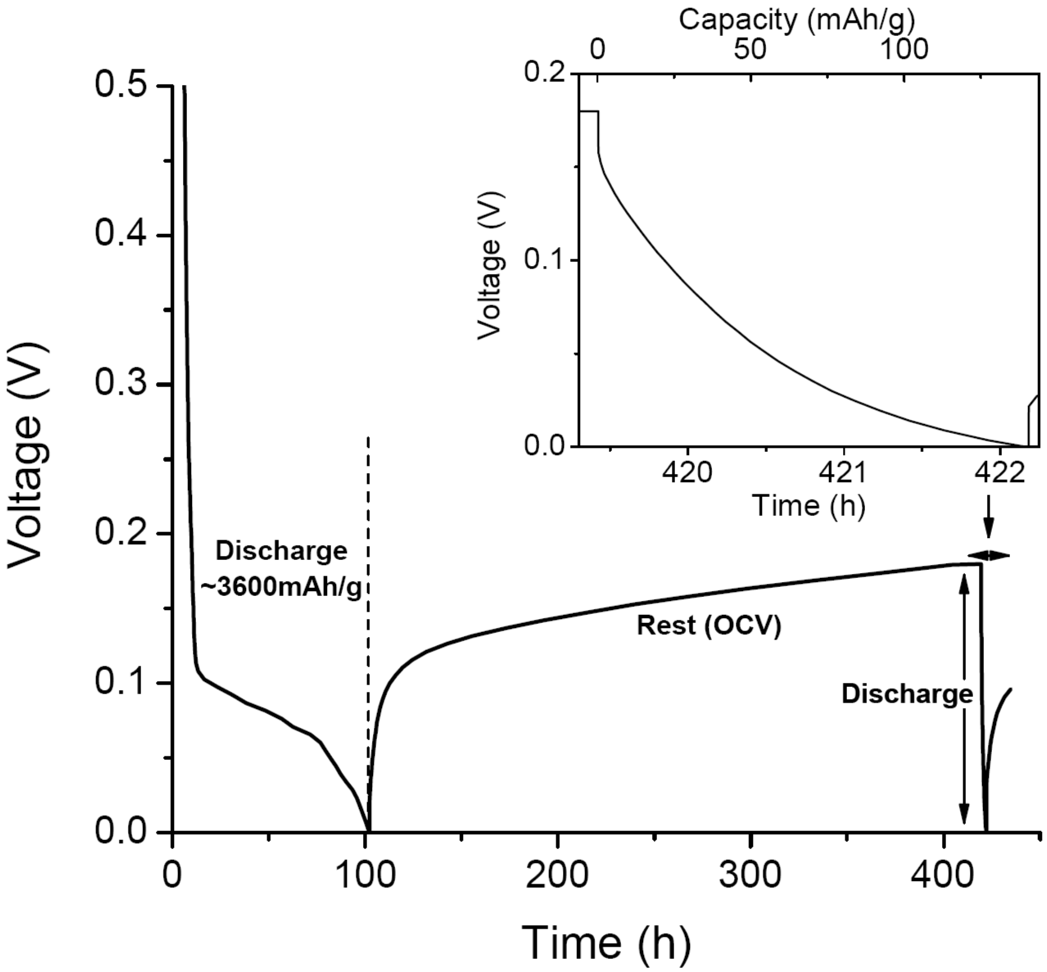

Figure 3.13. The electrochemical plot of crystalline silicon vs. Li^+/Li. The open circuit potential is plotted during the rest period (after the 1st discharge). Inset: Magnified plot of the second discharge after the rest step.

^{7}Li MAS NMR spectra of the model compound $Li_{15}Si_4$, synthesized by ball-milling, and of that made into an electrode and electrochemically discharged to a potential of 0 V and washed, are shown in Figure 3.14. The ^{7}Li NMR shift of the discharged sample is clearly more shielded than that of pristine $Li_{15}Si_4$, consistent with additional lithium insertion in this phase, providing additional evidence that $Li_{15}Si_4$ is not a line phase and can accommodate a slight excess of lithium. However, the resonance does not shift to as low a frequency as observed following electrochemical lithation of Si (Figure 3.7, -6.7 ppm). This may be due to the variations in the ability of the two $Li_{15}Si_4$

materials, one synthesized by ball-milling and the other electrochemically, to accommodate additional Li, due to differences in particle sizes and/or defect concentrations. Alternatively, some partial self-discharge of the over-lithiated $Li_{15}Si_4$ (ball-milled) phase could have occurred before the cell was taken apart. Consistent with this, a shoulder at 15 ppm in the spectrum of the discharged material is seen, suggesting the formation of Si-Si small clusters formed via a self-discharge process. This further suggests that $Li_{15}Si_4$ can react with the electrolyte, to form an amorphous lithium silicide phase.

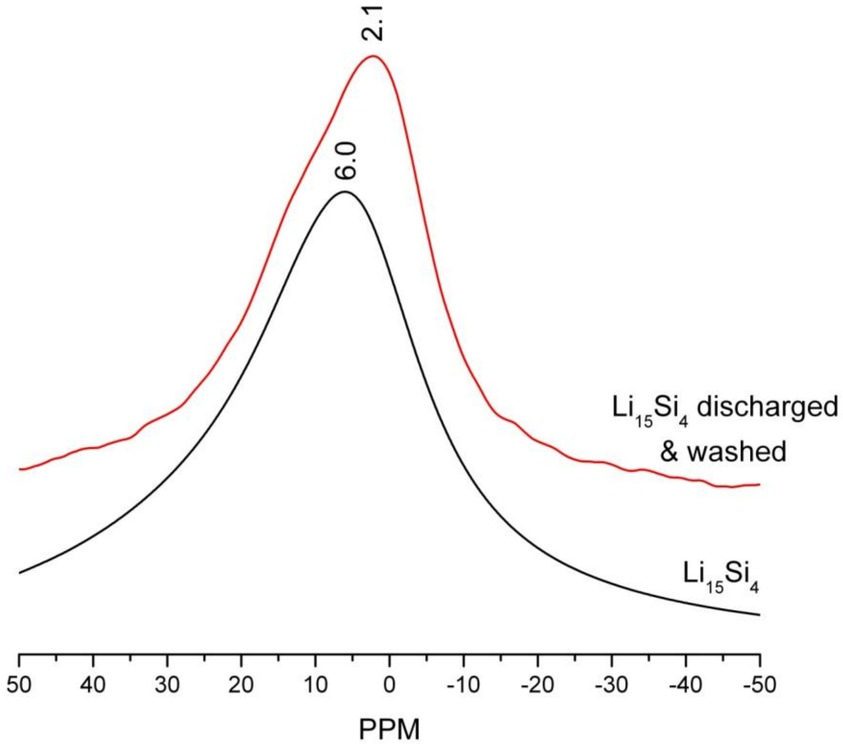

Figure 3.14. ^{7}Li MAS NMR spectra collected at 38 kHz spinning speed of pristine $Li_{15}Si_4$ and a $Li_{15}Si_4$ sample fully discharged and then washed.

Finally, the effect of a binder on the low voltage process was investigated. Figure 3.15 shows the comparison between the OCV of cells constructed with and without the use of CMC binder [20] that have been left to relax following the 1st full discharge process. The electrochemical profile of the CMC cell shows that the cell still relaxes but the initial rise in the OCV is smaller. The CMC cell reaches only 75 mV after 9 days whereas the OCV of the cell with no binder rises much more rapidly, reaching 170 mV. In contrast a CMC cell took almost a month (29 days) until it reached 170 mV. Although the initial rise in OCV for the CMC cells varies slightly between cells, the two electrochemical profiles shown in Figure 10 represent the lower and upper limits of the OCVs observed in several CMC cells. The initial rise in the potential profile always remained below 100 mV for CMC cells and above 100 mV for cells with no binder. Figure 3.15 (b) shows that the *ex-situ* NMR spectra acquired for the fully discharged CMC cell contains the approximately -5 ppm resonance, but that the 9 day relaxed CMC cell still has a resonance at -3.4 ppm suggesting the relaxation is not complete. The relaxation of the CMC cell that was allowed to rest for a month is close to completion, and the negative ppm resonances are replaced by a resonance at 6 ppm. In contrast to binders such as PVDF, CMC had been suggested to bond to the thin layer of SiO_2 on the Si particles, which results in better accommodation of the expansion/shrinkage upon cycling Si [20]. Such a coating also appears to inhibit the reaction of the highly reactive $Li_{15+\delta}Si_4$ with the electrolyte.

Analysis of the *in-situ* NMR experiments suggests that the side reactions also occur between the lithium silicides and the electrolyte at higher voltages. The effect of these reactions is, however, much easier to monitor at very low voltages, because it results in significant changes in both the NMR spectrum and the OCV. However, the intensity of the 4.5 ppm ^{7}Li resonance, which is assigned to both Li in the SEI and nearby isolated Si atoms, continues to grow steadily with time, even during the initial stages of the discharge and on charge (where Li should be removed from the lithiated silicide, reducing the intensity of this resonance). This confirms that some of this signal is due to products arising from electrolyte decomposition, and indicates that the amorphous lithium silicides are also reactive. Additional *in-situ* experiments (not shown) showed that the 4.5 ppm peak did not gain in intensity when the battery was discharged to only 100mV and left for a day. More detailed NMR experiments are in progress to attempt to separate some of the overlapping signals from the different components in the static spectra of the intact batteries and to investigate the decomposition reactions in greater detail. Finally, our batteries used for the *in-situ* NMR studies were only associated with capacities for the first charge of approx. 1500 $mAhg^{-1}$, the capacity dying rapidly on subsequent cycles. This capacity fade may be inherent to the binder choice used in the *in-situ* NMR cell, and the likely related reactions with the electrolyte. Attempts to optimize the design to allow studies of multiple discharge-charge cycles are in progress.

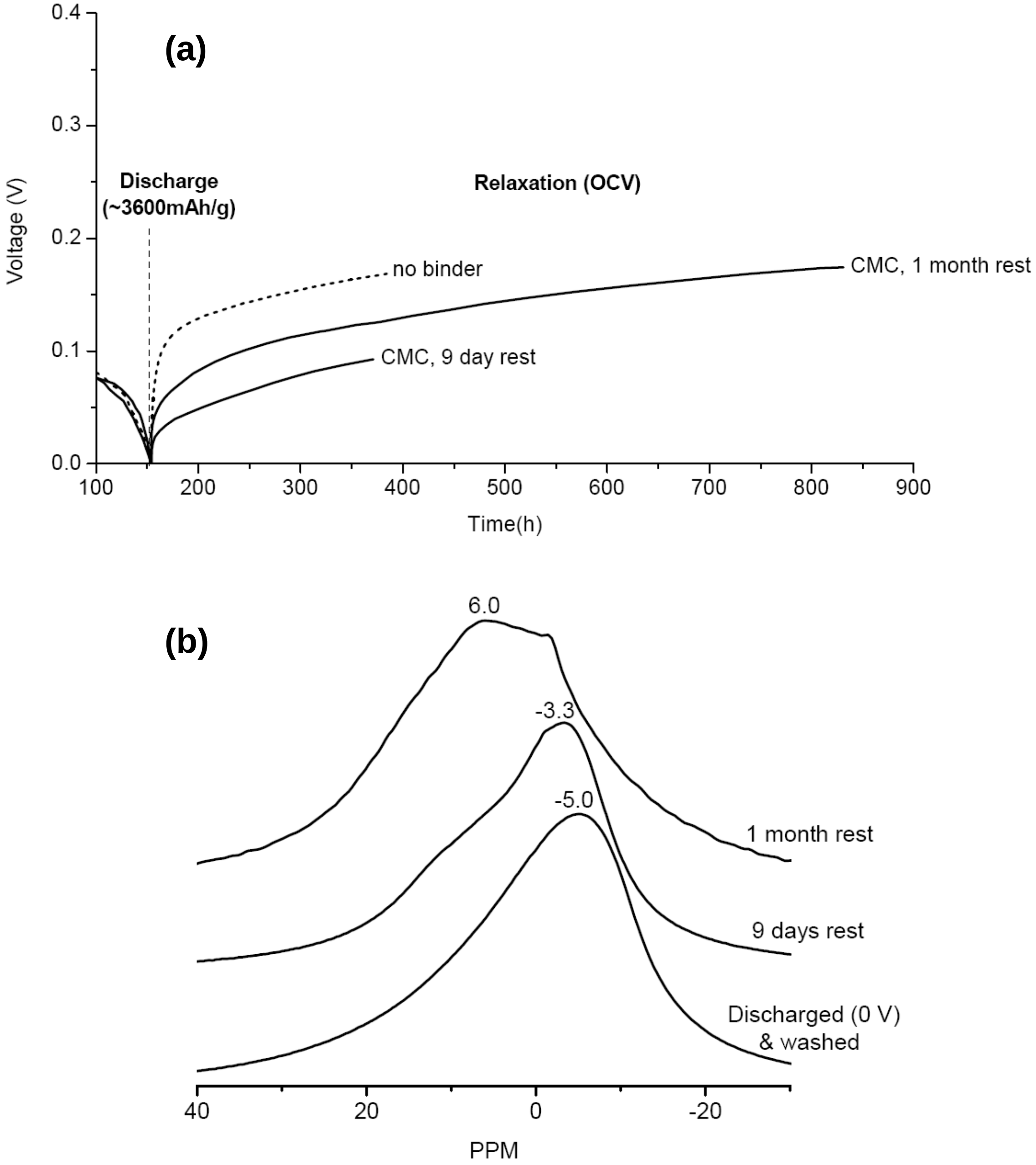

Figure 3.15. (a) Electrochemical profiles of the first discharge, followed by 9 day and 1 month relaxation of crystalline silicon vs. Li/Li$^+$ cells prepared with (solid lines) and without CMC binder (dashed line, 9 day relaxation). The first 100 hours of the discharge are not shown. (b) *Ex-situ* ^{7}Li NMR spectra of battery samples stopped at the end of the 1st discharge (0V), after 9 days and 1 month relaxation of crystalline Si vs. Li/Li$^+$, prepared with a CMC binder.

3.3.2.5. *ex situ* ^{29}Si MAS NMR of the Discharged Samples

In order to probe the changes in electronic structure, as monitored at the Si sites, *ex-situ* ^{29}Si NMR experiments are presented (Figure 3.16) for two of the samples whose ^{7}Li spectra were shown in Figure 3.7. They clearly show a change in the silicon local structure on lithiation, as most of the intensity at -80 ppm from crystalline silicon is converted to broad resonances at 72 and 235 ppm, for the cell assembled at the end of the discharge step, without washing. However, if the electrode (of the discharged cell) is quickly washed and packed into the rotors for data acquisition, a significant shift of the Si resonance is seen and a new, broad peak centered at 942 ppm is observed. Very little signal is present between 72 and 235 ppm. This again confirms that the electronic structure surrounding the Si in the $Li_{15+\delta}Si_4$ is very sensitive to whether the sample is allowed to rest before disassembling the cell, consistent with the ^{7}Li NMR results. Finally, space-charge mechanisms have been used to explain additional capacity in some nano-composites [21]. These results do not appear to be consistent with this mechanism, since essentially all of the ^{29}Si signal is shifted, and not just the signals from Si atoms near the surface of the particles.

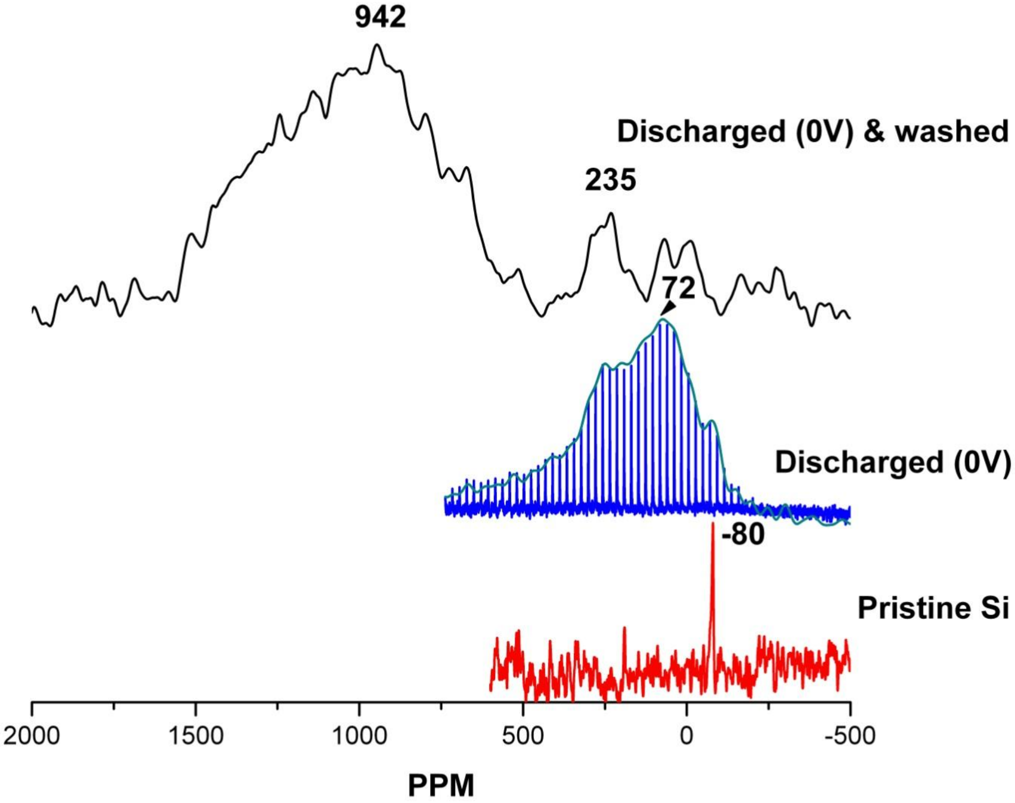

Figure 3.16. The ^{29}Si MAS NMR spectra of crystalline silicon, fully discharged crystalline silicon and a fully discharged and immediately washed sample. Spectra were collected at a 14 kHz spinning speed and a CPMG sequence was used for the fully discharged sample (unwashed).

3.3.2.6. *ex situ* ^{7}Li MAS NMR (1st Charge)

The NMR spectra of samples collected along the pseudo plateau show a clear trend, a loss in the intensity of the NMR peaks being seen as the charging proceeds (Figure 3.17). Up to a state of charge of 440 mV, which corresponds to the middle point on the charge, both the major resonance at 5.3 ppm due to Li in isolated Si clusters[6] and the minor resonance at 16.5 ppm due to Li in Si-Si clusters[6] lose intensity. Importantly, the spectrum of the sample from a battery stopped at 458 mV does not contain a resonance at 16.5 ppm, due to Li nearby Si clusters, while the resonance at 5.3 ppm is still present. I.e., there is no evidence for the formation of intermediate phases or domains containing silicon clusters. Beyond this point to the top of the charge at 3.0 V, the resonance gradually shifts to 3 - 2 ppm. The 2 ppm resonance is tentatively ascribed to either some residual Li trapped in a lithiated silicide, in a “dead”, i.e., non electrically-connected particle, or possibly some Li_2O due to the passivating layer of oxide on the surface of the starting material (the ^{7}Li chemical shift of Li_2O is 2.7 ppm[22]). An alternative and more likely explanation is that this resonance is due to Li particles nearby large silicon domains.

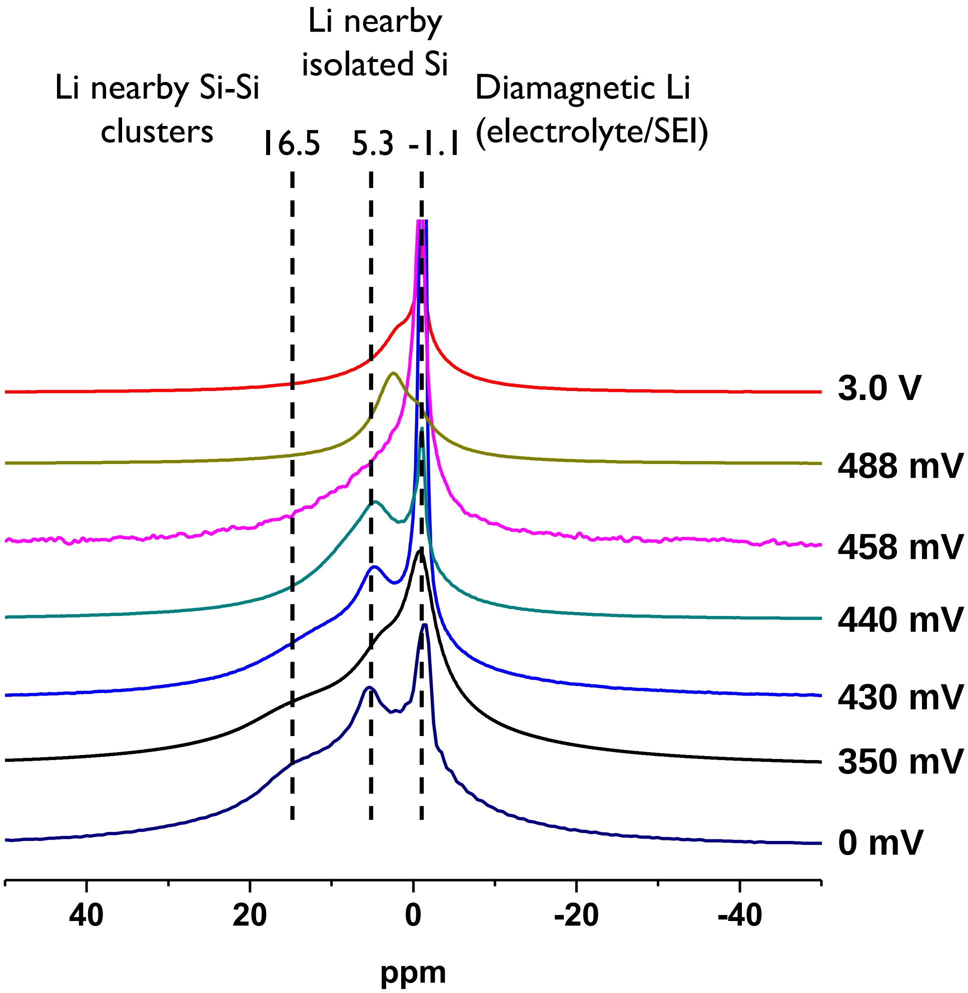

Figure 3.17. *ex situ* ^{7}Li MAS NMR of battery samples stopped during the 1st charge. Dashed lines indicate resonances with known lithium assignments.

3.3.2.7. PDF (1st Charge)

The PDF data (Figure 3.18) is largely consistent with the NMR data: the 4.75 Å correlation due to long range Si - Si ordering of isolated Si anions disappears at 440 mV (approximately the mid-point of the plateau-like region), the intensity of the first two Si correlations growing steadily with state of charge. The ratios of the intensities of these two correlations remains approximately constant with the state of charge, this observation implying that no intermediates a higher intensity ratio for the 2.35 : 3.8 Å correlation, which would be characteristic of a cluster phase, are seen. A shoulder on the Si-Si peak is seen at 2.5 Å (marked with an arrow for the sample collected at 458 mV), Interestingly, the crystalline LiSi phase, which contains a 3 dimensional three coordinated Si network (analogous to black phosphorus) also contains longer Si-Si distances of 2.4 – 2.5 Å, suggesting that this correlation may be seen for similar Si local arrangements [23].

The delithiated phase is amorphous and has only very weak peaks beyond 4 Å. The dominant peaks at 2.35 and 3.8 Å correspond to distances in a silicon tetrahedron. None of the smaller weaker peaks above 3.8 Å corresponds to those found in crystalline Si and the complete absence of the 4.5 Å peak indicates that the ordering of the Si tetrahedra that is present in crystalline silicon is completely absent. No nanocrystalline Si domains, which would be difficult to detect by diffraction, are formed. The difference in the 2.35 : 3.8 Å intensity ratio between crystalline silicon and delithiated amorphous silicon, indicates that the tetrahedra themselves are more distorted, and that some 3 coordinate Si could also be present. The weaker peaks such as the one at 4.2 Å may correspond to Si-Si 2nd coordination distances in 3 coordinate Si units or in larger Si-Si rings, an increase in the Si-Si-Si bond angle leading to longer correlations.

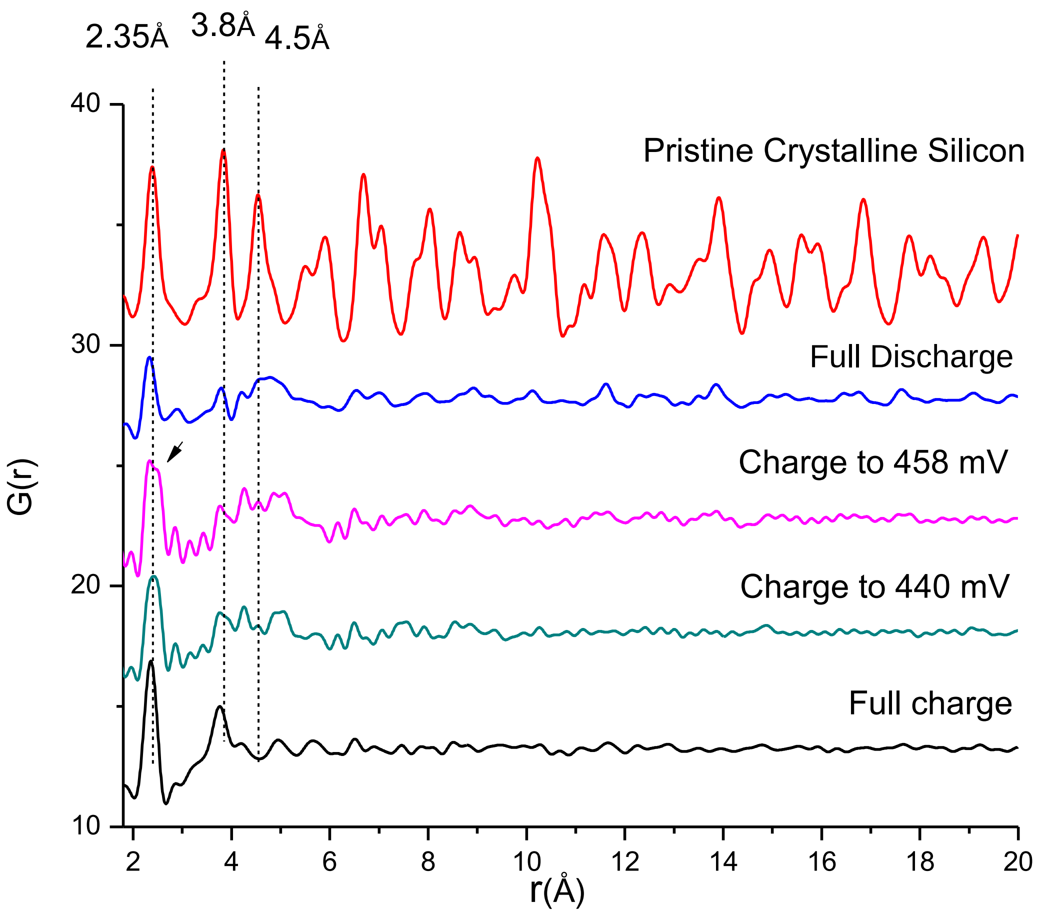

Figure 3.18. Short to mid range *ex situ* PDF of crystalline silicon, fully discharged, charged to 440 mV, 458 mV and fully charged battery samples extracted from the 1^{st} cycle of a crystalline silicon electrode. The dashed lines indicate 1^{st}, 2^{nd} and 3^{rd} coordination shells of Si—Si distances in Si diamond matrix. The arrow indicates the correlation at 2.5 Å.

3.3.2.8. *ex situ* ^{7}Li MAS NMR (2^{nd} Discharge)

The lithiation of the amorphous Si, formed after the 1^{st} charge, is now monitored by using both NMR and PDF, to investigate the structural origins of the two distinct voltage regions in the 2^{nd} discharge profile of silicon (Figure 3.4) at approximately 250 and 100 mV. Since subsequent discharge cycles appear to go through the same electrochemical processes[1], it is particularly important to understand these processes. Figure 3.19 shows the ^{7}Li NMR spectra of samples extracted following discharge after charging to 3.0 V. The 1^{st} process, which starts at 300 mV and ends at approximately 150 mV, is accompanied by the appearance of a broad NMR resonance centered at around 3 ppm (see for example, the 260 mV sample). The NMR spectrum of the 200 mV sample is also dominated by the 3 ppm signal, but the presence of a tail at higher frequencies (centered around 12 ppm) indicates a minor presence of Li environments nearby Si clusters. The 3 ppm resonance is surprising, because based on our earlier assignments it should indicate isolated Si ions. However, a 2 - 3 ppm resonance is also formed at the end of the 1st charge, where it is suggested that it may be due to Li nearby much larger Si clusters. The observation of presumably the same resonance on both charge and discharge strongly suggests that this 3 ppm resonance is indeed due to Si nearby larger Si clusters, where little electron density transfer between the Si clusters and Li ions has occured, i.e., the Li^+ ions are still in a diamagnetic environment. Again, this hypothesis requires testing.

Beyond 150 mV, the peak intensities change in a manner that is similar to that observed during the 1st discharge. After 200 mV, the resonance due to Li nearby small Si-Si clusters at 16.9 ppm starts to gain in intensity until the end of the 2nd plateau-like region at 70 mV. Beyond this point this resonance disappears, and at 0 mV, the 5 ppm resonance due to Li in isolated silicon ions dominates. The presence of an over-lithiated $Li_{15+\delta}Si_4$ phase was detected in every subsequent discharge cycle after the 1st discharge [6] (see the *in situ* NMR experiment that illustrates this, Figures 3.20 and 3.21).

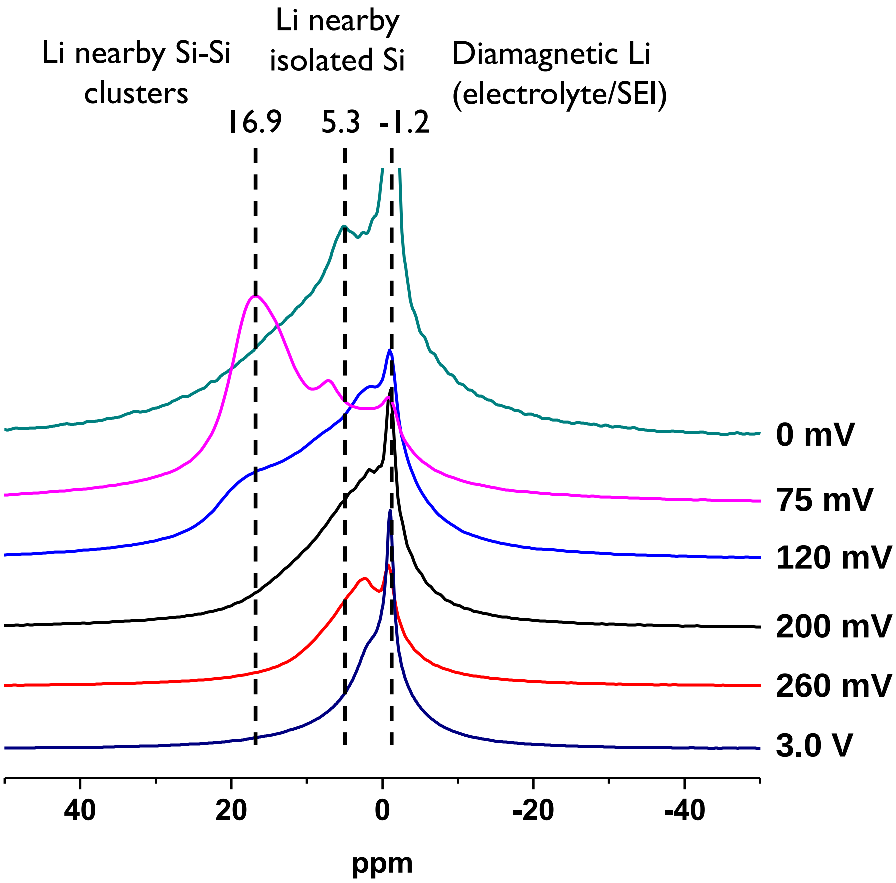

Figure 3.19. *ex situ* ^{7}Li MAS NMR spectra of battery samples stopped during 2nd discharge. Dashed lines indicate resonances with known lithium assignments

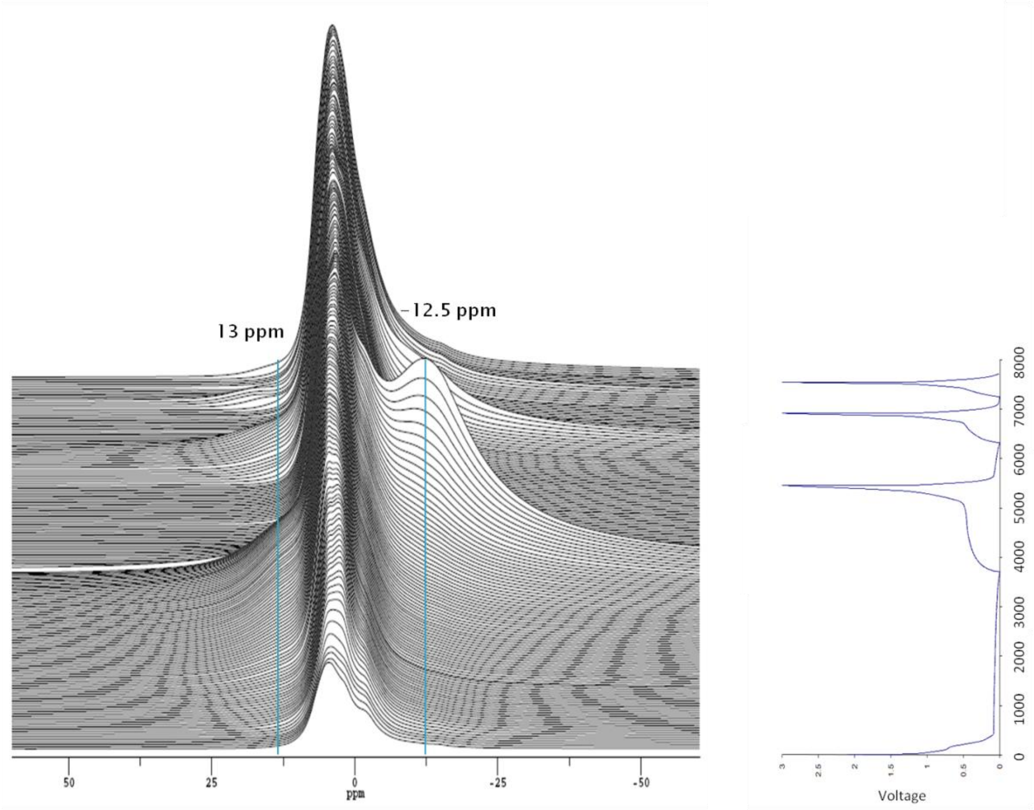

Figure 3.20. Stack plot and electrochemical profile of an in-situ NMR experiment for the first three cycles for crystalline silicon electrode vs. Li metal.

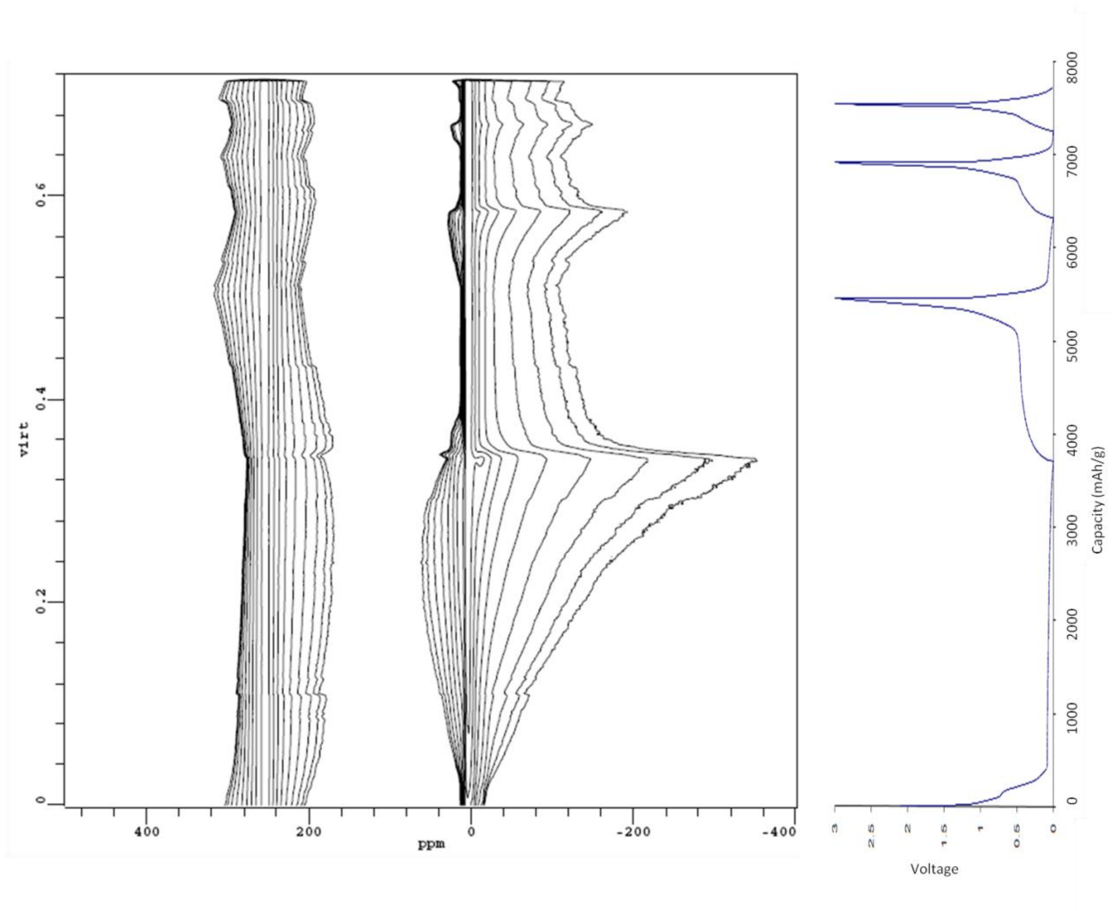

Figure 3.21. Contour plot and electrochemical profile of an in-situ NMR experiment for the first three cycles for crystalline silicon electrode vs. Li metal.

3.3.2.9. PDF (1st Charge)

The short-range correlations in the PDF patterns (from 2-6 Å) and the integrated areas under the peaks for samples stopped during the 2nd discharge are shown in Figure 3.22. The decrease in intensity of the 3.8 Å peak and the 2.35 Å peak does not follow the same trend as observed for the 1st discharge. The intensity of the 3.8 Å peak has diminished almost completely at the end of the first discharge plateau-like region, i.e., in for the sample collected at 120 mV. However, the 2.35 Å peak is still present in the PDF pattern of this sample, indicating a complete loss of larger Si-Si-Si units, but the presence of residual Si-Si bonds in the structure. The peak at approximately 4.2 Å grows in this range, which is ascribed to the formation of Si "stars" (Figure 3.1 (b)) or possibly Si-Si-Si trimers. Beyond this point, and along the lower voltage process at approx. 100 mV, the 1st coordination (Si-Si bond) peak continues to lose intensity. The PDF pattern of the 74 mV sample contains a new peak at approximately 2.5 Å, which is assigned to 1st shell Li-Si correlations. These correlations are clearly seen in the PDF patterns of the model compounds $Li_{12}Si_7$, Li_7Si_3 and $Li_{13}Si_4$ (see Chapter 2). At the same time, the "2.35 Å" peak shifts to lower values (approximately 2.30 Å), which is ascribed to the formation of more multiply-bonded Si-Si linkages. The integrated "2.35 Å" peak intensity is strongly affected by the contribution from the 2.5 Å peak (Figure 3.22), which is ascribed to Li-Si correlations. Thus, the lineshape was deconvoluted with two peaks (2.30 Å and 2.5 Å) for the 75 and 0 mV samples and only the 2.30 Å deconvoluted integrated intensities are plotted. In summary, the plot of the Si-Si correlation intensities shows a decrease and almost complete loss of intensity of the 3.8 Å peak during the 1st higher voltage process, the 2.35 Å peak losing intensity during both processes, but most noticeably during the lower voltage process, some intensity remaining at the end of full discharge. At 0 mV, the characteristic distance at 4.7 Å due to the crystallization of the $Li_{15+\delta}Si_4$ can be observed.

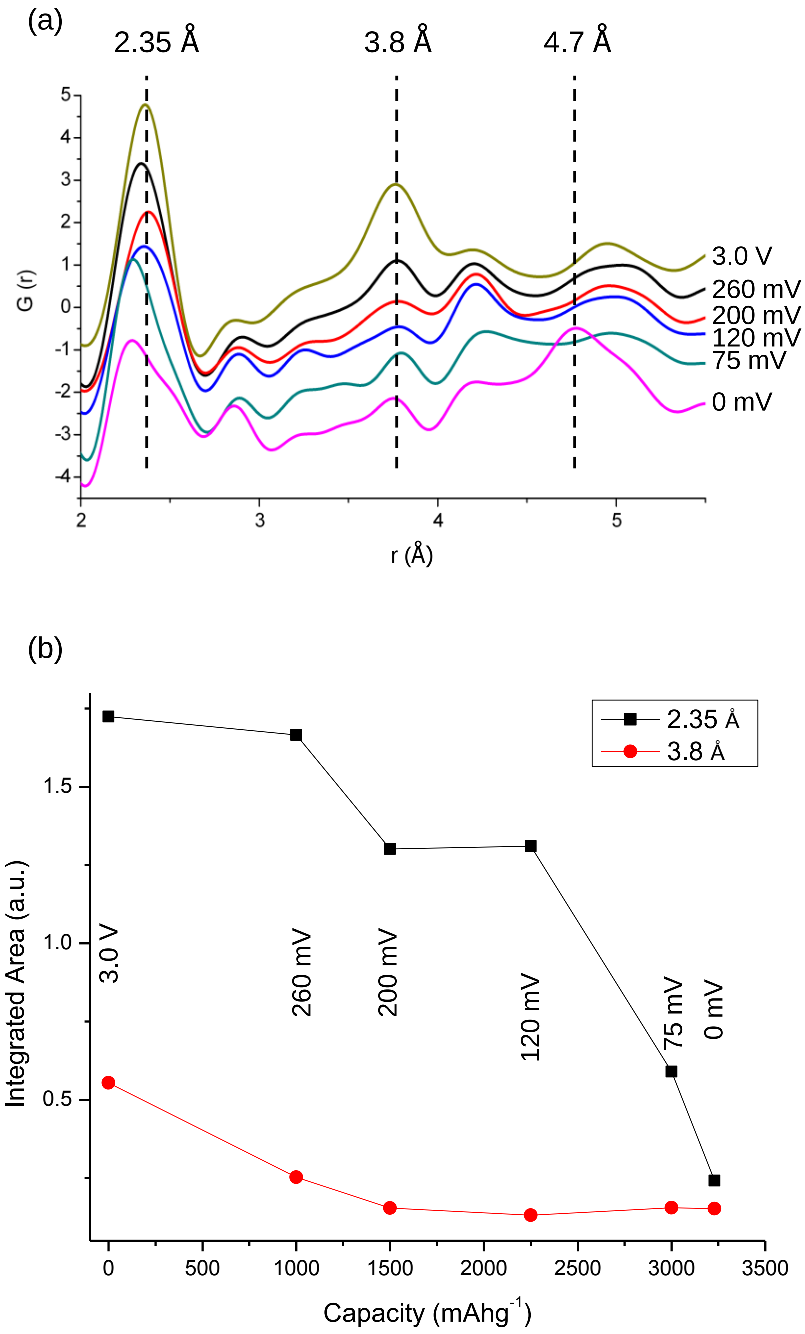

Figure 3.22. (a) *ex situ* Pair Distribution Function G(r), and (b) integrated area under the 1st two PDF correlations peaks, for battery samples stopped during the 2nd discharge. The first two dashed lines indicate the 1st and 2nd coordination shells of Si—Si distances in a Si diamond matrix, while the 3rd (4.7 Å) corresponds to the $Li_{15}Si_4$ characteristic Si-Si distance.

3.3.2.10. *ex situ* ^{7}Li MAS NMR (Charge subsequent to a Partial Discharge)

In order to investigate the correlation between structure and the two unexplained processes following a partial discharge[1], a series of NMR spectra of samples were collected following discharge to a cutoff of 85 mV (Figure 3.4b) and subsequent charging. 85 mV is selected because it corresponds to a point near total amorphization of the crystalline silicon matrix. The studies described above indicate that at this state of discharge, there are two main lithium local environments, lithium ions surrounding isolated Si ions (weaker resonance at approx. 8 ppm), and lithium ions close to Si-Si small clusters (14 ppm). Delithiation of this 85 mV phase to 250 mV is predominantly associated with a small shift of the 14 ppm (cluster) ^{7}Li resonance to high frequency (16.5 ppm) and a loss of intensity of both cluster and isolated Si Li resonances. Both observations suggest that larger clusters are formed at the expense of some of the isolated anions. The cluster resonance then decreases in intensity and, from 330 to 425 mV, shifts to noticeably lower frequencies, reaching 10 ppm at the end of the low voltage process (see Figure 3.23, samples 85 to sample 425 mV). At this point, Li environments nearby both clusters and isolated Si ions now predominate. Beyond this point, the 10 ppm resonance completely disappears, and a shift at 3 ppm is observed.

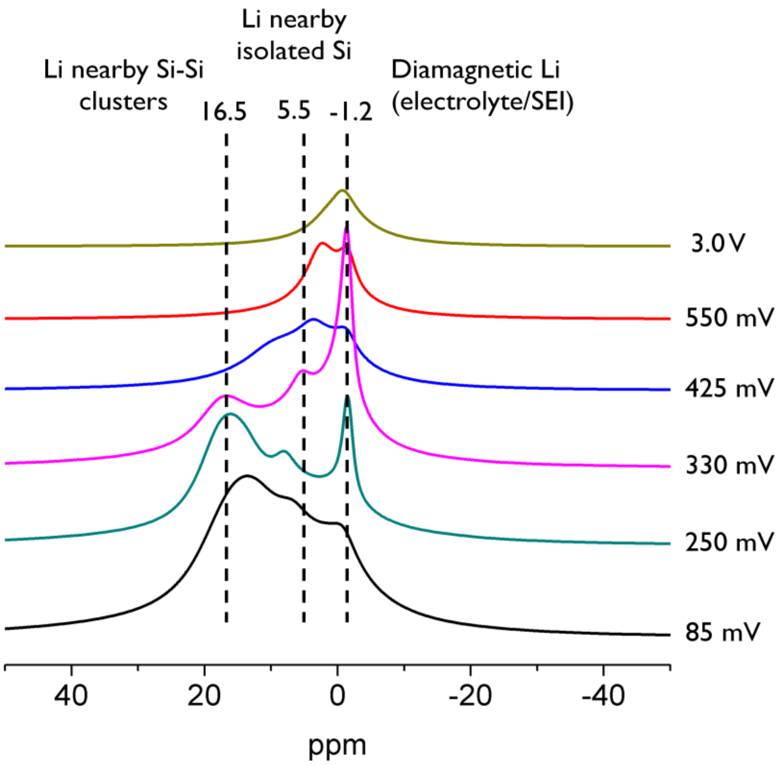

Figure 3.23. *ex situ* ^{7}Li MAS NMR spectra of battery samples stopped during the 1st charge subsequent to a partial discharge to 85 mV.

3.3.3. Discussion of the lithiation mechanisms

3.3.3.1. 1st Discharge

In general, lithiation is expected to start on, or close to the surface of a Si particle, where the Li in electrolyte has access to the particle through the SEI. The significant volume expansion associated with lithiation of Si also favors a reaction front that starts from the surface. A recent theoretical (DFT) study of lithium transport in crystalline silicon thin films found a large activation energy for lithium transport from the (100) surface into the bulk (0.88 eV), with lower activation energies for transport between subsurface sites (0.5 eV) and within the bulk (0.57 eV) [24]. The larger activation energy largely resulted from the presence of a stable (low energy) site for Li on the silicon surface, these DFT studies again suggesting that the reaction starts by lithiating the surface. Presumably, the initial Li ions enter the Si framework from the surface sites forming interstitial sites. The presence of Li, and the associated addition of electron density to the silicon framework, will weaken the Si network surrounding Li, eventually resulting in Si – Si bond breakage and the formation of small Si (negatively charged) clusters surrounded by Li ions (Figure 3.24, II). Given (a) the large activation energy associated with Si – Si bond breakage, particularly for crystalline Si, and (b) the volume expansion associated with Li insertion, once Si-Si bond breakage has started, it will be (kinetically) easier to continue to break up these Si clusters, rather than to continue to lithiate and break up more of the Si framework. There will be a competition between the two processes (i.e., reaction with the framework, vs. the clusters), both factors (i.e., the kinetics and the volume expansion) preventing the system from reaching thermodynamic equilibrium even if the potential is removed and the system is allowed to relax. Our results suggest that the intermediate phases such as Li_7Si_3 (containing dumb-bells only) do not crystallize at this stage, because no single type of silicon cluster is present in the amorphous region. Crystallization to form one particular crystalline cluster phase would require Si – Si bond breakage and rearrangements (Si migration), which involves too large an activation barrier. The inhomogeneity of Li content likely occurs at both a local and electrode level, the poor electronic conductivity of silicon likely contributing the latter inhomogeneity.

Such a scenario agrees with our PDF data, which shows a larger drop in intensity of the 2nd and 3rd Si-Si correlations over that expected in a reaction to directly form $Li_{15}Si_4$, indicating that clusters must be present. 2.35 Å correlations are present throughout confirming that small clusters are present; their intensity at 85 mV (and the intensity of the 3.8 Å peak) is greater than predicted for a model where only dumb-bells are present, showing that isolated Si ions must also be present, consistent with the NMR data at this stage. A comparison between the Li NMR data of Li_xSi and the model compounds again suggests that the Si clusters are relatively small, likely comprising dumb-bells, stars and possibly trimers/small rings.

The lithiation continues until all the silicon atoms of the diamond matrix are consumed via bond breakage, as seen by PDF at beyond 85 mV (Figure 3.24, III, $Li_{2.33}Si$). At this point, a gradual shift of the NMR peaks to lower frequency, corresponding to the breakage of the small Si clusters, is seen predominantly resulting in the formation of isolated silicon ions. A crystalline phase $Li_{15+\delta}Si_4$ can now (i.e., below 50 mV) nucleate from an amorphous $Li_{x'}Si$ phase, because the amorphous phase largely contains isolated Si anions and only a few Si clusters (Figure 3.24, IV). It is speculated that one reason that the metastable $Li_{15}Si_4$ phase crystallizes rather than the thermodynamic phase $Li_{21}Si_5$, is because this phase can accommodate defects, such as Si-Si dumbbells, more readily than can $Li_{21}Si_5$.

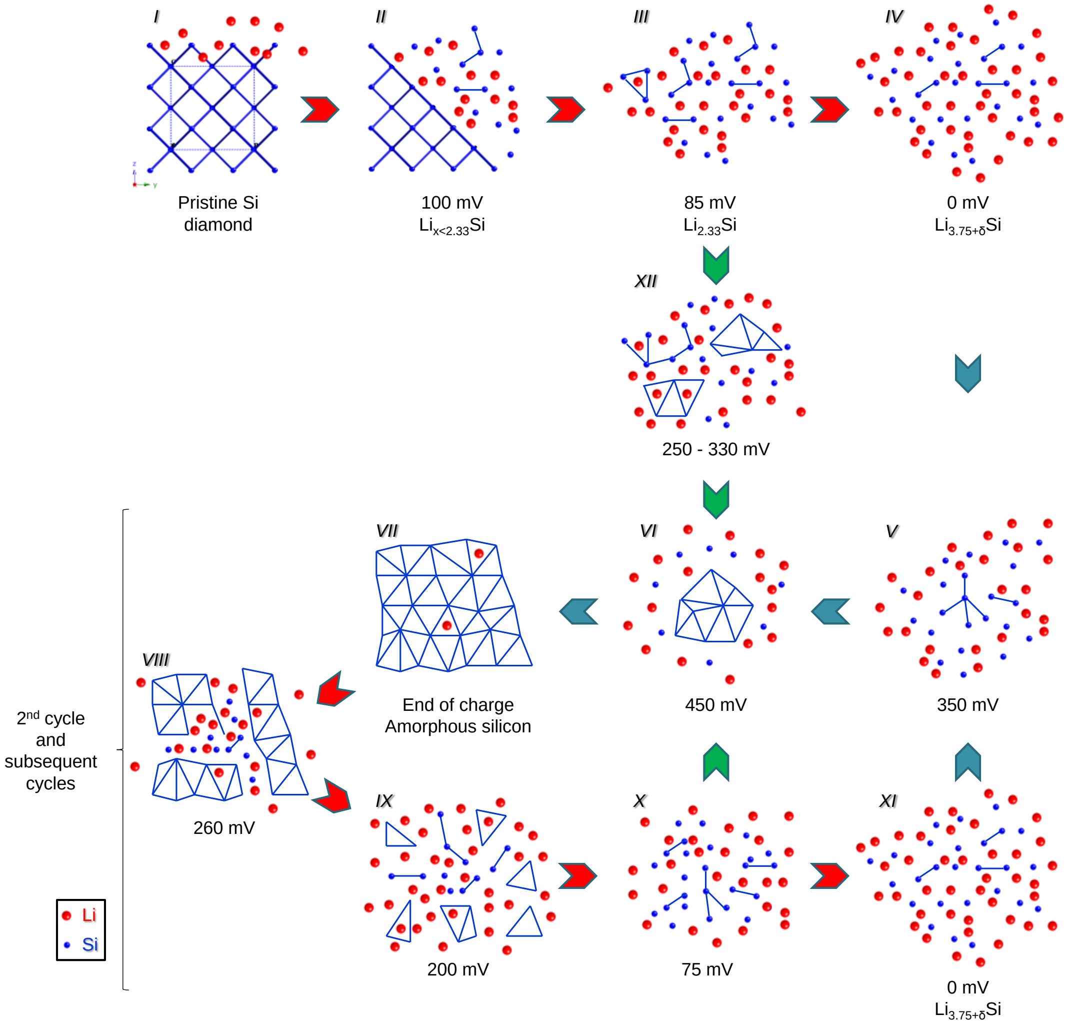

Figure 3.24. Illustration of mechanisms by which silicon is lithiated and delithiated. I to IV corresponds to lithiation of crystalline silicon discharged down to 0 mV. Red arrows denote discharge steps, while blue and green arrows denote charge steps. V to VII corresponds to delithiation of fully lithiated silicon and VII to XI corresponds to relithiation of amorphous silicon to form fully lithiated silicon for cycle #*x* (*x*>1).

3.3.3.2. 1st Charge

The delithiation mechanism is shown in Figure 3.24 from IV to VII. Contrary to the lithiation of crystalline silicon, delithiation from $Li_{15}Si_4$ may, in principle, proceed from both the surface and from the bulk owing to the high lithium diffusivity in the lithiated phases. Evidence for rapid Li motion in the Li_xSi phases comes from the sharp ^{7}Li NMR resonances that were observed in the static NMR spectra for the amorphous and crystalline lithiated phases[6] and for the lack of clear resolution of the signals from the different crystallographic sites in the ^{7}Li MAS NMR of the model compounds, even at spinning speeds of 38 kHz. Delithiation of $Li_{15}Si_4$ should lead to the formation of Si clusters if delithiation follows the thermodynamic pathway, and yet these are not seen in significant concentrations in the Li NMR spectra (Figure 3.17). Thus, it appears that once a nucleation site, in the form of a small cluster is formed, this starts to grow to form an amorphous silicon matrix. Growth is helped by the rapid diffusion of Li^+ in the Li_xSi phase, away from the growing Si cluster/amorphous Si domain. Growth of an already formed cluster (or a defect that remains at the end of the 1st discharge) is more likely to dominate over nucleation to form a new cluster, because the latter requires two highly charged silicon anions (with formal charge of 4-) in the $Li_{15}Si_4$ to migrate closer together and to combine. In contrast, addition of a Si anion to a growing Si nucleus (Si cluster) that has already formed, which will have a lower formal charge (per Si atom), should proceed more readily (Figure 3.24, V to VI). Thus the lithiated phase with isolated Si ions is gradually converted to an amorphous Si phase. A few Li ions remain, as seen by the resonance at 3 ppm, but these are ascribed to Li on the surfaces of larger amorphous Si domains or coordinated to much larger Si clusters.

3.3.3.3. 2nd Discharge

The 2nd discharge of the amorphous Si, based on the combined PDF and NMR studies, (Figure 3.24, from VII to X) progresses by breaking down the amorphous silicon matrix to form silicon clusters. The amorphous silicon matrix is more open than the crystalline one, and thus can be more readily penetrated by lithium, resulting in almost complete lithiation of the *whole* Si matrix by the end of the 1st (higher voltage) process. This is seen by the almost complete loss of the Si 3.8 Å correlation in the PDF experiment (Figure 3.24, IX) by 200 mV. The clusters that form at this point differ electronically from those of the model compounds – no resonances near 16 ppm are seen in the Li NMR experiment. They are also associated with an increase in intensity of the 4.2 Å correlation. Beyond this point, the Si clusters are lithiated and further broken down (Figure 3.24, X) as seen by the decrease in the Si-Si 2.35 Å correlation and the appearance of the characteristic resonance at 16 ppm, due to Li nearby smaller Si clusters. At the end of the 2nd full discharge, at 0 mV, the fully lithiated $Li_{15+\delta}Si_4$ phase recrystallizes (Figure 3.24, XI).

3.3.3.4. Charge Subsequent to a Partial Discharge

The different mechanism that follows partial discharge to 85 mV is ascribed to the presence of more Si clusters than at 0 mV. The residual clusters can serve multiple nucleation sites within amorphous Li_xSi, these clusters growing during the lower voltage process, by addition of isolated Si and presumably by fusing of some of the smaller clusters (Figure 3.24, green arrows, from III to XII to VII or from X to VI to VII) consistent with the change in the Li NMR spectrum from 85 to 250 mV. In the higher voltage process, the small clusters fuse to form larger amorphous Si domain as Li is extracted, and only a ^7Li signal near 3 ppm remains at 550 mV. Note that the Li spectra following partial charge are very similar to that seen on lithiating the amorphous Si phase, the presence of the larger numbers of Si nuclei allowing delithiation to follow a pathway that is close to that seen on discharge.

3.4. Conclusions

A model for lithiation and delithiation of crystalline silicon is proposed based on PDF and NMR results, to explain the electrochemical phenomena observed during the 1st discharge and all subsequent charge and discharge cycles regardless of the voltage cutoffs used for cycling. The model is composed of 4 mechanisms. Lithiation of crystalline silicon starts and progresses with bond breakage of the Si matrix from the surface by forming both lithiated isolated silicon anions and lithiated silicon clusters until the bulk crystalline Si is consumed and total amorphization is achieved. This is followed by breakage of the remaining Si clusters to form predominantly fully lithiated isolated silicon environments. Key to this mechanism is (i) the difficulty in breaking up the crystalline Si framework, which means that it is kinetically more favorable to lithiate silicon clusters and form isolated Si ions, or smaller clusters, than to break up the framework. (ii) Since a distribution of different Si clusters and anions are formed, the (more thermodynamically stable) crystalline phase expected based on the Li:Si ratio of the amorphous component does not readily nucleate, since this would involve Si-Si bond breakage and rearrangement of the clusters. Only when essentially all of the Si clusters are broken up < 50 mV is it possible to nucleate a crystalline phase comprising isolated Si ions. The mechanism for delithiation of the fully lithiated phase progresses from a small number of nuclei, which are either formed on delithiation or which may still be present in the fully discharged phase. These nuclei grow directly to form the amorphous (delithiated) Si phase without (significant) formation of any intermediate structures or compositions with multiple small clusters. The amorphous Si phase formed on the top of charge contains Si tetrahedra, but no order beyond silicon 2nd coordination shell. The amorphous silicon matrix is much more open, so that the *whole* matrix can now be partially lithiated at the end of the higher voltage process (i.e., with a much lower overpotential than required to break the crystalline framework), partially breaking down the Si network. The lower electrochemical process is associated with the breaking of remaining smaller lithiated silicon clusters and it ends with recrystallization of the fully lithiated phase. If a partially delithiated phase, and one that still contains Si clusters, is delithiated, these clusters appear to serve as nucleation sites, allowing the system to retrace a similar electrochemical pathway to that seen on discharge. In contrast, if lithiation proceeds to form $Li_{15}Si_4$, i.e., the phase with isolated anions, there are few Si nucleation sites, and delithiation proceeds via the growth of only a few Si clusters to form larger Si domains and eventually the amorphous Si phase. Finally, it is suggested that it may be important to control the potential windows over which the material is cycled to optimize both the numbers and type of clusters that are formed and that this may be important in determining the reversibility and capacity retention of this system. For example, cycling the material over the 1st process vs. the 2nd process involves very different rearrangements of the Si matrix/clusters, presumably with different kinetic barriers for reaction.

3.5. References

(1) Obrovac, M. N.; Christensen, L. *Electrochem. Solid-State Lett.* **2004**, *7*, A93.

(2) Obrovac, M. N.; Krause, L. J. *J. Electrochem. Soc.* **2007**, *154*, A103.

(3) Hatchard, T. D.; Dahn, J. R. *J. Electrochem. Soc.* **2004**, *151*, A838.

(4) Li, J.; Smith, A.; Sanderson, R. J.; Hatchard, T. D.; Dunlap, R. A.; Dahn, J. R. *Journal of the Electrochemical Society* **2009**, *156*, A283.

(5) Danet, J.; Brousse, T.; Rasim, K.; Guyomard, D.; Moreau, P. *Physical Chemistry Chemical Physics* **2010**, *12*, 220.

(6) Key, B.; Bhattacharyya, R.; Morcrette, M.; Seznec, V.; Tarascon, J. M.; Grey, C. P. *Journal of the American Chemical Society* **2009**, *131*, 9239.

(7) Qiu, X.; Thompson, J. W.; Billinge, S. J. L. *J. Appl. Crystallogr.* **2004**, *37*, 678.

(8) Farrow, C. L.; Juhas, P.; Liu, J. W.; Bryndin, D.; Bozin, E. S.; Bloch, J.; Proffen, T.; Billinge, S. J. L. *J. Phys. Condens. Matter* **2007**, *19*, 335219/1.

(9) Carr, H. Y.; Purcell, E. M. *Phys. Rev.* **1954**, *94*, 630.

(10) Chevallier, F.; Letellier, M.; Morcrette, M.; Tarascon, J. M.; Frackowiak, E.; Rouzaud, J. N.; Beguin, F. *Electrochem. Solid-State Lett.* **2003**, *6*, A225.

(11) Li, J.; Christensen, L.; Obrovac, M. N.; Hewitt, K. C.; Dahn, J. R. *J. Electrochem. Soc.* **2008**, *155*, A234.

(12) Jiang, M.; Key, B.; Meng, Y. S.; Grey, C. P. *Chemistry of Materials* **2009**, *21*, 2733.

(13) Yamakawa, N.; Jiang, M.; Key, B.; Grey, C. P. *Journal of the American Chemical Society* **2009**, *131*, 10525.

(14) Breger, J.; Dupre, N.; Chupas, P. J.; Lee, P. L.; Proffen, T.; Parise, J. B.; Grey, C. P. *Journal of the American Chemical Society* **2005**, *127*, 7529.

(15) Breger, J.; Meng, Y. S.; Hinuma, Y.; Kumar, S.; Kang, K.; Shao-Horn, Y.; Ceder, G.; Grey, C. P. *Chemistry of Materials* **2006**, *18*, 4768.

(16) Grey, C. P.; Dupre, N. *Chem. Rev. (Washington, DC, U. S.)* **2004**, *104*, 4493.

(17) Meyer, B. M.; Leifer, N.; Sakamoto, S.; Greenbaum, S. G.; Grey, C. P. *Electrochem. Solid-State Lett.* **2005**, *8*, A145.

(18) Nesper, R. *Prog. Solid State Chem.* **1990**, *20*, 1.

(19) Li, H.; Huang, X.; Chen, L.; Zhou, G.; Zhang, Z.; Yu, D.; Mo, Y. J.; Pei, N. *Solid State Ionics* **2000**, *135*, 181.

(20) Hochgatterer, N. S.; Schweiger, M. R.; Koller, S.; Raimann, P. R.; Woehrle, T.; Wurm, C.; Winter, M. *Electrochem. Solid-State Lett.* **2008**, *11*, A76.

(21) Jamnik, J.; Maier, J. *Phys. Chem. Chem. Phys.* **2003**, *5*, 5215.

(22) Krawietz, T. R.; Murray, D. K.; Haw, J. F. *Journal of Physical Chemistry A* **1998**, *102*, 8779.

(23) Stearns, L. A.; Gryko, J.; Diefenbacher, J.; Ramachandran, G. K.; McMillan, P. F. *Journal of Solid State Chemistry* **2003**, *173*, 251.

(24) Peng, B.; Cheng, F.; Tao, Z.; Chen, J. *J. Chem. Phys.* **2010**, *133*, 034701/1.

Chapter 4

Solid State NMR and PDF Studies on Nanoparticulate Crystalline Silicon

Abstract

In this chapter nanoparticulate crystalline silicon lithiation and delithiation mechanisms for lithium ion batteries are studied by using ex-situ solid state magic angle spinning nuclear magnetic resonance and pair distribution function analysis. The main differences vs. bulk lithiation and delithiation are identified by characterizing the amorphous phases formed. The 1st discharge of nanoparticulate crystalline silicon progresses by homogeneous lithiation of the nanoparticle by fragmenting the matrix into large clusters of silicon. The fragmentation process continues along the long plateau-like potential region until a composition, Li_xSi ($x \leq 3.13$), is reached. Beyond this state of charge (SOC), below 75 mV, the amorphous phase has predominantly Li nearby isolated Si clusters. This phase does not crystallize, reacts readily with electrolyte and its short range order is found to be a mixture of $Li_{15}Si_4$ and $Li_{21}Si_5$ which has metallic character while some small Si-Si clusters remain not fully lithiated. Upon charge of this phase, during the 1st voltage process at 300 mV, only metal-like phase is delithiated and small Si-Si clusters are being formed. The clusters do not have any connectivity within each other and no connected Si framework is being formed. During the 2nd voltage process at 480 mV, the small Si-Si clusters come together to form an amorphous Si matrix by extracting the remaining Li from the electrode. Subsequent discharge of this sample, during the 1st voltage process at 250 mV, the amorphous silicon matrix is lithiated and partially dissociated to form low concentration Li environments nearby large Si clusters while the Si connectivity still remains in the electrode. During the 2nd voltage process at 90 mV, large Si clusters start to be fragmented into isolated Si environments and small Si-Si clusters. When almost all the Si connectivity remaining from the amorphous Si matrix is fragmented, the remaining small clusters of Si are fully lithiated to form an electrode predominantly composed of Li nearby isolated Si. This phase, again, does not

crystallize although nano-crystalline domains are formed, and reacts readily with electrolyte with similar composition observed at the end of 1st discharge.

4.1. Introduction

Silicon is an extremely attractive negative electrode material with extremely high theoretical capacity (Chapter 1) [1]. The high capacity is also associated with slow rates discharge and charge steps which limits the applications of silicon for potential commercialization [2]. One possible alternative is to use nanoparticles in order to improve performance and rate capability of crystalline silicon [3,4]. Previous studies have shown that thin films of silicon appears to react differently upon lithiation and delithiation compared to bulk silicon [3,5]. Nanoparticulate Si, upon full lithiation, does not recrystallize to form $Li_{15}Si_4$. The nature of the fully lithiated phase as well as its local structure is yet unknown. Furthermore, delithiation of the fully lithiated phase features two sloping potential regions as opposed to one for lithiated micron-sized silicon. The origin of these plateau-like regions are also unknown. No attempt has been made to characterize the amorphous phases that form upon lithiation and delithiation of nanoparticulate crystalline silicon and link the structure to phenomena observed in electrochemistry and diffraction. The inconsistency between crystalline silicon and nanoparticulate silicon constitutes the motivation for using local structure probes such as NMR and PDF, using a similar strategy carried out in earlier chapters for micron-sized crystalline silicon (Chapter 2 and 3). The results obtained in this chapter are compared with conclusions from earlier chapters to discuss the (de)lithiation mechanism for nanoparticulate Si and to identify the similarities and differences of the amorphous phases that are characterized.

4.2. Experimental Methodology

4.2.1. Electrochemistry

A series of samples were prepared for ex-situ analysis by using 2032 type coin cells and by following a standard assembly procedure: The positive electrode was nanoparticulate crystalline silicon powder (15nm particle size, from Aldrich), milled with super P carbon in 1:1 weight ratio, and the negative electrode was lithium metal (0.38 mm thickness). 1 M $LiPF_6$ dissolved in a 1:1 volumetric mixture of anhydrous ethylene carbonate (EC) and anhydrous dimethyl carbonate (DMC) was used as the electrolyte (Merck, Selectipur^{TM}). A porous borosilicate glass fiber soaked with the electrolyte was used as the separator. The cells were assembled in an argon glove box and cycled galvanostatically between 2.0 and 0.0 V at a C/100 discharge rate with an Arbin Instrument galvanostat/potentiostat at room temperature. After electrochemical cycling, the cells were disassembled in the glove box where the active materials were extracted, dried and packed into 1.8 mm diameter zirconia rotors for MAS NMR analysis and into 1 mm diameter polyimide capillaries sealed with epoxy resin for x-ray scattering experiments at the synchrotron. The NMR spectra of the samples were run a few days after extraction. One 0 mV sample, called “0 mV washed”, was extracted quickly from a cell and washed with DMC to investigate the lithium environments prior to any significant degradation of the lithium silicides, due to reactions with the electrolyte (a self-charge reaction). The second 0 mV “non-washed” sample was treated in the same manner as all the other higher voltage samples, a few hours passing between the end of discharge and the extraction of the sample from the battery. The PDF experiments were conducted days to weeks after the samples were extracted, so it is possible that some side reactions may have occurred.

4.2.2. Diffraction and PDF

Total scattering patterns (Bragg diffraction patterns and diffuse scattering data) were acquired with 2D detectors (GE a-Si and Perkin Elmer a-Si 2D image plates) at the Advanced Photon Source in Argonne National Lab, IL (60 and 90 keV beam energies). 2D images were converted into 1D Q-space vs. Intensity plots by FIT2D program by using CeO_2 calibration standard and PDF patterns (G(r)) were obtained with the PDFGetX2[6] software. The data range used was up to 23 A^{-1} Q. The PDFGui software[7] was used to fit the data. No attempt was made to subtract the PDF signal due to the carbon and the binder from the total signal of the whole electrode composite.

4.2.3. NMR

^{7}Li MAS NMR spectra were acquired at 77.63 MHz using a CMX-200 MHz spectrometer, with a 1.8 mm MAS probe at a 38 kHz spinning speed. All the ^{7}Li spectra were referenced to a 1M LiCl solution at 0 ppm. Rotor-synchronized spin-echoes ($90^o - \tau - 180^o - \tau -$ acq) were used to acquire the spectra, where the values of τ were chosen, such that they were equal to the rotor period (i.e. $\tau = 1$ / spinning frequency). A recycle delay of 0.2 s was used to collect a total of 32000 scans for each sample.

4.3. Results and Discussion

4.3.1. Electrochemistry

An electrochemical profile that is typical of those from samples extracted from a series of different batteries is presented in Figure 4.1. The 1st (irreversible) process that occurs at approx. 0.8 V is primarily due to the reaction with the carbon in the Si/C composite. The lithiation of pristine nanoparticulate silicon is accompanied by a long sloping plateau-like voltage region at approximately 140 mV (Figure 4.2). The sloping profile for the 1st discharge is indicative of a transformation involving primarily two phases (nano-crystalline silicon and an amorphous phase) taking place. Unlike bulk crystalline silicon, nanoparticulate silicon does not recrystallize at the end of the lithiation process to form a phase similar to $Li_{15}Si_4$, although at the end of 1st discharge a similar composition of 3.75 Li per Si is achieved [3,5]. The absence of recrystallization is seen at the end of subsequent discharge cycles. Again, unlike bulk crystalline silicon, two distinct potential regions are observed in the charge cycle (Figure 4.1) appearing at approximately 300 and 480 mV (Figure 4.2). The origins of these plateaus are yet unknown. Upon subsequent discharge following a full charge step, the samples undergo two plateau-like voltage regions appearing approximately 250 and 90 mV, similar to those observed and studied in Chapter 3. The origin of the plateaus are expected to be similar but are discussed in the work described in this chapter nonetheless.

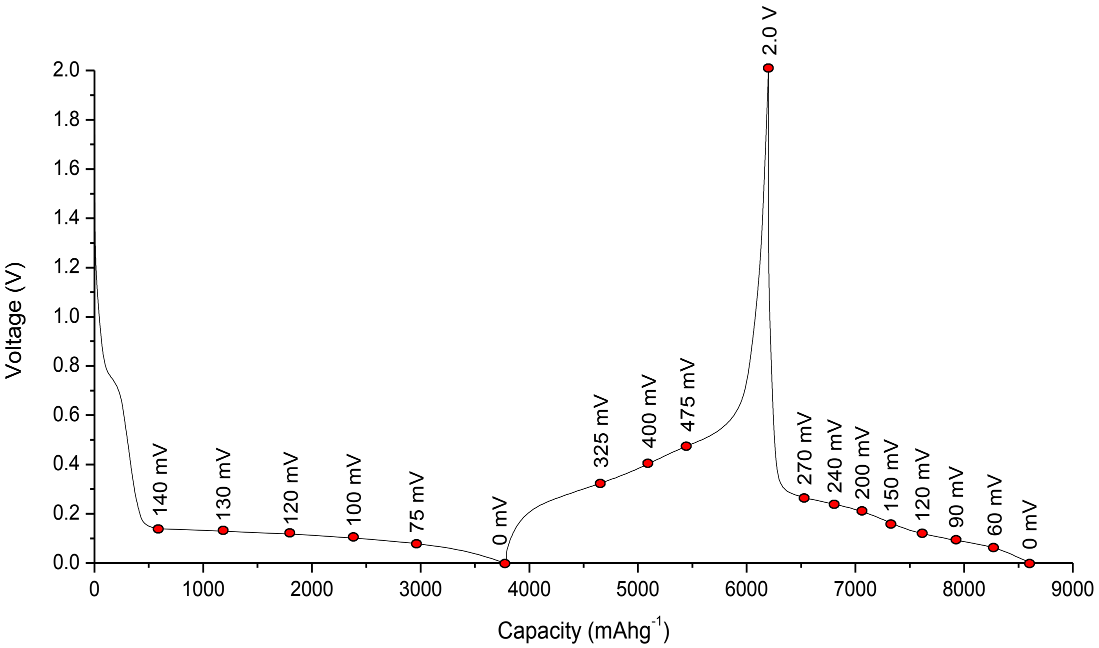

Figure 4.1. The electrochemical profiles for the 1st discharge, 1st charge and 2nd discharge of nanoparticulate crystalline silicon (voltage cutoffs between 2 V and 0 V and with a C/100 current rate). The red points indicate the samples collected for ex-situ PDF and NMR studies.

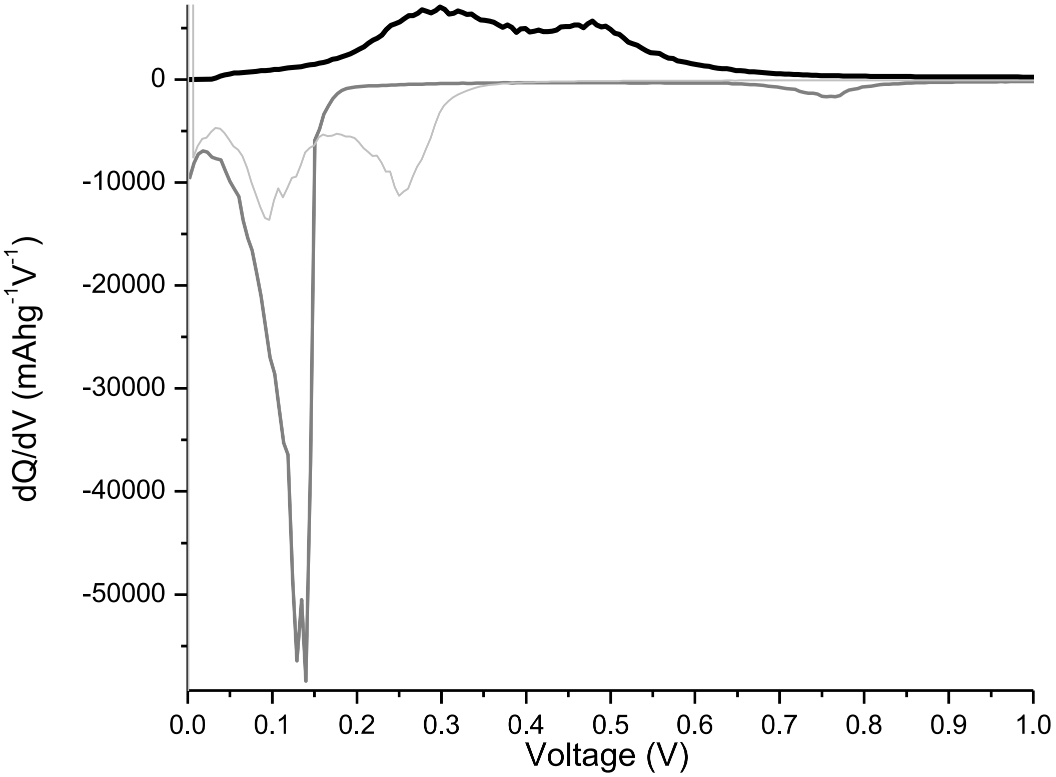

Figure 4.2. Plot of differential capacity vs. potential for the 1st full discharge, 1st full charge and the 2nd full discharge of nanoparticulate crystalline silicon. The negative peak (dark grey line) at 140 mV corresponds to the main process seen in the 1st discharge step. The positive peaks at 300 and 480 mV correspond to the processes in the 1st charge step (black line). The negative peaks at 250 and 90 mV correspond to the processes in the 2nd discharge step (light grey line).

It is demonstrated in Chapter 3 and Chapter 2 that the ^{7}Li NMR shifts of battery samples collected at specific states of charge (or discharge) can be used to provide the local ordering of lithium clusters around specific silicon local structures, i.e. the lithium environments around bonded silicon clusters (dimers, rings, stars and trigonal planar formations) appear at around 18 ppm, whereas, lithium around isolated silicon environments give rise to ^{7}Li resonances at 6 ppm. The same assignment strategy is used to explain the lithium and silicon local environments for nanoparticulate silicon battery samples in the following sections of this chapter.

4.3.2. NMR (1st discharge)

To investigate the different voltage regions in detail during the 1st discharge with ^{7}Li MAS NMR spectroscopy, six coin cells composed of nanoparticulate crystalline silicon as the positive electrode and lithium metal as the negative electrode were stopped at different potentials and the electrode materials were extracted (Figure 4.3). The battery sample arrested at 140 mV, gives rise to a sharp resonance at -1.2 ± 0.2 ppm superimposed on a broader component, which is assigned to diamagnetic environments for Li in carbon (Li_xC), in the (dried) electrolyte solution, in the solid electrolyte interphase (SEI) and possibly in environments created due to reaction with oxides on the surface of the silicon [1,8]. The -1.2 ppm resonance is present in NMR spectra of all of the electrode samples extracted from actual batteries (Figure 4.3).

After 140 mV, the reaction of crystalline silicon with lithium takes over and new ^{7}Li resonances start to appear (Figure 4.3). At 130 and 120 mV, a single broad resonance starts to appear at 2 ppm. This 2 ppm resonance was observed during the charge of lithiated bulk silicon and was tentatively assigned to lithium environments nearby large Si clusters (Chapter 3). The same assignment is used to explain this resonance which suggests that nanoparticulate silicon is lithiated, to form partially lithiated large clusters of bonded Si. The experimental observations for the initial lithiation diverge drastically for bulk and nano-silicon. It could be speculated that the increased surface area and small particle size for nanoparticulate silicon allows lithium to penetrate and form more uniform lithium silicon local environments along the volume of the nanoparticle, a phenomenon which does not appear to take place in bulk silicon.

The resonance appearing at 2 ppm for the initial voltage region of the 1st discharge gradually gains intensity and shifts to 4 ppm for the samples arrested at 100 mV and 75 mV. This experimental observation is consistent with the initial shift assignments, indicating that the homogeneous lithiation and bond breaking in the nanoparticle Si matrix form smaller and smaller Si clusters and an increase in Li concentration surrounding them. For the sample arrested at the end of the full lithiation (0 mV) only one resonance at 8 ppm is observed. This shift is analogous to the fully lithiated crystalline silicon resonance appearing at 6 ppm and predominantly is due to fully lithiated silicon environments (3800 $mAhg^{-1}$, corresponding to full capacity for silicon). A similar shift of 6 ppm was observed for $Li_{15}Si_4$ (Chapters 2 and 3) and is associated with Li nearby isolated Si [1].

Although the local structure of Li atoms indicates full lithiation, nanoparticulate silicon is known to not crystallize to form a phase analogous to $Li_{15}Si_4$ [5]. In order to investigate the inconsistency and explore dynamic processes taking place at the end of the full discharge process, another full discharge sample is arrested for NMR. This sample is extracted from the coin cell and washed with DMC immediately to inhibit side reactions that might take place with residual electrolyte and packed quickly into the rotor for NMR acquisition. The ^7Li MAS NMR spectrum of the non-relaxed sample is plotted in Figure 4.3 (0mV washed). The spectrum contains resonances at -1.2 ppm and 7.8 ppm consistent with the 0 mV sample, however, two new major resonances appear at 38 ppm and 20 ppm which indicate reactive local environments that most likely undergo side reactions with the electrolyte and/or relax rapidly to form the ultimate resonance at 8 ppm. The relative shifts and T_1 relaxation times measured for the new resonances are different compared to the 8 ppm resonance (87, 202 and 160 ms for 38, 20 and 8 ppm resonances, respectively) which may suggest that the NMR shifts of these new local environments are governed by Knight shift, which is also the case for highest lithium containing and more metallic model compound $Li_{21}Si_5$ (^7Li NMR shifts at 93.7 and 70.5 ppm, Chapter 2 and 3).

The Knight shift is indicative of metallic character for the Li local environment for this sample, which is maintained only for a short period of time in electrolyte even though the sample was washed to get rid of residual electrolyte before packing. The relaxation process is illustrated in Figure 4.4 and only the peak at 8 ppm remains after a period as short as 10 hrs. This process is analogous and can be considered similar to the self-discharge process observed at the end of a full discharge cycle for bulk crystalline silicon. The difference between the two processes can be described as follows: The full lithiation of bulk crystalline silicon produces a slightly over-lithiated $Li_{15}Si_4$ semi-crystalline phase which self-discharges in electrolyte to lose the excess lithium, on the other hand, the full lithiation of nanoparticulate crystalline silicon does not trigger crystallization of $Li_{15}Si_4$ but forms metallic local domains which have a similar composition $Li_{15}Si_4$. It must also be noted that there is a mere 0.45 Li per Si difference between $Li_{21}Si_5$ (4.2 Li per Si) and $Li_{15}Si_4$ (3.75 Li per Si). Local over-lithiation for a nanoparticle which contains residual silicon clusters would create a mixture of metallic Li local environments as well as Li nearby isolated Si and Li nearby Si-Si clusters. The synthesized $Li_{21}Si_5$ model compound has also been found to decompose in an Ar glovebox presumably due to trace O_2/H_2O and lose its metallic shift over time and the relaxation phenomenon that is observed for the fully lithiated sample can be analogous to this decomposition. The evidence collected from NMR clearly is clearly not enough to shed light to the nature of the fully lithiated phase. Therefore a complementary local structure probe, x-ray pair distribution function analysis, is used to investigate the loss of silicon short range order of the samples collected during the 1st discharge.

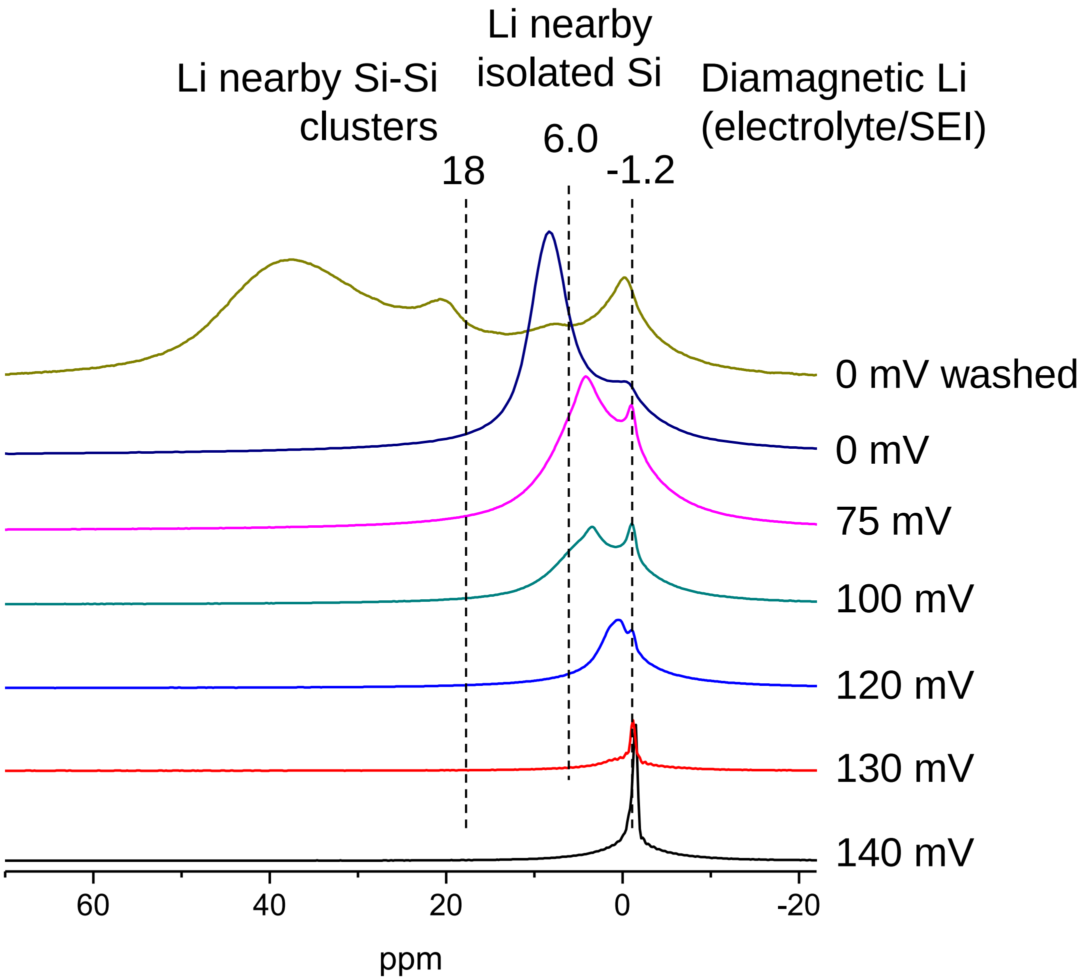

Figure 4.3. *ex situ* ^{7}Li MAS NMR of battery samples stopped during the 1st discharge. Dashed lines indicate resonances with known lithium assignments.

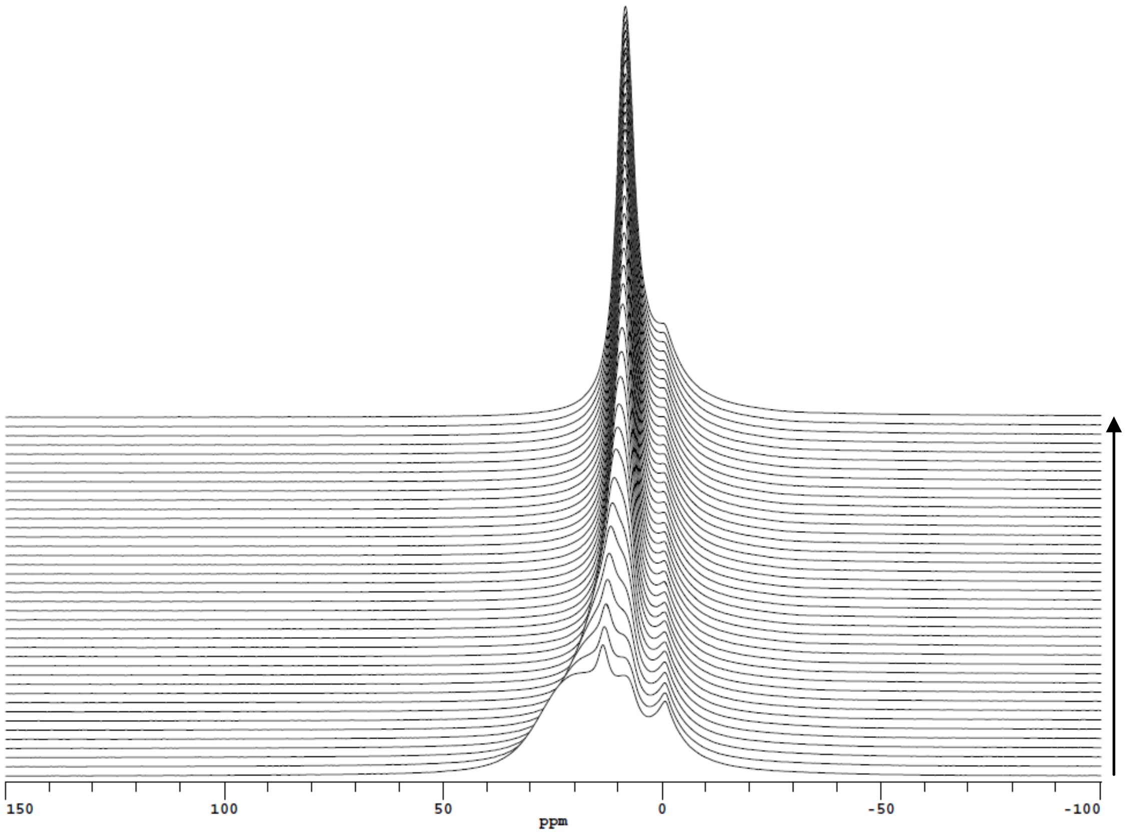

Figure 4.4. Stack plot of a ^{7}Li MAS NMR experiment illustrating the relaxation of the fully discharged phase extracted from a battery. The arrow indicates the time axis.

4.3.3. PDF (1st Discharge) and Discussion of Lithiation Mechanism

The PDF data collected for the samples arrested from batteries during the 1st discharge is plotted in Figure 4.4. Upon 1st discharge of nanoparticulate silicon, the loss of crystallinity can be visually observed to be complete for samples collected below 100 mV. It is also clear that the sample at 0 mV indicates local ordering at 4.8 Å (Figure 4.5, marked with arrow) which is characteristic of the $Li_{15}Si_4$ phase, although no long range ordering for this phase has been observed at any full discharge cycle of nanoparticulate silicon. Furthermore, the crystallographic model for $Li_{21}Si_5$ contains minimum Si – Si distances of 4.6 Å so it is likely that the pair correlation at 4.8 Å belongs to a local Si ordering, characteristic of sub-nano sized $Li_{15}Si_4$ and/or $Li_{21}Si_5$.

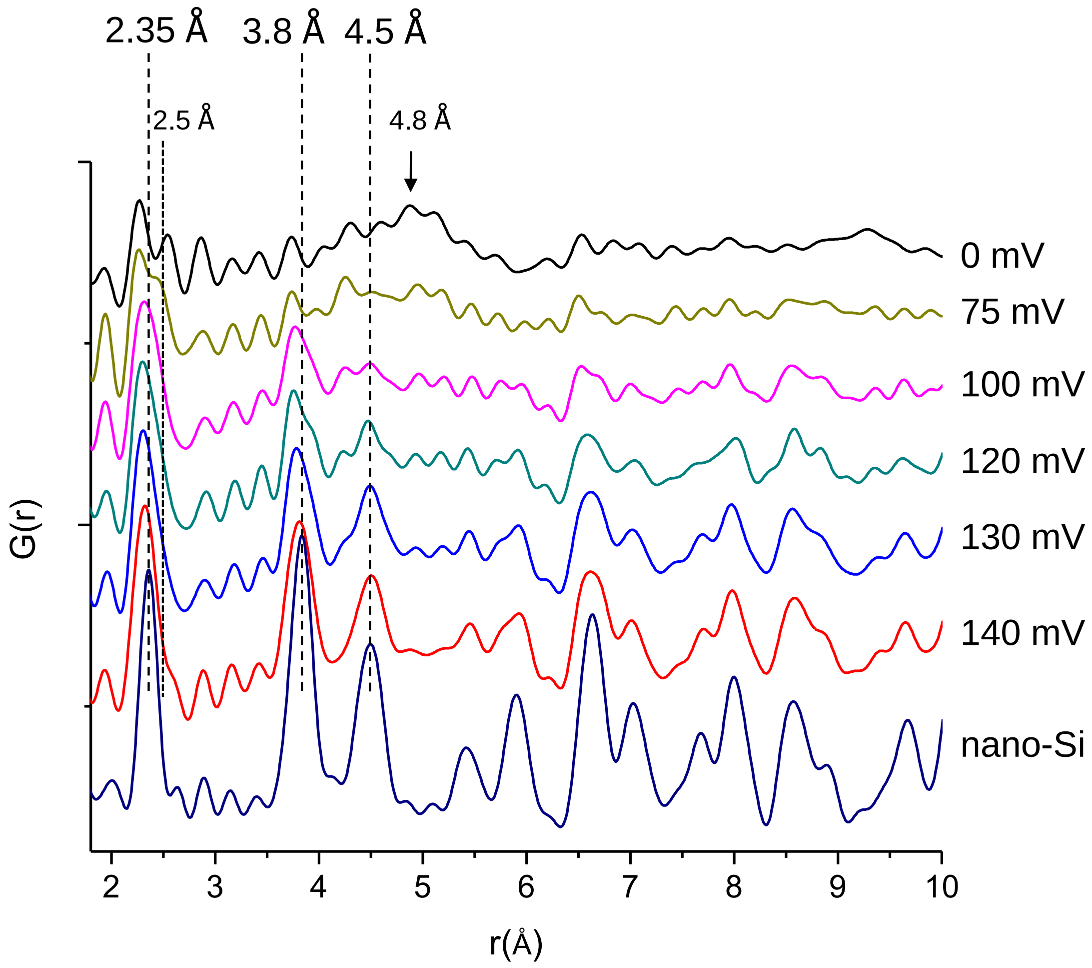

Figure 4.5. *ex situ* PDF patterns of battery samples stopped during the 1st discharge. Dashed lines indicate first, second and third coordination shells of crystalline silicon matrix. The dashed line at 2.5 Å indicates the Li-Si correlation. The arrow indicates the characteristic Si – Si long range distance at 4.8 Å.

The intensities of the peaks due to Si first, second and third coordination shells (see Chapter 3 for detailed explanation of the PDF analysis and significance of Si coordination shells) are gradually lost during the 1st discharge as lithiation proceeds. The intensity of the 4.5 Å peak, which is indicative of the integrity of the Si diamond matrix (long range order in connectivity of Si tetrahedral), is almost completely lost beyond 100 mV (2400 mAhg^{-1}) (Figure 4.5 and 4.6). However at this SOC, the intensities of the 2.35 and 3.8 Å peaks are not totally lost which indicates the presence of small Si-Si clusters in the electrode. On the other hand, the sample collected at 75 mV has no evidence of the 3.8 Å peak and at this state of charge (3000 mAhg^{-1}) some Si-Si bonds still exist (Figure

4.5). The PDF collected at this state of charge also shows the distinct formation of Li-Si correlations at approximately at 2.5 Å. For this reason, deconvoluted integrated intensities are plotted for the 2.35 Å correlation to exclude the intensity due to the 2.5 Å correlation. The loss of intensity for the 3.8 and 2.35 Å correlations can be followed from the plot of integrated area under each respective peak in Figure 4.6. Although, the trend of intensity loss until 3000 $mAhg^{-1}$ is non-linear for both peaks (Figure 4.6), it is indicative of the fact that up to this SOC, the Si-Si correlations are being lost for both 1st and 2nd coordination shells continuously, simultaneously and non-preferentially. Combined with the observations from NMR experiments, it can be suggested that until this SOC is reached, the lithiation of nanoparticulate crystalline silicon matrix undergoes a solid solution phase transformation, from crystalline to an amorphous lithiated silicide phase with composition Li_xSi ($x \leq 3.13$, derived from 3000 $mAhg^{-1}$). However, it must be noted that complete bond breakage for Si dumbbells is not achieved. Further lithiation of a sample at this SOC, interestingly, results in almost no significant change in intensity of silicon coordination shell peaks but an increase in intensity of the 4.8 Å and 2.5 Å correlations indicative of the formation of the new metallic phase with isolated Si (Figure 4.6). Combined with the NMR data, it can be suggested that beyond 75 mV (3000 $mAhg^{-1}$), full lithiation is achieved by oversaturation (compared to micron-sized Si lithiation) of individual isolated Si, as opposed to breaking down residual Si-Si dumbbells. The phase distribution for the 0 mV sample is expected, based on experimental data, to contain (1) Li nearby residual Si-Si clusters (which explains the broad NMR shift for this sample appearing at 8 ppm but not at 6 ppm which is the shift expected for fully lithiated $Li_{15}Si_4$ phase) and (2) Li nearby isolated Si in which the composition is estimated to be between $Li_{3.75}Si$ and $Li_{4.2}Si$ although long range order of the overlithiated phase(s) is not induced. This is most significant, since in case of bulk silicon, macrometer-sized particles do not accommodate excess Li to overcome the diamagnetic to metallic transition barrier and form a phase, locally similar to $Li_{21}Si_5$. However, a similar relaxation (self-discharge ?) mechanism is also observed for the fully lithiated nanoparticulate silicon with NMR, suggesting a similar reactivity of this new amorphous phase compared to the fully lithiated micron-sized crystalline silicon. It must be noted that the reactivities of the fully lithiated nano Si and micron-sized Si has not been investigated in detail.

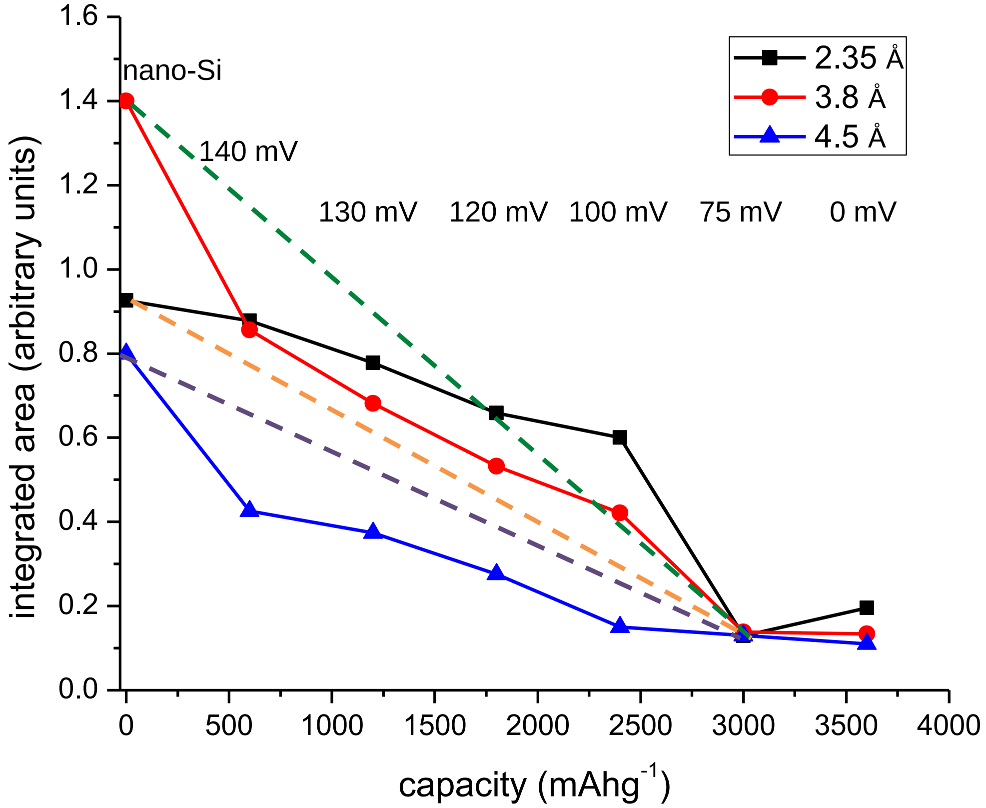

Figure 4.6. Integrated area under the 1st three PDF correlations peaks, for battery samples stopped during the 1st discharge. The dashed lines indicate loss of intensity predictions for each correlation assuming a hypothetical two phase transformation.

4.3.4. NMR (Charge)

To investigate the delithiation mechanism subsequent to a full discharge step, five coin cells arrested at specific SOCs were used to obtain the ^{7}Li MAS NMR data. Two electrochemical processes can be observed from the electrochemistry profile (Figure 4.1 and 4.2, at 300 and 480 mV). During the 1st process, the NMR spectra changes most dramatically, which can be followed from Figure 4.7. The spectrum collected for the 0mV sample loses all intensity and the only resonances that can be observed for the sample collected at 320 mV (collected near the end of the 300 mV process) are at -1.2 ppm and 1.0 ppm (marked with a red dashed line). The former is due to the electrolyte/SEI and the latter is again (see Chapter 3 and NMR (1st discharge)) ascribed to low concentrations of Li trapped within large clusters of amorphous Si matrix which is likely to start to form at this SOC. Compared to the 320 mV sample spectrum, at the very end of the 1st process, at 400 mV, where the 2nd higher voltage process (480 mV) takes over, the 1.0 ppm resonance loses intensity which continues until the end of the 2nd process, ending at 2.0 V.

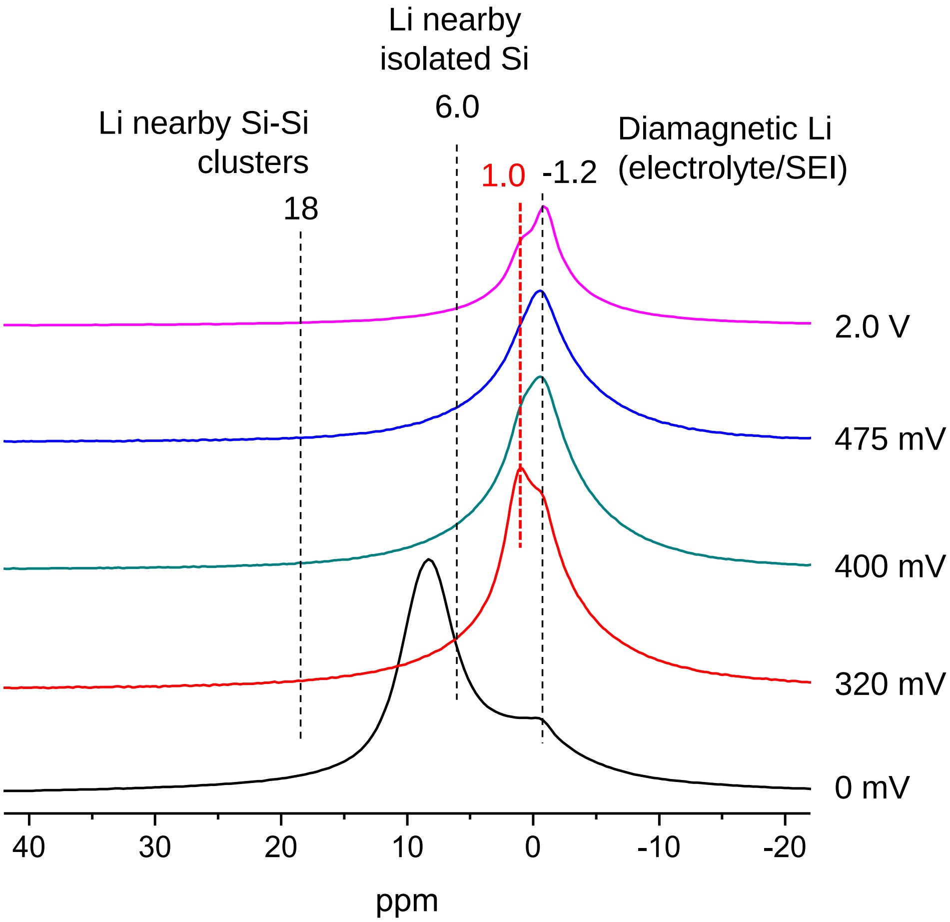

Figure 4.7. *ex situ* ^{7}Li MAS NMR of battery samples stopped during the 1st charge. Dashed lines indicate resonances with known lithium assignments. The red dashed line indicates the resonance at 1.0 ppm.

4.3.5. PDF (Charge) and Discussion of Delithiation Mechanism

The PDF data collected for the samples arrested from batteries during the 1st charge is plotted in Figure 4.8. Upon charge of fully lithiated nanoparticular silicon, the most obvious change in PDF is the loss of short-medium range order (up to 15 Å) in the 1st voltage process (300 mV process). This is associated with the loss of intensity of the

4.8 Å correlation, indicating the delithiation from the $Li_{15}Si_4$/$Li_{21}Si_5$ phase during the 1st process. When compared with the 0 mV sample PDF, at 320 mV, the 2.5 Å (marked with red dashed line) and 2.85 Å (marked with arrow) correlations disappear almost completely, which indicates delithiation and loss of Li-Si and Li-Li correlations respectively. As for Si-Si correlations, the 2.35 Å correlation is observed to gain intensity, suggesting formation of silicon bonds (dumbbells or other small units). However, at 320 mV, no regeneration of the 3.8 Å correlation is observed (Figure 4.8). This observation is significant because, not only it agrees with the NMR results but indicates that during the 1st voltage process, only metal-like phase is delithiated and small Si-Si clusters are being formed and that these clusters do not have any connectivity within each other and no amorphous matrix is being formed. For the samples collected above 320 mV (Figure 4.8, 400 mV, 475 mV and 2.0 V), however, a clear increase in intensity of both 2.35 Å and 3.8 Å peaks is observed. This suggests that the 2nd voltage process mostly brings about the small Si-Si clusters to form a larger amorphous Si matrix by delithiating the remaining Li in the sample.

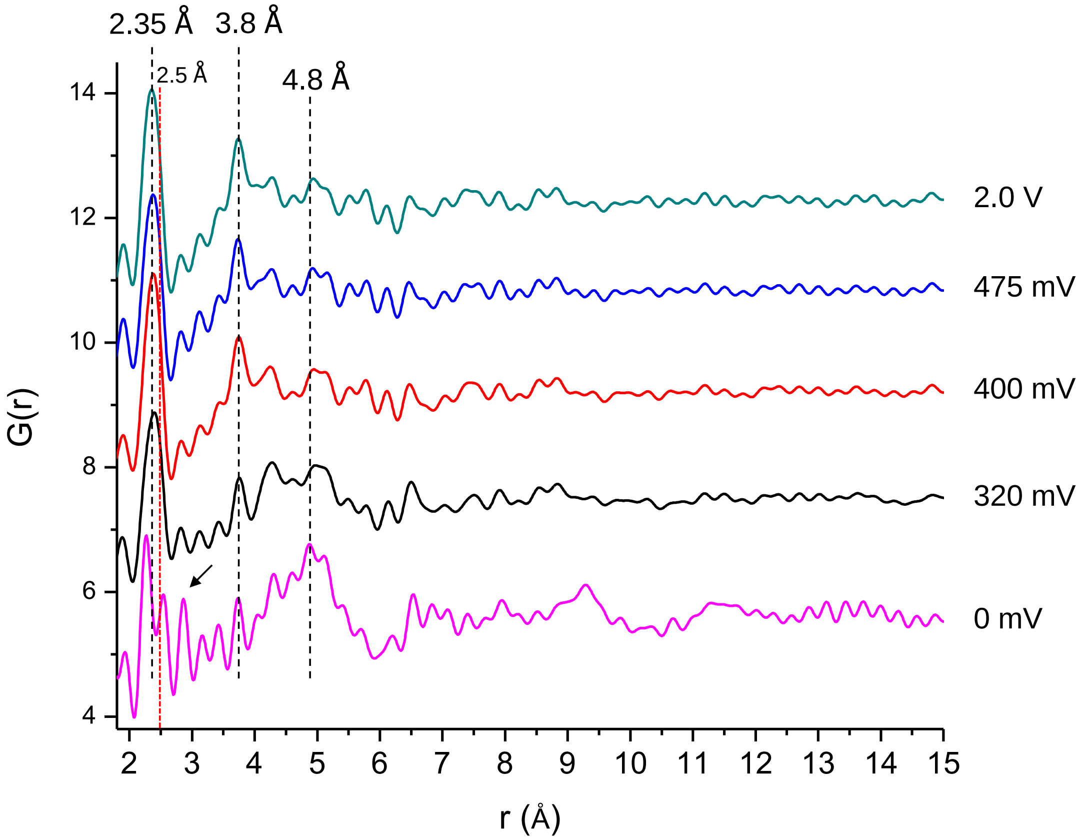

Figure 4.8. *ex situ* PDF patterns of battery samples stopped during the 1st charge. Dashed lines indicate first and second coordination shells of crystalline silicon matrix. The dashed line at 4.8 Å indicates the characteristic Si – Si long range distance. The arrow indicates the Li-Si/Li-Li correlation at 2.85 Å.

4.3.6. NMR (2nd Discharge)

To investigate the different voltage regions in detail during the 2nd discharge with ^{7}Li MAS NMR spectroscopy, ten coin cells composed of nanoparticulate crystalline silicon as the positive electrode and lithium metal as the negative electrode were stopped at different potentials and the electrode materials were extracted (Figure 4.9). The spectrum of the battery sample arrested at 270 mV contains the resonance appearing at 1.4 ppm which gains intensity and shifts gradually to 2.7 ppm until 150 mV is reached (Figure 4.9). This corresponds to the 1st electrochemical process centered at 250 mV (Figure 4.1 and 4.2). The NMR data, using the insight gained from the 1st discharge step, is interpreted such that the amorphous silicon matrix is delithiated and partially dissociated to form low concentration Li environments nearby large Si clusters. This also indicates that Si connectivity still remains in the electrode. At 120 mV, two additional resonances, at 6 ppm and 9 ppm (marked with arrow), appear in the spectrum. The former was assigned to Li nearby isolated Si and the latter is similar to the resonances observed for the 2nd discharge of crystalline silicon (see Chapter 3) and assigned to Li nearby small clusters of Si-Si (dumbbells, chains, stars). The broad collection of resonances at this SOC is interpreted as such that the lithiation, i.e. lithium concentration, beyond the 1st process comes to a threshold at which point large Si clusters start to be fragmented into isolated Si environments and small Si-Si clusters. This mechanism corresponds to the beginning of the 2nd voltage process which is centered at 90 mV (Figure 4.1 and 4.2). Below 120 mV, for samples 90 and 60 mV, the spectra shows that 2.7 ppm resonance continues to lose intensity while the resonances at 6 ppm and 9 ppm gain in intensity. Finally, below 60 mV, at 0 mV, when almost all the Si connectivity remaining from the amorphous Si matrix is fragmented, the remaining small clusters of Si are fully lithiated to form an electrode predominantly composed of Li nearby isolated Si (6 ppm resonance, 0 mV, Figure 4.9).

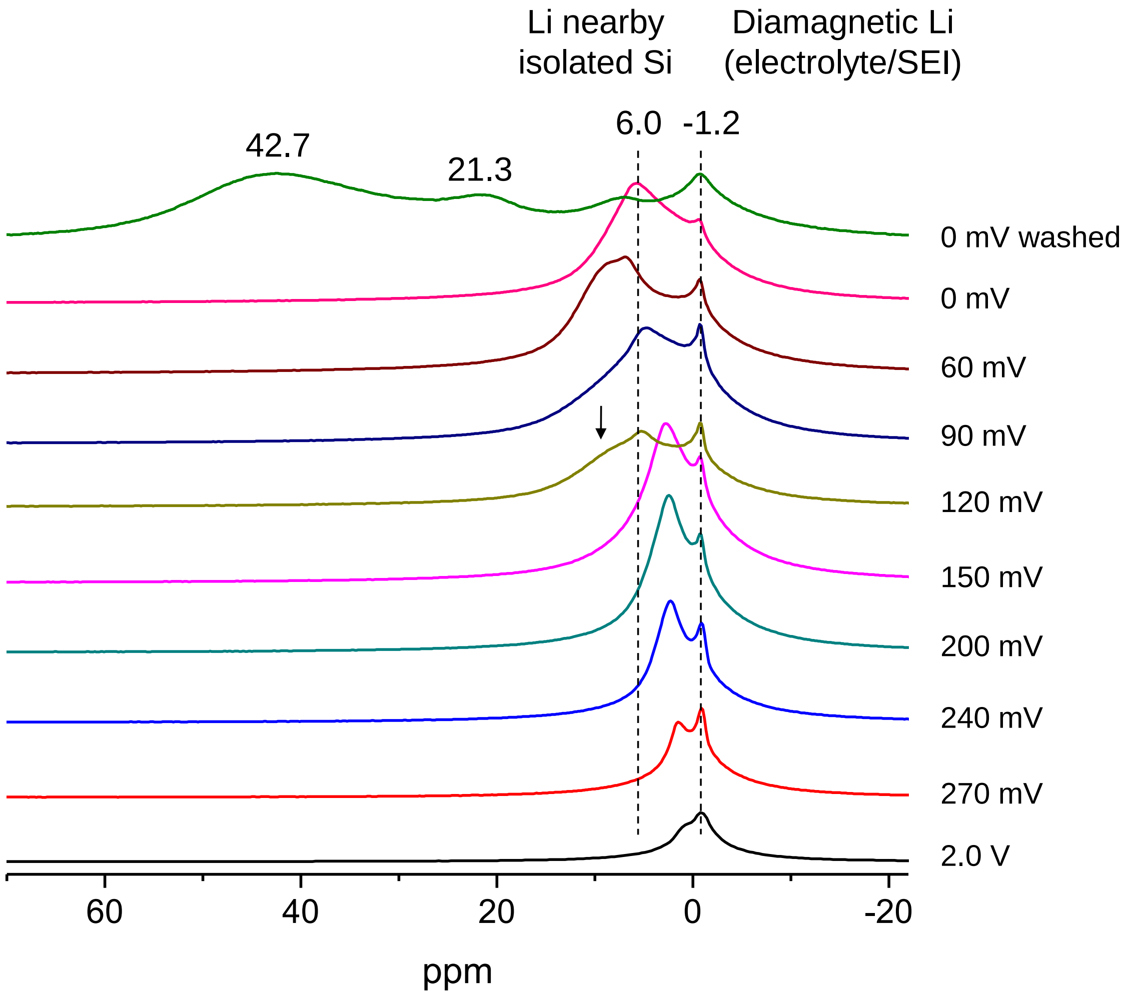

Figure 4.9. *ex situ* ^{7}Li MAS NMR of battery samples stopped during the 2nd discharge. Dashed lines indicate resonances with known lithium assignments. The arrow indicates the appereance of Li nearby small Si-Si clusters.

Another full discharge sample was arrested for NMR at the end of the 2nd discharge. This sample was extracted from the coin cell and washed with DMC immediately to inhibit side reactions that might take place with residual electrolyte and packed quickly into the rotor for NMR acquisition. The ^{7}Li MAS NMR spectrum of the non-relaxed sample is plotted in Figure 4.9 (0mV washed). The spectrum contains resonances at -1.2 ppm and 7.8 ppm consistent with 0 mV sample, and again, two major resonances are observed at 42.7 ppm and 21.3 ppm which indicate reactive local environments that most likely undergo side reactions with the electrolyte and/or relax rapidly to form the ultimate resonance at 8 ppm.

4.3.7. PDF (2nd discharge) and Discussion of Delithiation Mechanism

The PDF data collected for the samples arrested from batteries during the 2nd discharge is plotted in Figure 4.10. Upon discharge of amorphous nanoparticulate Si matrix, two voltage processes centered at 250 and 90 mV are observed in the electrochemical profile (Figure 4.1 and 4.2). The changes in PDF patterns of the samples collected during the 1st process can be visually observed for 2.35 Å and 3.8 Å peaks, as both peaks lose intensity (Figure 4.10 and 4.11). The 2.35 Å correlation loses more than 70% of its initial intensity whereas 3.8 Å correlation loses approximately 50% of its initial intensity by 150 mV SOC. This indicates fragmentation of the amorphous nanoparticulate silicon matrix has taken place during the 1st process. Along the 2nd voltage process, after 150 mV, the peak intensities do not decrease significantly, indicating that the fragmentation, as suggested by NMR, is complete at the end of the 1st process. At and after 120 mV, the 2.5 Å peak starts to appear due to increasing concentration of Li-Si correlations, and more importantly the peak at 4.8 Å appears which indicates the local ordering of the isolated Si phase.

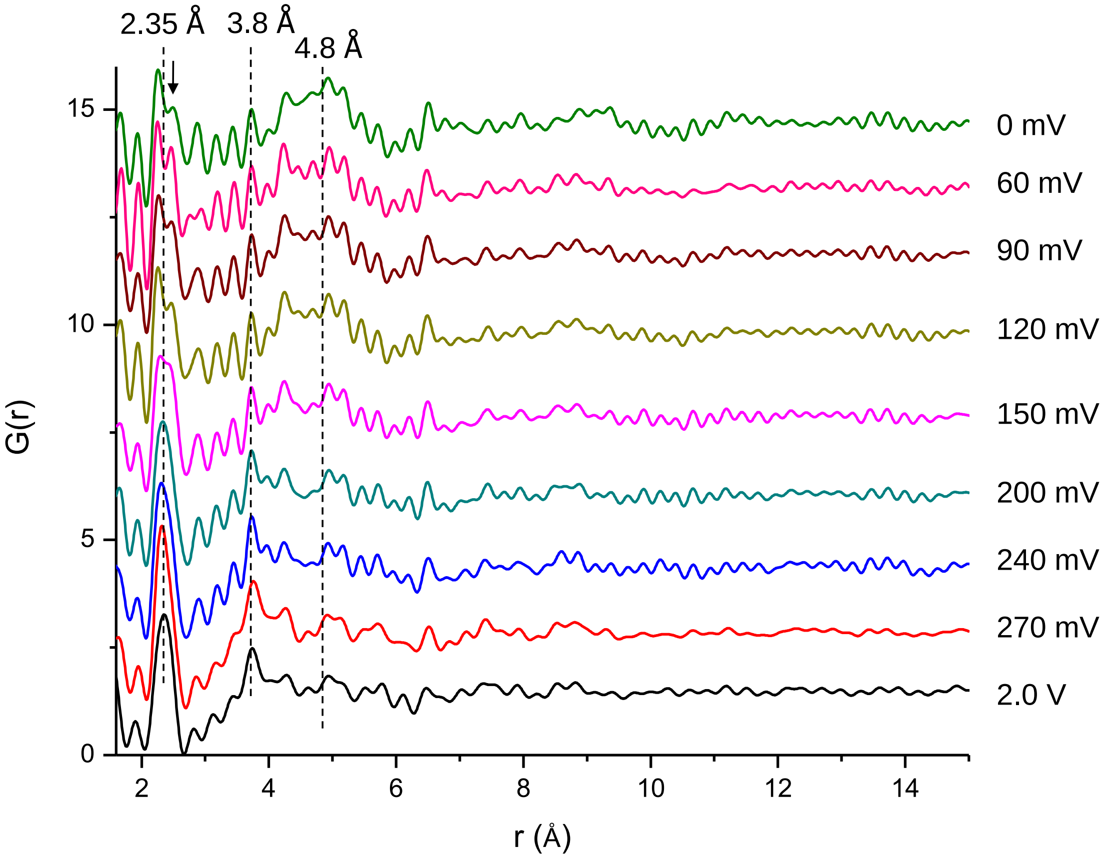

Figure 4.10. *ex situ* PDF patterns of battery samples stopped during the 2nd discharge. Dashed lines indicate first and second coordination shells of crystalline silicon matrix. The dashed line at 4.8 Å indicates the characteristic Si – Si distance for non-bonded Si. The arrow indicates the Li-Si correlation at 2.5 Å.

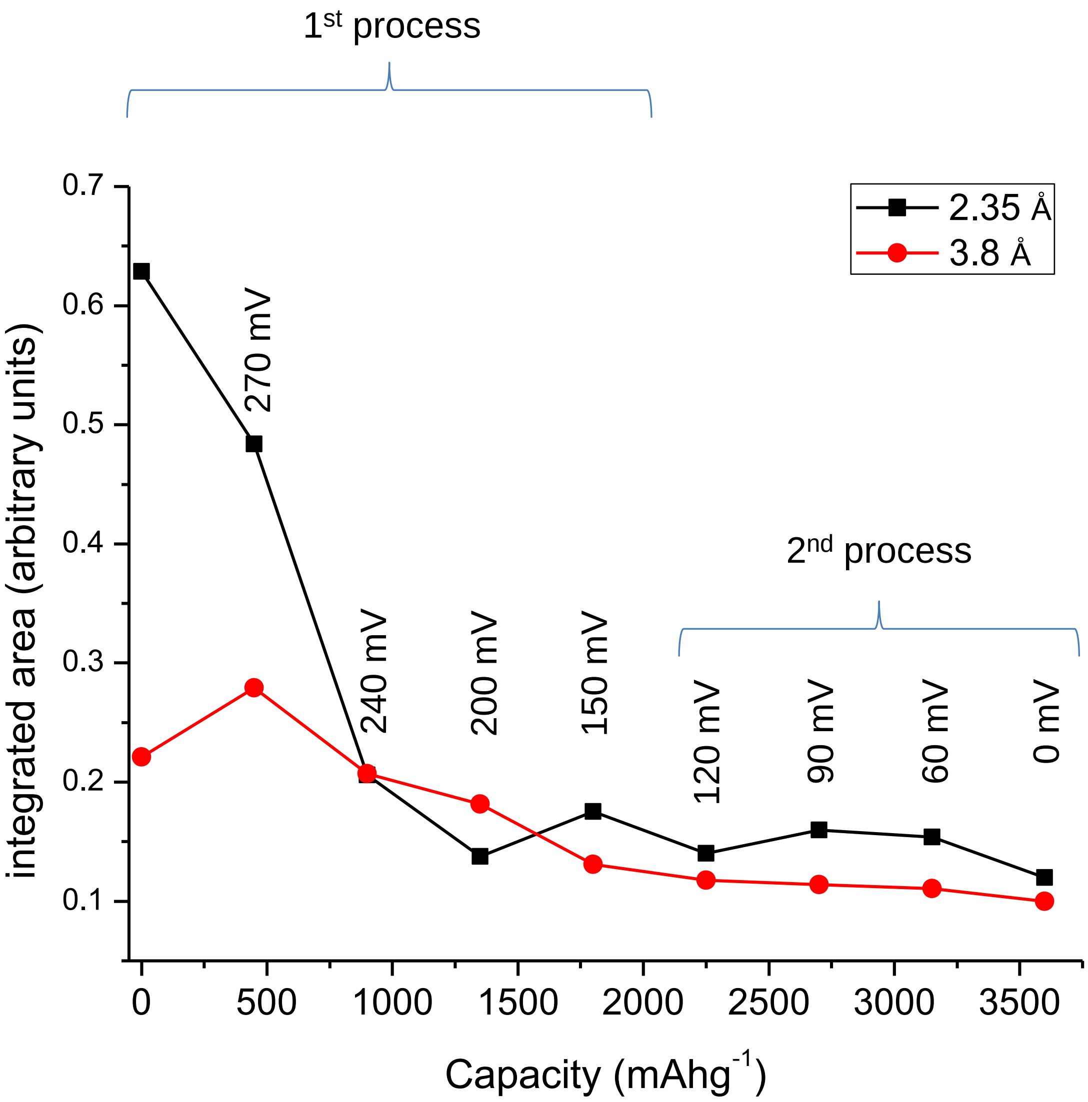

Figure 4.11. Integrated area under the 1st two PDF correlations peaks, for battery samples stopped during the 2nd discharge.

4.4. Summary of (De)lithiation Mechanisms for Nanoparticulate Crystalline Silicon and Conclusions

Based on the experimental data, the 1st discharge of nanoparticulate crystalline silicon progresses by lithiation of the nanoparticle by fragmenting the matrix into large clusters of silicon. The fragmentation process continues along the long plateau-like potential region until a composition, Li_xSi ($x \leq 3.13$), is reached. Beyond this SOC, below 75 mV, the amorphous phase has predominantly Li nearby isolated Si clusters. This phase does not locally crystallize but form nano-clusters up to 1nm in diameter, reacts readily with electrolyte and its short range order is found to be a mixture of $Li_{15}Si_4$ and $Li_{21}Si_5$. Some small Si-Si clusters remain not fully lithiated. Upon charge of this phase, during the 1st voltage process at 300 mV, only the metal-like phase is delithiated and small Si-Si clusters are formed. The clusters do not have any connectivity within each other and no amorphous Si matrix is formed. During the 2nd voltage process at 480 mV, the small Si-Si clusters come together to form a larger amorphous Si matrix by extracting the remaining Li from the electrode. Subsequent discharge of the sample at this SOC, during the 1st voltage process at 250 mV, the amorphous silicon matrix is delithiated and partially dissociated to form low concentration Li environments nearby large Si clusters while Si connectivity is still remaining in the electrode. During the 2nd voltage process at 90 mV, large Si clusters start to be fragmented into isolated Si environments and small Si-Si clusters. When almost all the Si connectivity remaining from the amorphous Si matrix is fragmented, remaining small clusters of Si are fully lithiated to form an electrode predominantly composed of Li nearby isolated Si. This phase, again, does not crystallize, and reacts readily with electrolyte with similar composition observed at the end of 1st discharge. However, it must be noted that the side reactions at the surface of Si is more severe for nanoparticulate Si and it is possible that the samples collected for NMR and PDF analysis could have been undergone decomposition.

4.5. References

(1) Key, B.; Bhattacharyya, R.; Morcrette, M.; Seznec, V.; Tarascon, J. M.; Grey, C. P. *Journal of the American Chemical Society* **2009**, *131*, 9239.

(2) Obrovac, M. N.; Krause, L. J. *J. Electrochem. Soc.* **2007**, *154*, A103.

(3) Holzapfel, M.; Buqa, H.; Hardwick, L. J.; Hahn, M.; Wuersig, A.; Scheifele, W.; Novak, P.; Koetz, R.; Veit, C.; Petrat, F.-M. *Electrochim. Acta* **2006**, *52*, 973.

(4) Chan, C. K.; Peng, H.; Liu, G.; McIlwrath, K.; Zhang, X. F.; Huggins, R. A.; Cui, Y. *Nat. Nanotechnol.* **2008**, *3*, 31.

(5) Hatchard, T. D.; Dahn, J. R. *J. Electrochem. Soc.* **2004**, *151*, A838.

(6) Qiu, X.; Thompson, J. W.; Billinge, S. J. L. *J. Appl. Crystallogr.* **2004**, *37*, 678.

(7) Farrow, C. L.; Juhas, P.; Liu, J. W.; Bryndin, D.; Bozin, E. S.; Bloch, J.; Proffen, T.; Billinge, S. J. L. *J. Phys. Condens. Matter* **2007**, *19*, 335219/1.

(8) Meyer, B. M.; Leifer, N.; Sakamoto, S.; Greenbaum, S. G.; Grey, C. P. *Electrochem. Solid-State Lett.* **2005**, *8*, A145.

Chapter 5

In situ NMR Observation of the Formation of Metallic Lithium Microstructures in Lithium Batteries

Abstract

Lithium metal has the highest volumetric and gravimetric energy density of all negative electrode materials, when used as an electrode material in a lithium rechargeable battery. However, the formation of lithium dendrites and/or “moss” on the metal electrode surface can lead to short circuits, following several electrochemical charge-discharge cycles, particularly at high rates, rendering this class of batteries potentially unsafe and unusable due to the risk of fire and explosion. Many recent investigations have focused on the development of methods to prevent moss/dendrite formation. In parallel, it is important to quantify Li moss formation, to identify the conditions under which it forms. Although optical and electron microscopy can visually monitor the morphology of lithium electrode surface and hence the moss formation, such methods are not well suited for quantitative studies. In this chapter, the use of in-situ NMR spectroscopy, to provide time-resolved, quantitative information about the nature of the metallic lithium deposited on lithium metal electrodes is reported for the first time.

5.1. Introduction

Lithium-ion batteries (LIBs), due to their very high gravimetric and volumetric energy densities, are widely used as electrical-energy storage devices. Owing to their increasing power and energy capabilities, together with their enhanced cycle life, LIBs are now also being developed for use in the automobile industry[1,2]. With these new applications for LIBs comes an even larger demand for more energy from these devices, and thus for electrode materials that store more Li. In principle, Li metal represents the ultimate LIB negative electrode (anode) having a factor of 10 higher specific energy density than lithiated graphite[2]. However, it suffers from at least one serious disadvantage: upon several charge and discharge cycles in non-aqueous electrolytes, dendritic and/or mossy structures of lithium metal are formed on the lithium metal anode, which poses a potentially disastrous safety issue. The dendritic structures — first reported as early as 1980[3] — may dissociate from the anode and remain as floating structures in the electrolyte (known as dead lithium). These dead lithium fibers, along with fibers that grow directly from the electrode, may result in short circuits, causing spontaneous high-rate discharge[2]. This can result in rapid overheating of the battery leading to fire hazards associated with the flammable organic electrolyte[2]. These issues have been a significant impediment to the commercialization of lithium metal batteries. However, the comparatively low volumetric and gravimetric capacities of LIBs using a graphite anode have created a resurgence of interest in lithium metal batteries[4-6]. Indeed, the high capacities that are quoted for Li-air and Li-sulfur batteries, which have attracted considerable recent attention, are based on the use of Li-metal negative electrodes.

Considerable effort has been devoted to prevent moss and dendrite formation on lithium metal anodes during cycling[4,5,7-9] and to understand the negative impacts of dendritic growth on the various aspects of battery cycling. Orsini *et al.* showed, by using scanning electron microscopy (SEM), that there was a direct correlation between dendrite formation and the current density, with larger amounts of dendritic deposits forming at higher current densities[7]. However the SEM method does not provide a way of accurately quantifying the amount of such micro-structures[7]. Studies of mossy or dendritic lithium often use the capacity loss and cycling efficiency as a measure of dendrite formation, although such observations can again only provide a qualitative estimate of the amount of this morphology[4,5]. There have been efforts to theoretically model the dendritic growth, through studies that focus on the morphology of dendritic whiskers (the size, shape and growth)[10-12], but experimental methods that allow *direct quantitative* estimates of mossy or dendritic structures remain elusive.

Li NMR spectroscopy, when performed *in-situ* during electrochemical cycling is a non-invasive method for investigating the structural changes that can occur in electrode materials[13-16]. Since the ^{7}Li signal (spin = 3/2, 92.5% abundance) can be acquired on a time scale that is much faster than the typical charge-discharge cycle (because of high sensitivity of ^{7}Li NMR), the structural changes that occur in the active material at various states-of-charge can be detected and quantified by recording spectral snapshots at suitable time intervals[13]. The NMR approach described here relies on the finite ability of the radio frequency (rf) field, used to excite the Li nuclei, to penetrate the bulk lithium metal electrode beyond tens of micrometers, the so-called "skin-depth"[17], problem. The skin depth, *d*, can be readily calculated since it is a function of known physical constants and the properties of the relevant metal:

$$d = \frac{1}{\sqrt{\pi \mu_0}} \sqrt{\frac{\rho}{\mu_r f}}, \qquad [5.1]$$

where, μ_o is the permeability of the vacuum (=4π 10^{-7} mkgA^{-2}s^{-2})[18] , μ_r is the relative permeability of the metal (for lithium, μ_r = 1.4 [18]), ρ is the resistivity of the metal (92.8 nΩm for Li [18]) and *f* is the frequency of the applied rf field (i.e., the Larmor frequency which is 77.8 MHz in this study). Using these values, a value for *d* of 14.7 μm is calculated for lithium. (N.b. use of a higher magnetic field strength for NMR will lead to a smaller skin depth). Since the rf only penetrates the sub-surface region, the bulk metal signal is proportional to the area of the metal, and not its volume (see Figure 5.1, and equations 5.5 and 5.6). In this chapter, it is shown that NMR spectroscopy performed *in-situ* in conjunction with electrochemical cycling is capable of dynamically monitoring the growth and stripping of lithium microstructures. Using simple calculations based on the skin-depth of metallic structures under radiofrequency excitations, it is shown that it is possible to quantify the amount of moss/dendritic Li formed.

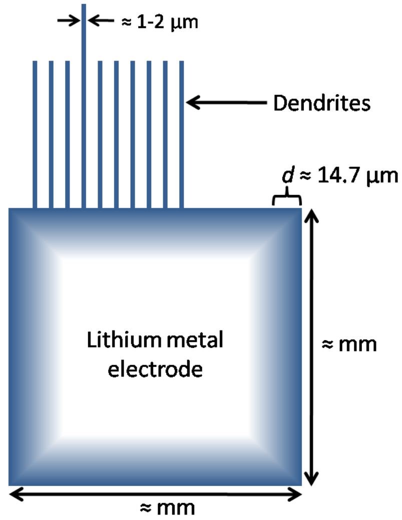

Figure 5.1. Cartoon showing the rf penetration in a block of lithium metal and in the whisker-like dendritic structures. The fraction of the metal block excited by the rf field depends on both the skin depth, d, and its surface area A. The intensity of the blue color depicts the strength of the rf field. The white region inside the metal block depicts the absence of rf field.

5.2. Experimental Methodology

5.2.1. LIB Cells

The batteries used for the *in situ* NMR studies were prepared in an Argon-filled glovebox using a flexible battery design, modified from Bellcore's plastic lithium-ion battery technology [14,15]. The lithium electrodes in all the cells were prepared by brushing a lithium strip (Aldrich, 99.9%, thickness 0.38mm) so as to dislodge some of the native film (oxide, carbonate, etc.), with no attempt being made to polish the electrode surface prior to use. A porous glass microfiber separator (Whatmann, type GF/B) of approximate 1 mm thickness soaked with the electrolyte was used as a separator.

5.2.2. $LiCoO_2$-based cells

Positive electrodes containing $LiCoO_2$ (with desert-rose structure[19]) as an active material were prepared by mixing 7:1.5:1.5 weight ratio of $LiCoO_2$ (typically 8 mg) super P carbon and polytetrafluoroethylene (PTFE). The self-supporting mixture was then pressed on aluminum mesh on one side, leaving the other end of the mesh as the current collector. The negative electrode was prepared by pressing two thin strips of lithium metal (each having dimensions 8 mm x 4 mm x 0.38 mm, cut from a ribbon purchased from Aldrich, purity 99.9%) onto a copper wire mesh, which serves as the current collector. 1M $LiPF_6$ dissolved in a 1:1 volumetric mixture of anhydrous ethylene carbonate (EC) and anhydrous dimethyl carbonate (DMC) was used as the electrolyte.

5.2.3. Symmetrical cells

Electrodes were prepared by cleaning the lithium metal (Aldrich, 99.9%) with hexane before pressing single strips of lithium metal (having dimensions 4 mm x 10 mm x 0.38 mm) on to a copper wire mesh. Two liquid electrolytes were tested (i) butyl-methylpyrrolidinium bis(trifluoromethanesulfonyl)imide (C_4mpyr TFSI; Merck) + 0.5 mol.kg^{-1} lithium bis(trifluoromethanesulfonyl)imide (3M LiTFSI; electrolyte prepared in CSIRO laboratories[20]); <20ppm H_2O and (ii) 1-ethyl-3-methylimidazolium tetrafluoroborate (C_2mIm BF_4, Solvent Innovations, 93.5% purity; 350 ppm H_2O) + 0.5 mol.kg^{-1} $LiBF_4$ (Stella Corporation, dried under vacuum at 140 °C prior to use) + 10wt% Vinylene Carbonate (VC; Aldrich, 99% purity)[20].

The cell components were assembled in heat-sealable polyester bags (Kapak Corporation, type 500-24) which were hermetically sealed inside an argon glove box. The average final dimensions of the cells were 12 mm x 5 mm x approx. 2 mm. Galvanostatic cycling, with chosen potential limits, was performed by using either a Bio-Logic Science Instruments VSP potentiostat/galvanostat or an Arbin cycler.

5.2.4. NMR

Experiments were performed with a Chemagnetics spectrometer at operating proton frequency of 200 MHz (^{7}Li frequency is 77.8 MHz) at room temperature. A single resonance static probe with 5mm solenoidal coil tuned at 77.8 MHz was used for all experiments. The RF power used was 100 kHz (ω_1). The pulse width π/2 was kept fixed at 2.5 μs to ensure $\omega_1\tau_p = \pi / 2$. The details of the experimental setup for the in-situ NMR are described elsewhere[13]. During all experiments (unless otherwise specified) the plane of the lithium metal electrode of the batteries was oriented perpendicular with respect to the magnetic field. The NMR spectrometer was synchronized with the electrochemical cycler and series of spectra were recorded in uniform intervals during the entire length of the electrochemical cycles for each cell. The recycle delay has been chosen to be long enough (1s) compared to the measured longitudinal spin-lattice relaxation time (T_1) of lithium metal (~100 ms), in order to avoid saturation of the lithium signal. Since the Li metal NMR signal is shifted far from the spectral region where the other components of the battery resonate, in the batteries investigated here, other Li signals, such that from the electrolyte or the positive electrode material appear at a high field region in the range of 0-100 ppm. Thus the NMR signal from the metal electrode can easily be separated from these signals. The recorded series of spectra were processed by using a set of MatLab scripts that perform automatic phase and baseline corrections and deconvolution of the Knight-shifted peaks (within a range of 250 to 300 ppm) with a combination of Lorentzian/Gaussian lineshapes. The deconvolution has been performed by least-square fitting of the recorded lineshape with the minimum required number of peaks, each of which had four adjustable parameters, namely the amplitude, position, width and a ratio to specify the extent of the Gaussian/Lorentzian broadening. The intensity has been calculated from the area under all the peaks used for the deconvolution.

5.3. Theory and Results

5.3.1. “Skin Depth” Issue

The skin-depth, d, (14.7 μm) is almost an order of magnitude larger than the reported thickness of mossy or dendritic whiskers of 1-2 μm[7], and therefore the penetration of these structures can be assumed to be total. Thus, unlike the bulk, the signal from these Li microstructures is directly proportional to their volume or mass

(Figure 5.1, equations 5.7 and 5.12). As a result, the signal of the lithium microstructures can be readily separated from the signal of the bulk Li and their formation and growth can be readily monitored by using in-situ NMR spectroscopy. (N.b., the NMR method does not directly distinguish between the moss and the dendrites, and hence the term "microstructure" is used to cover both these morphologies). In the subsequent sections it is first confirmed that there is indeed a "skin-depth" problem for Li metal, and then demonstrate the application of a non-destructive *in situ* methodology to quantify dendritic/mossy lithium formation for cells containing lithium metal electrodes. Three cells are investigated, a $LiCoO_2$ - Li cell with a standard $LiPF_6$, ethylene carbonate (EC)/dimethylcarbonate (DMC) electrolyte, and then two symmetric Li-Li cells (i.e., cells with Li on both electrodes), but with two different ionic liquids with reportedly very different abilities to suppress dendrite growth[8,20-23]. $LiCoO_2$ – Li cells containing ionic liquids were not studied, since they suffer from significant capacity fade[24,25], presumably due to cobalt dissolution. The development of a theory to quantify amount of Li microstructure is described in the next section.

In order to demonstrate that the skin-depth issue is important in NMR studies of Li metal batteries, three samples were prepared by pressing together multiple stacked Li strips, each strip having a dimension of 11 x 4.5 mm, and a uniform thickness of 0.38mm, to generate samples with thicknesses 0.76, 1.14 and 1.52mm. These samples have volume ratios 2:3:4, and relative surface areas of approx 1: 1.08:1.18, A linear dependence of the NMR signal with respect to the area (rather than the volume) is clearly evident (Figure 5.2) validating our assertion that the NMR signal from the bulk electrode mostly originates from Li atoms near the surface. These observations are used to explore the morphology of the Li electrodes.

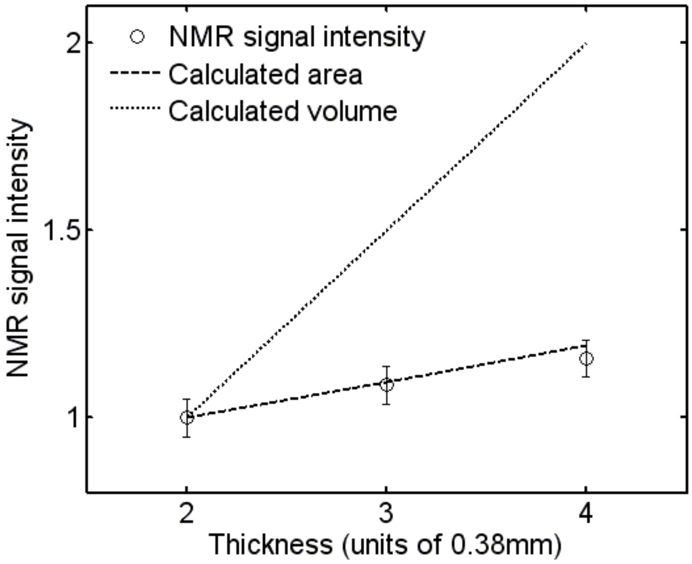

Figure 5.2. NMR signal intensities of multiple lithium strips of length and width, 11 x 4.5 mm. (normalized with respect to the thinnest strip). The calculated area (dashed line) and the volume (dotted line) of the lithium metal are also shown. A linear dependence of signal intensity with lithium metal area is clearly evident.

5.3.2. Theory Used to Quantify the NMR Signals of Metals

For rf field of strength ω_1, the field strength inside a metal ($\omega(x)$), at a depth x from surface is given by,

$$\omega(x) = \omega_1 e^{-\frac{x}{d}}. \qquad [5.2]$$

where, d is the skin depth as defined in equation 5.2. For direct excitation NMR experiments, the NMR signal intensity (S) depends on the product of the strength of the applied rf (ω_1) and duration of the rf pulse (τ_p), via, $S \propto \omega_1 \tau_p$, where τ_p is chosen to satisfy $\omega_1 \tau_p = \pi / 2$ in order to maximize the signal response. Since, inside a metal, the rf strength decreases as a function of the depth, ω_1 is replaced by $\omega(x)$ to write, $S \propto \int_0^\infty \sin(\omega(x)\tau_p)dx$ with $\omega(0) = \omega_1$. In the case of a typical metal electrode, the thickness of the metal (c) is far greater than the skin depth, and hence the upper limit of the integral can be set to infinity. The NMR signal from the entire volume of the metal, S_{bulk} is,

$$S_{bulk} = s_o A \int_0^c \sin(\omega(x)\tau_p)dx \cong s_o A \int_0^\infty \sin(\omega(x)\tau_p)dx \qquad [5.3]$$

where A is the total surface area of the metal block and s_o is the signal per unit volume of the metal. For $\omega(0)\tau_p = \omega_1\tau_p = \pi / 2$ (i.e, when a π/2 pulse is used to excite the signal), and using equation 5.2 to obtain from the above integration,

$$S_{bulk} = 1.3708\, d\, A s_o \qquad [5.4]$$

where, S_{bulk} is the NMR signal from a metal block. For a metal block of length a, width b, and thickness c, $A = 2(ab + bc + ca)$ and the NMR signal intensity can be written as,

$$S_{bulk} = 1.3708\, d\, \{2ab + 2(a+b)c\} s_o \qquad [5.5]$$

To further simplify calculations it is assumed that the lithium metal electrode has only two types of morphologies, (i) bulk metal having a thickness far greater than skin depth, (ii) micro-structures on the surface of the electrode, with a thickness that is much smaller than the skin depth (i.e., the rf penetration of the dendritic whiskers is total). It is also assumed that the metal electrode prior to electrochemical cycling has negligible micro-structure. If the total volume of the lithium micro-structure is $V_\mu(t)$, then the NMR signal from the micro-structure ($S_\mu(t)$) can be written as

$$S_\mu(t) = V_\mu(t) s_o \qquad [5.6]$$

and therefore, it can be written from equation 5.5,

$$S = S_m + V_\mu s_o = s_o(V_{eff} + V_\mu) = s_o(1.3708\, d\, A + V_\mu) \qquad [5.7]$$

The mass of lithium deposited at or stripped from ($M_{Li}(t)$) the metal lithium electrode can readily extracted from the electrochemical data:

$$M_{Li}(t) = C\, m_{Li} \int_0^t I_c(t)\, dt \qquad [5.8]$$

where, m_{Li} is the mass of a lithium atom, *C* is number of electrons per Coulomb, and $I_c(t)$ is the current at time *t*. It is assumed that there is 100% Coulombic efficiency, i.e, the loss of lithium due to the formation of a SEI or another side reaction is negligible.

Note that since a typical discharge process results in stripping of lithium ions from the lithium electrode under a negative value of current, the calculated mass could be negative in sign; i.e., the negative sign indicates a loss of observable mass from the electrode.

Supposing that the total mass deposited or stripped from the lithium electrode can be written as,

$$M_{Li}(t) = M_{SD}(t) + M_{\mu}(t) \qquad [5.9]$$

where, M_{SD} is the mass of smoothly deposited or stripped metal and M_{μ} is the mass of the micro-structure (mossy or dendritic lithium). If smooth deposition or stripping results in a change of thickness of the metal by an amount $c_d(t)$,

$$M_{SD}(t) = \rho_{Li}\, a\, b\, c_d(t) \qquad [5.10]$$

and assuming the volume of the micro-structure is $V_{\mu}(t)$,

$$M_{\mu}(t) = \rho_{Li} V_{\mu}(t) \qquad [5.11]$$

where, ρ_{Li} is the density of the lithium metal. Thus from equations 5.9, 5.10 and 5.11,

$$M_{Li}(t) = \rho_{Li}\, a\, b\, c_d(t) + \rho_{Li}\, V_{\mu}(t). \qquad [5.12]$$

From equations 5.5 and 5.6, the total NMR signal originating from the bulk metal and the micro structures can be written as (where the original thickness of the metal electrode, that is the thickness before the stripping or deposition, is, c_o),

$$S(t) = S_{bulk}(t) + S_{\mu}(t) = 1.3708\, d\,\{2ab + 2(a+b)(c_o + c_d(t))\}s_o + V_{\mu}(t)s_o \qquad [5.13]$$

The fractional change of NMR signal intensity *I(t)* is denoted as,

$$I(t) = \frac{S(t) - S(0)}{S(0)} = \frac{2(a+b)c_d(t)}{A_o} + \frac{V_\mu(t)}{1.3708\, d\, A_o} \qquad [5.14]$$

where, $A_o = 2ab + 2(a+b)c_o$, is the area of the metal electrode before electrochemical cycling.

For comparison, the dimensionless parameter *I(t)* for two extreme cases is calculated, (i) there is a smooth deposition or stripping ($I_{SD}(t)$) and (ii) when all deposition or stripping results in microstructures ($I_\mu(t)$). For these two cases, from equations 5.9, 5.10, 5.11 and 5.14,

$$I_{SD}(t) = \frac{2(a+b)M_{Li}(t)}{A_o \rho_{Li}\, ab} \qquad [5.15]$$

and,

$$I_\mu(t) = \frac{M_{Li}(t)}{1.3708 d\, A_o\, \rho_{Li}} \qquad [5.16]$$

It is noted that the right hand sides of equations 5.16 and 5.17 are expressed in terms of known or experimentally measured quantities.

Since, all parameters except $c_d(t)$ and $V_\mu(t)$ in the equations 5.13 and 5.14 are either known or can be measured experimentally, one can solve these two equations to calculate $c_d(t)$ and $V_\mu(t)$, and subsequently, by using equations 8-10, the masses $M_{SD}(t)$ and $M_\mu(t)$ can be calculated. Thus, the volume $V_\mu(t)$ and the mass $M_\mu(t)$ of the micro-structures formed during the electrochemical cycling can be estimated from the following experimental parameters: the intensities of the metallic Li NMR resonances (i) originating from the moss and lithium metal electrode during electrochemical cycling $S(t)$, and (ii) at the beginning of the in-situ experiments $S(0)$, i.e., in the pristine state, assuming no micro-structures have formed yet, (iii) the geometry of the lithium metal electrode (length *a*, width *b*, and thickness c_o). Other parameters such as the skin depth (*d*) and the density of the lithium metal ($\rho_{Li} = 0.54\,\mathrm{g\,cm^{-3}}$) are either known [18] or can be calculated as discussed earlier. It is important to note that the method discussed above does not require the NMR peaks originating from the bulk of the lithium electrode and the moss to be well resolved.

In order to confirm that the skin-depth must be taken into account, appropriate expressions under the assumption that there is *no* skin-depth problem (in other words the extent of rf penetration is total for both the bulk metal and the micro-structures) are also derived. A dimensionless parameter $I_{vol}(t)$ is defined, which corresponds to the NMR signal intensity in a system where the signal is directly proportional to the volume (and thus mass) of the material; this can be calculated in a similar manner to equations 5.13 or 5.14,

$$I_{vol}(t) = \frac{S(t) - S(0)}{S(0)} = \frac{M_{Li}(t)}{\rho_{Li}\, a\, b\, c_{\delta}}. \qquad [5.17]$$

The above formula can be compared with the experimentally measured values of $I_{expt}(t)$.

So far, the relevant expressions of NMR signal intensity originating from a single lithium metal electrode subjected to electrochemical cycling have been derived. It is also possible to consider a type of cell where both the electrodes are lithium metal strips (*a symmetric cell*). For a symmetric cell net transfer of mass of lithium from one electrode to the other at any given point of electrochemical cycling is zero, since the loss of mass from one electrode results in an equal gain of mass by the other electrode, that is, $M_{Li}(t) = 0$ (as before, it is assumed that the loss of lithium in forming the SEI is negligible). Therefore, in the absence of the skin depth issues NMR signal originating from a symmetric cell will remain constant during the electrochemical cycling. Also, smooth deposition/stripping processes at both electrodes will result in constant NMR signal since the change in thickness $c_d(t)$ will be equal and opposite in sign for both the electrodes. Hence it can be written for a symmetric cell,

$$M_{Li}(t) = I_{SD}(t) = I_{vol}(t) = 0. \qquad [5.18]$$

However equations 5.8-5.13 can still be applied for symmetric cells. From equation 5.10, $M_{\mu}(t) = -M_{SD}(t)$ is obtained, which represents the growth of lithium microstructure that occurs at the expense of the loss of smoothly deposited lithium. Note that the errors introduced by any loss of Li metal due to SEI formation or other side-reactions will lead to an underestimation of the extent of microstructure formation, in systems with *significant* SEI formation. However, SEI formation can be readily monitored in the *in situ* NMR experiment via the formation of diamagnetic Li^+ species with resonances close to 0 ppm. Thus, this effect can be easily corrected for by monitoring the evolution of the intensities of the lithium-NMR signals of the diamagnetic components, since these are directly related to the mass of these species. The total mass of lithium/Li^+ remains constant in the cell, and thus the sum, $M_{Li} + M_{SEI} + M_{electr.}$, where M_{SEI} and $M_{electr.}$ are the masses of lithium in the SEI and electrolyte, respectively, remains unchanged.

5.3.3. Analysis of the Li metal signal in a Li:Silicon Cell

Here the first change involves insertion of Li into silicon, and the loss of Li from the negative electrode (Chapter 3) [13]. However, the Li metal signal remains essentially unchanged on charging, consistent with smooth stripping from the bulk Li strip (Figure 5.3). On charge, however, a significant increase in Li metal signal occurs, so that the apparent Li mass after one cycle has increased noticeably, indicating that the Li electrode that is formed after one cycle is now mossy/dendritic. There is a large irreversible capacity loss in the 1st cycle, however, this has no effect on the phenomenon under investigation. The following 2nd discharge (not shown) continues by removal of primarily the mossy/dendritic lithium.

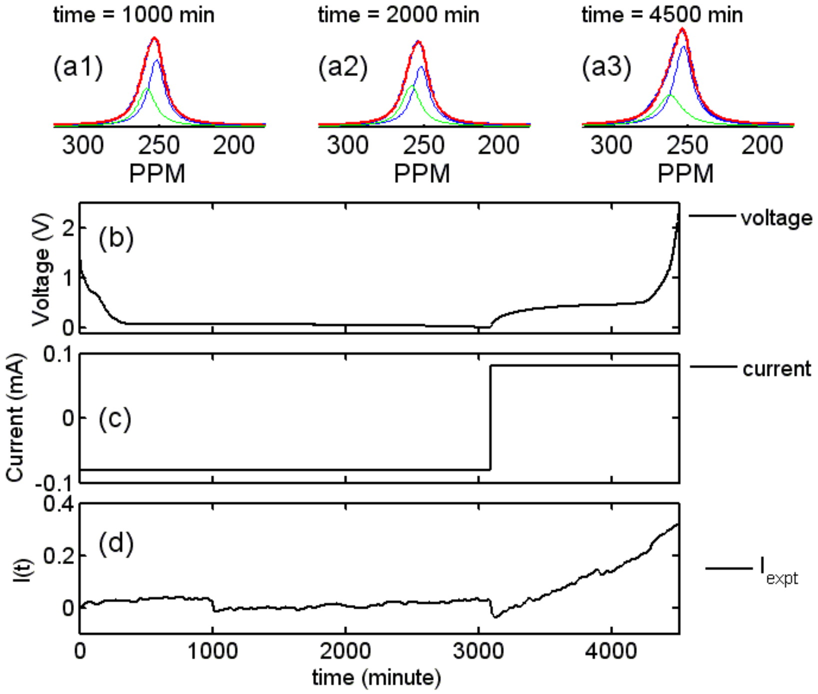

Figure 5.3. (a) Spectral snapshots of the ^{7}Li metal signal. (b-c) Current and voltage profiles. (d) Li signal intensity (fractional change, I_{expt}, normalized to the signal at the beginning). The Li intensity remains essentially constant during discharge (Li stripping). Since uniform stripping leaves the electrode area unchanged and the change in thickness is negligible, the signal remains virtually constant. The minor changes in the signal intensity during the 1st discharge are most likely due to the formation of pits which are smoothed out or removed as stripping continues.

5.3.4. Symmetrical and Full Cell Studies

Figures 5.4-6(a) show the ^{7}Li NMR spectra of three cells at different stages during electrochemical cycling, with applied current profiles and resulting cell potentials as plotted in Figures 5.4-6 (b) and (c). Only the spectral region near the Li metal is plotted. A resonance is seen at time, t = 0, at approximately 258 ppm for all the cells. The large shift of this Li metal resonance is caused by the Knight shift, which is a clear signature of a metal and a measure of the density of states (DOS) at the Fermi level at the Li nucleus (see Chapter 1) [26]. For the $LiCoO_2$ - Li battery, the growth and decay of the intensity of the Li metal NMR resonance, $I_{expt}(t)$, is almost linear (Figure 5.4d). The change in intensity of the Li signal was first analyzed by assuming that there are no skin-depth issues, (I_{vol} in Figure 5.4d) i.e., that the Li NMR intensity is directly proportional to the *mass* of Li deposited (or stripped), M_{Li} (where the mass can be calculated from the current passed through the cell). The experimental data clearly does not match with the calculated values of I_{vol}. Second, it is assumed that there was (a) a skin-depth problem, and (b) that all of the Li is deposited (and stipped) as a smooth Li deposit. Again, the calculated intensity, I_{SD}, does not fit the experimental data. In contrast, when it was assumed that the Li deposition involves the formation of microstructures only (i.e., Li mass that is completely observable by NMR), the curve (I_{μ}) is now very close to the experimental one suggesting there no longer appears to be a skin-effect; the rf signal penetrates the newly formed Li deposits. The best fit is achieved for deposition of approx. 90% of the Li metal as (dendritic/mossy) microstructures (M_{μ}), and approx. 10% as a smooth deposition (M_{SD}), on the Li electrode (Figure 5.4e). This calculation relies on I_{exp} and the total deposited mass M_{Li} (see theory section for relevant expressions). On discharge, a linear decay of the Li metal peak occurs, the fit to this decay indicating that essentially all of the micron-sized Li participates in the electrochemistry, at least in the 1st cycle, for a cell cycled at a low current density. Consistent data were observed on cycling a Li - Silicon (EC/DMC) cell[13] (see section 5.3.3). Now, however, the first change involves insertion of Li into silicon, and the loss of Li from the negative electrode. The Li metal signal remains essentially unchanged during the 1st charge of this cell, indicating that Li is stripped smoothly from the bulk Li strip. By contrast, on discharge a significant increase in Li metal signal occurs, so that the apparent Li mass after one cycle has increased noticeably, indicating that the Li electrode that is formed after one cycle vs. Si is now mossy/dendritic.

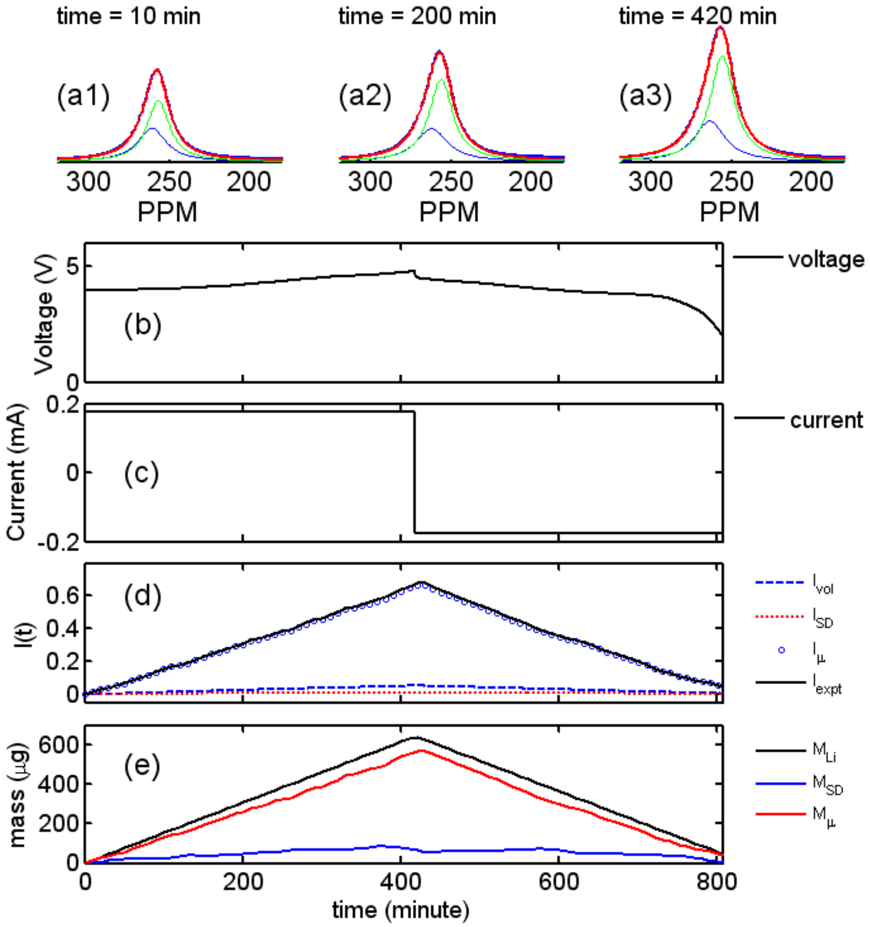

Figure 5.4. Deconvoluted ^{7}Li NMR spectra of metallic lithium (a 1-3), as a function of time for a "desert-rose" $LiCoO_2$ cell, for one charge-discharge cycle. Time, t = 420 minutes represents the top of charge. The deconvoluted peaks used to the fit the NMR data are indicated with thin red, blue and green lines, in this and the subsequent two figures. The thick red and blue line (almost invisible under the red line), shows the fit and the experimental spectra respectively. The measured voltage and the applied current (corresponding to a C/10 rate) are plotted in (b) and (c). The measured Li metal intensity ($I_{exp}(t)$) is shown as a solid black line in (d), where the signal (S(t)) has been normalized to the signal at t=0, to give $I_{exp}(t) = [S(t)-S(t=0)]/S(t = 0))$. Theoretical values of I(t), calculated under various assumptions are shown for comparison: (i) no skin depth issues $I_{vol}(t)$ (blue dashed line; equation 5.18), (ii) all of lithium is smoothly deposited $I_{SD}(t)$ (red dotted line; equation 5.16), (iii) all of lithium deposited/stripped forms micro-structure $I_{\mu}(t)$ (blue circles; equation 5.17). Only $I_{\mu}(t)$ provides a good fit to the experimental data, the small deviation being due to a small amount of smoothly deposited lithium. $I_{exp}(t)$ in combination with total mass of Li deposited or stripped $M_{Li}(t)$ (extracted from the electrochemistry), can be used to calculate the mass of deposited Li, $M_{SD}(t)$ and Li microstructures $M_{\mu}(t)$, taking into account of the skin-depth problem (e) (equations 5.11 and 5.12).

The accumulation of Li microstructures can be seen even more clearly in experiments performed with symmetric Li-metal cells, because the total mass of Li (M_{Li}) remains constant during electrochemical cycling (stripping from one electrode results in deposition on the other electrode), and thus any change in Li metal intensity must be due to microstructure formation (i.e., a morphological change which keeps the volume constant and yet changes the surface area). In the first experiment (Figure 4), an ionic liquid based electrolyte (1-ethyl-3-methylimidazolium tetrafluoroborate (C_2mim BF_4 + 0.5 mol.kg^{-1} $LiBF_4$)) was used which has been shown to be ineffective in suppressing the formation of Li dendrites[21] , but whose performance can be improved somewhat by the addition of vinylene carbonate (VC), allowing cells to be cycled for a limited number of times[20]. On cycling with a constant current density, the Li signal remains constant for the first few cycles, indicating that Li is deposited as a smooth film, but then after 220 mins (6 cycles), the Li signal grows steadily indicating that Li microstructures are forming (figure 5.5d). An almost monotonic growth is seen, which is then followed by the degradation of electrochemical performance and a short circuit is observed after 500 minutes. This is consistent with earlier optical microscopy studies (e.g., of Li cells containing 1M $LiPF_6$ in propylene carbonate, PC), which show that the electrical effects of the mossing (i.e., short-circuits) appear after the optical images show significant growth of Li dendritic structures[27].

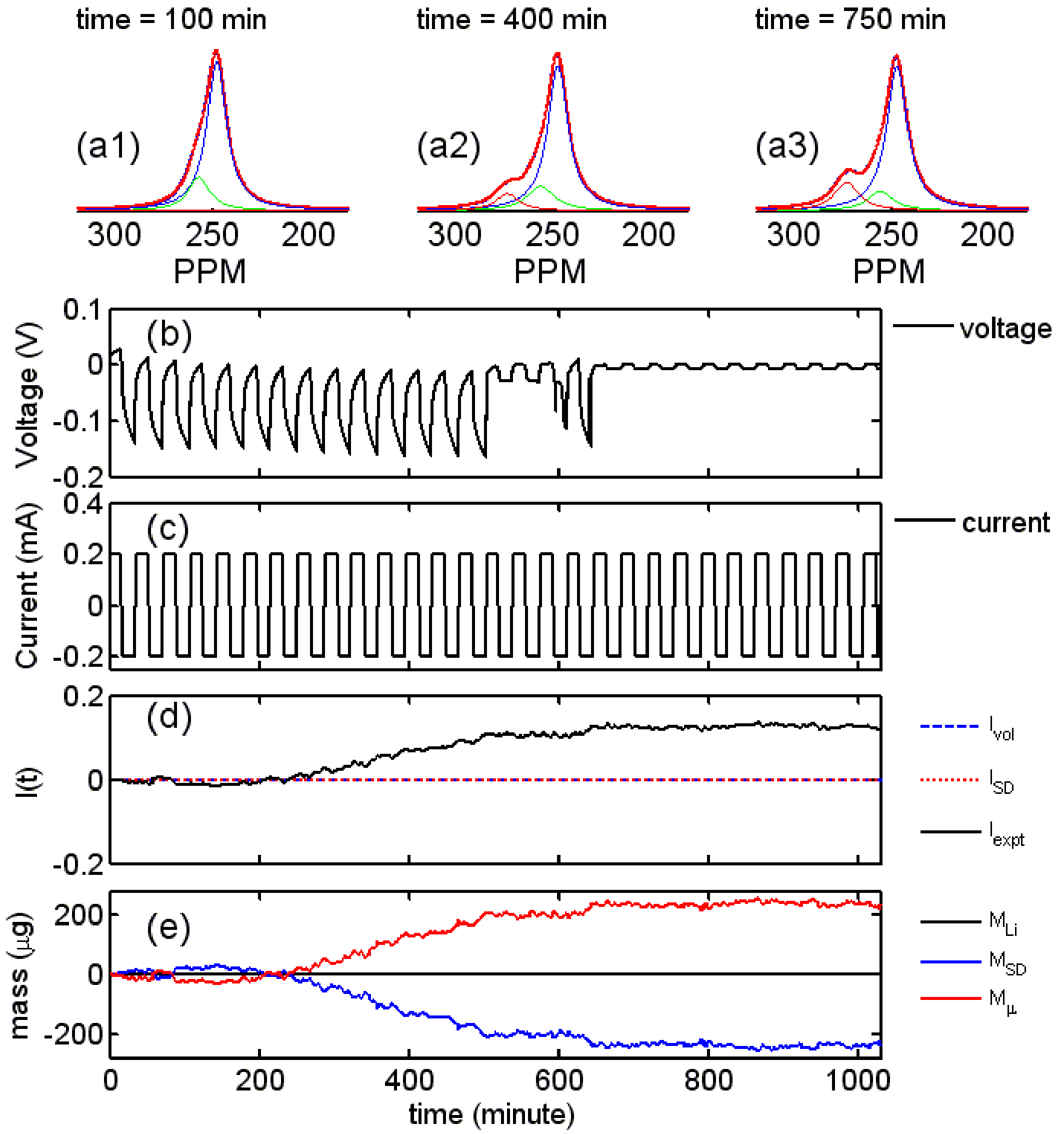

Figure 5.5. Deconvoluted ^{7}Li NMR spectra of metallic lithium (a 1-3) for the symmetric cell with electrolyte C_2MIm BF_4 + $LiBF_4$ + VC. Multiple (>28) charge-discharge cycles are shown. (b,c) measured voltage and the applied current during the electrochemical cycling. (d) Calculated and experimental values of I(t) (the definitions are given in the caption to Figure 3 and in the text). I_{vol}, is hidden under the I_{SD} curve (red dashed line). (e) I_{expt} was then used to calculate the M_{μ}(t) and M_{SD}(t), (with equations 5.11 and 5.12), M_{Li} (black line) remaining constant. The growth of the microstructure occurs before the degradation of the cell performance (as seen by the erratic voltage profile). The mutually opposite behavior of M_{μ}(t) and M_{SD}(t) reflects the fact that micro structures form at the expense of the smoothly deposited lithium.

Interestingly the growth of the Li signal is also associated with the observation of a second Li metal peak at approximately 270 ppm, and three peaks are required to fit the spectrum. In contrast, the Li metal resonances of the other two cells (Figures 5.4(a) and 5.6(a)) can be adequately fit by using a main resonance and a second, weaker peak to account for the shoulder. This additional resonance, with a shift that is different from that of bulk Li, is observed in many of our *in situ* NMR experiments (including experiments with $LiCoO_2$-Li cells), and has also been reported by Gerald *et al.* [16]; it is assigned to the mossy / dendritic Li. In contrast to Gerald *et al.,* who ascribed this effect to differences in the DOS of the dendrites *vs.* the bulk metal, it is proposed that the major contribution to the shift differences arises from the magnetic susceptibility of the lithium metal electrode, which displays temperature independent paramagnetism (TIP)[17]. Any material, when placed in a static magnetic field, will be magnetized giving rise to an internal field; in the case of a paramagnetic material the internal field will align with the external field, the field varying across material in a way that depends on the shape and packing of the particles that comprise the material, and the *orientation* of the sample with respect to the field, giving rise to bulk magnetic susceptibility (BMS) effects[28]. This proposal was tested in a separate experiment by exploring the effect of the orientation of the Li electrode with respect to the magnetic field on the Li shift (Figure 5.7). The largest and smallest shifts are seen when the Li foil is oriented parallel and perpendicular to field, respectively. In batteries with “mossy-Li” resonances such as those shown in Figure 5.5a, upon rotation of the cell by 90º, the “mossy-Li” resonance was observed at lower frequencies than the main Li metal resonance; at close to the “magic-angle” (54.7º), the signals could not be resolved (spectra not shown), again indicating that this is a BMS effect, the orientational dependence arising from the ($3\cos^2\theta$ -1), (θ is the orientation with respect to the applied field) i.e., second-rank tensorial dependence, of the bulk magnetic interactions. Such effects are long-range (tens of micrometer) and hence they are likely to affect the NMR shift of the dendrites as well as that of the surface signal of the bulk metal of the electrode. Thus it is ascribed to the peak asymmetry of the Li metal resonance, and the observation of the additional resonance, to different internal magnetic fields felt by different parts of the sample. The internal magnetic fields felt by the dendrites and moss may be quite different from those of the bulk Li metal foil, and will depend on the distance of the dendrite/moss from the foil and also the nature of the microstructure (e.g., the Li electrode in the $LiCoO_2$/Li EC/DMC cell contains mossy Li but does not show additional resonances (Figure 5.4a)). The work is currently in process to develop models to correlate microstructures with the observed BMS effects. However, since such susceptibility effects do not affect our intensity calculations, any further exploration of these effects is beyond the scope of the work presented here.

The third cell (Figure 5.6) contains 1-butyl-methylpyrrolidinium bis(trifluoromethanesulfonyl)imide (C_4mpyr TFSI) + LiTFSI, which has been shown to suppress dendrite formation and can be cycled up to a current density of 1.25 mA.cm^{-1} [9]. Now, no growth of the Li microstructures is observed, even for very high currents: cycling the cell up to 0.5 mA.cm^{-1} results in uniform lithium plating and stripping. At the highest current used (~ 0.5 mA cm^{-1}) surprisingly a decrease in the total Li mass is seen, which is ascribed to the heating effects associated with these large currents and voltages, but it may also be associated with the surfaces of the electrodes becoming smoother. This may occur because the initial Li foil is not perfectly smooth, since the brushing procedure used to remove native impurities (oxides, carbonates, etc.) from the metal may result in a roughened surface[13].

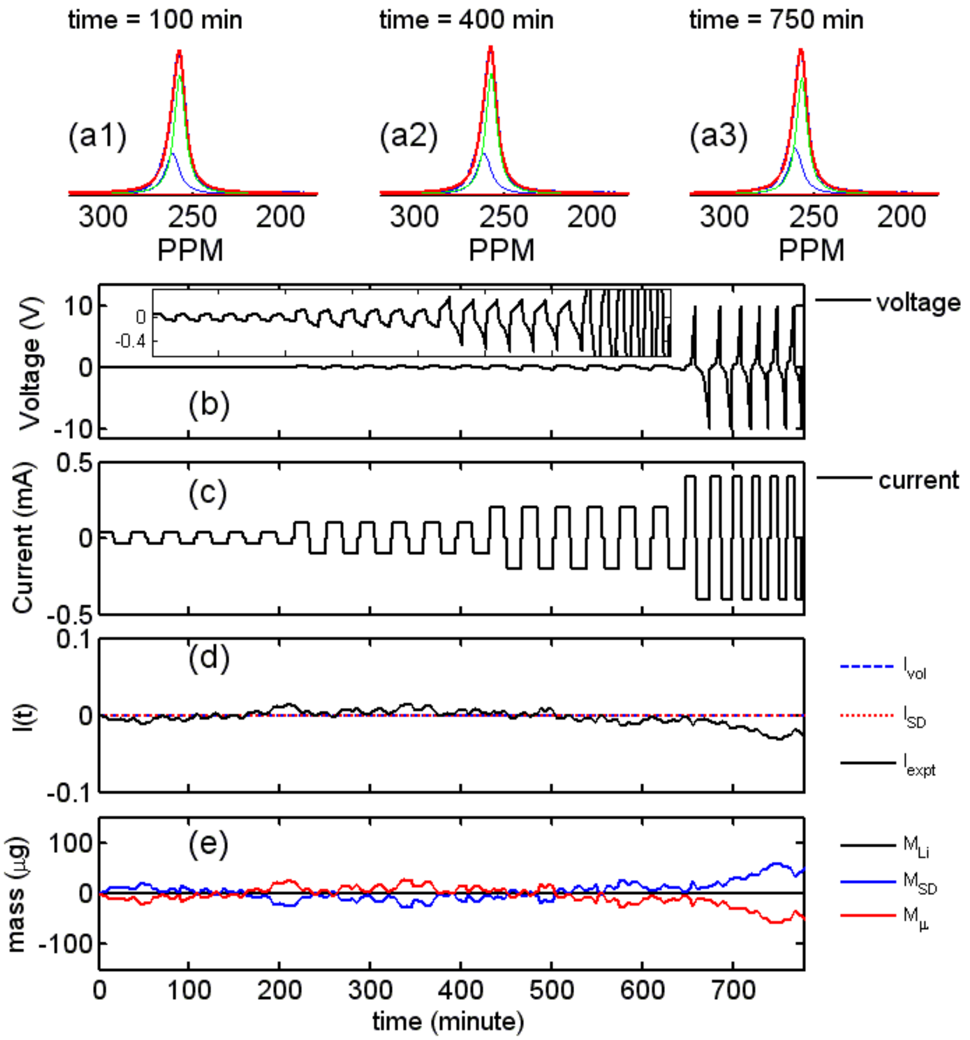

Figure 5.6. Deconvoluted spectra of metallic lithium (a1-3), and measured voltage and the applied current during the electrochemical cycling (b-c) of a symmetric cell with the electrolyte C_4mpyr TFSI + LiTFSI. The inset in (b) shows enlargement of part of the potential curve. 6 cycles are performed with a current of 0.1 mA cm^{-1} followed by 6 cycles with 0.25 mA cm^{-1} and finally 6 cycles with 0.5 mA cm^{-1} (effective Li surface area is 0.4 cm^{2}). (d) Calculated and experimental values of I(t) (see text and Figure 3 for definitions). I_{vol}, is hidden under the I_{SD} curve (red dashed line). (e) The corresponding values of M_{μ}(t) and M_{SD}(t), M_{Li}.

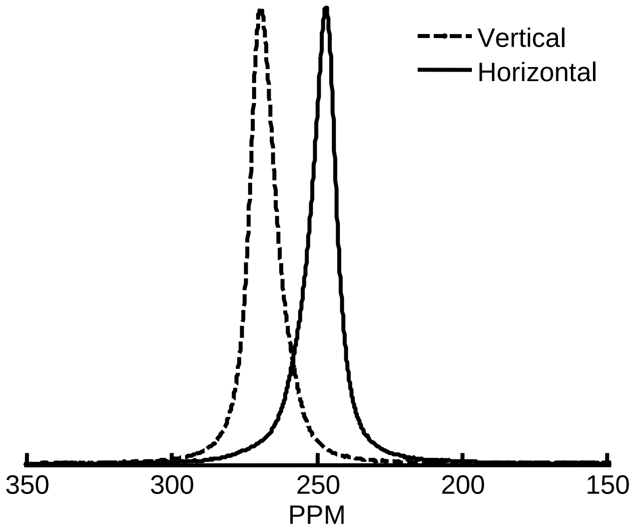

Figure 5.7. ^{7}Li NMR spectra of lithium electrode of a pristine symmetric cell (composed of two rectangular strips of size 4mm x 8mm x 0.38mm with a 1 mm separator between them) at different orientations with respect to the magnetic field. The dashed and solid lines shows the spectrum recorded when the plane of the strip was oriented parallel to the magnetic field (“vertical”) and perpendicular to the magnetic field (“horizontal”), respectively. The asymmetric lineshape of the resonance and its field-orientation dependence is attributed to the bulk magnetic susceptibility (BMS) effects of the lithium metal strip.

In general, the initial cycles of a battery result in the growth of a stable Solid Electrolyte Interphase (SEI) which is important for stable cycling of a lithium metal electrode within a battery. In the case of the C_2MIm BF_4 + $LiBF_4$ + VC electrolyte, VC is required to form a stable SEI layer[20-22]. However, as the lithium electrode is cycled, the VC is continuously consumed by side reactions finally leading the electrode to become dendritic[20], as clearly observed here by NMR, (growth of Li-metal signal intensity after 6 cycles, Figure 5.5d). In contrast, the C_4mpyr TFSI + LiTFSI electrolyte can form a stable SEI by itself leading to stable cycling up to a current density of 1.25 mA.cm^{-1} [8,23] and 0.5 mA.cm^{-1} in this work.

The method used here to analyze the data assumes that the metal electrode surface can be described as a combination of a smooth film and microstructures having dimensions much smaller than the skin depth of 14.7 µm. *i.e.*, the technique is sensitive to dendrites/moss of a few microns in thickness. If much thicker dendritic structures of

10 – 100 μm form, it becomes difficult to separate these from the bulk electrode. However, one simple way to quantify the distribution in sizes of the dendritic/mossy structures is perform the experiments at various magnetic fields (with both ^{6}Li and ^{7}Li NMR), so as to vary the skin-depth. For example, ^{6}Li with a Larmor frequency of 29.4 MHz at a field strength of 4.7 T has a skin depth of 23.9 μm, while ^{7}Li at a field strength of 14.1 T (corresponding to a ^{1}H Larmor frequency of 600 MHz) has a skin depth of only 8.4 μm, the former experiment detecting both thin and thicker microstructures, the latter only thinner microstructures. It is also assumed that SEI formation is negligible; the formation of a significant SEI film can, however, be readily monitored by *in situ* NMR and its effect can be corrected for.

5.4. Conclusions

In conclusion, it is shown that NMR spectroscopy performed *in-situ* in conjunction with electrochemical cycling is capable of dynamically monitoring the growth and stripping of lithium microstructures. Using simple calculations based on the skin-depth of metallic structures under radiofrequency excitations, it is shown that that it is possible to quantify the amount of moss/dendritic Li formed. Assuming that the total surface area of the bulk metal electrode does not change significantly under electrochemical cycling of the cells, the change in the intensity of the Li metal signal can be attributed to the formation or the stripping of mossy/dendritic Lithium. The potential of the approach is demonstrated by comparing the ability of two different ionic liquid electrolytes to prevent dendrite formation. The sensitivity of this technique means that this is a simple and accurate method for monitoring the early stages of dendrite formation in lithium batteries. For example, in the development of batteries with metallic lithium anodes, this means that the whole range of factors that might be used to control or eliminate the formation of dendrites can now be readily assessed and implemented with much more rigour than previously possible. In a short time, this should allow researchers to quantify the efficacy of strategies currently employed (e.g., electrolyte additives, pulsed charging schemes). In studies of other anodes (e.g., carbon, silicon etc.,) the method will allow the effect of state of charge and rate on lithium deposition to be explored. Extensions of the NMR approach to investigate a wider range of metallic systems, including electrochemical pitting, the investigation of micro fissures and cracks on small metal surfaces and the sintering of metal nanoparticles in catalytic or fuel-cell applications can also be envisaged.

5.5. References

(1) Armand, M.; Tarascon, J. M. *Nature (London, U. K.)* **2008**, *451*, 652.

(2) Tarascon, J. M.; Armand, M. *Nature* **2001**, *414*, 359.

(3) Epelboin, I.; Froment, M.; Garreau, M.; Thevenin, J.; Warin, D. *Proc. - Electrochem. Soc.* **1980**, *80-4*, 417.

(4) Sannier, L.; Bouchet, R.; Grugeon, S.; Naudin, E.; Vidal, E.; Tarascon, J. M. *J. Power Sources* **2005**, *144*, 231.

(5) Wang, C.; Wang, D. L.; Dai, C. S. *Journal of the Electrochemical Society* **2008**, *155*, A390.

(6) Xu, J. Q.; Yang, J.; NuLi, Y.; Wang, J. L.; Zhang, Z. S. *Journal of Power Sources* **2006**, *160*, 621.

(7) Orsini, F.; Du Pasquier, A.; Beaudoin, B.; Tarascon, J. M.; Trentin, M.; Langenhuizen, N.; De Beer, E.; Notten, P. *J. Power Sources* **1998**, *76*, 19.

(8) Saint, J.; Best, A. S.; Hollenkamp, A. F.; Kerr, J.; Shin, J. H.; Doeff, M. M. *J. Electrochem. Soc.* **2008**, *155*, A172.

(9) Howlett, P. C.; MacFarlane, D. R.; Hollenkamp, A. F. *Electrochemical and Solid State Letters* **2004**, *7*, A97.

(10) Yamaki, J.; Tobishima, S.; Hayashi, K.; Saito, K.; Nemoto, Y.; Arakawa, M. *Journal of Power Sources* **1998**, *74*, 219.

(11) Monroe, C.; Newman, J. *Journal of the Electrochemical Society* **2003**, *150*, A1377.

(12) Chazalviel, J. N. *Phys. Rev. A* **1990**, *42*, 7355.

(13) Key, B.; Bhattacharyya, R.; Morcrette, M.; Seznec, V.; Tarascon, J. M.; Grey, C. P. *Journal of the American Chemical Society* **2009**, *131*, 9239.

(14) Chevallier, F.; Letellier, M.; Morcrette, M.; Tarascon, J. M.; Frackowiak, E.; Rouzaud, J. N.; Beguin, F. *Electrochem. Solid-State Lett.* **2003**, *6*, A225.

(15) Letellier, M.; Chevallier, F.; Morcrette, M. *Carbon* **2007**, *45*, 1025.

(16) Gerald, R. E.; Klingler, R. J.; Sandi, G.; Johnson, C. S.; Scanlon, L. G.; Rathke, J. W. *J. Power Sources* **2000**, *89*, 237.

(17) Kittel, C. *Introduction to Solid State Physics. 5th Ed*, 1976.

(18) Lide, D. R.; Frederikse, H. P. R. *CRC Handbook of Chemistry and Physics, 78th Edition*, 1997.

(19) Chen, H.; Grey, C. P. *Adv. Mater. (Weinheim, Ger.)* **2008**, *20*, 2206.

(20) Lane, G. H.; Best, A. S.; MacFarlane, D. R.; Forsyth, M.; Hollenkamp, A. F. *Electrochimica Acta*, *In Press, Corrected Proof*.

(21) Egashira, M.; Kiyabu, T.; Watanabe, I.; Okada, S.; Yamaki, J. *Electrochemistry* **2003**, *71*, 1114.

(22) Sivakkumar, S. R.; MacFarlane, D. R.; Forsyth, M.; Kim, D. W. *Journal of the Electrochemical Society* **2007**, *154*, A834.

(23) Bhatt, A. I.; Best, A. S.; Huang, J. H.; Hollenkamp, A. F. *Journal of the Electrochemical Society* **2010**, *157*, A66.

(24) Seki, S.; Kobayashi, Y.; Miyashiro, H.; Ohno, Y.; Mita, Y.; Usami, A.; Terada, N.; Watanabe, M. *Electrochemical and Solid State Letters* **2005**, *8*, A577.

(25) Sakaebe, H.; Matsumoto, H. *Electrochemistry Communications* **2003**, *5*, 594.

(26) Slichter, C. P. *Principles of Magnetic Resonance. 2nd Ed*, 1978.

(27) Howlett, P. C.; MacFarlane, D. R.; Hollenkamp, A. F. *Journal of Power Sources* **2003**, *114*, 277.

(28) Kubo, A.; Spaniol, T. P.; Terao, T. *J. Magn. Reson.* **1998**, *133*, 330.

Chapter 6

Conclusions and Final Remarks

(De)lithiation mechanisms of micron-sized and nanoparticulate silicon have been studied for the first time in detail by identifying the long range and local structure of lithiated silicides and amorphous silicon obtained by electrochemical lithiation. This work is also the first detailed study to correlate the electrochemistry with the local structure. Additionally, a spontaneous reaction between the electrolyte and the fully lithiated silicon is identified by in-situ experiments. This reaction results in side reactions and capacity loss. The detailed mechanisms are expected to be instrumental in designing and building better electrodes for future commercial high capacity Li-ion batteries with silicon. Several examples can be given which originate from the results of this study such as:

- The side reactions that occur as early as the 1st discharge of silicon results in self-discharge and capacity loss as well as undesirable SEI build-up. This needs to be taken into account before a fast rate or a low voltage cut-off is selected for a silicon electrode.
- These side reactions are closely related to overall lithiation level of silicon and are more severe for fully lithiated silicon electrodes. A suitable capacity limit (for example, 2/3 of theoretical capacity) definitely needs to be employed for a silicon electrode to prevent capacity loss.
- The side reactions are also found to be an issue for nanoparticulate silicon lithiation.
- For subsequent discharge cycles of silicon, voltage cut-offs needs to be above 120 mV since below this limit, the amorphous phases transform into local Li-Si clusters with predominantly isolated Si which is identified as the most reactive and unstable form of local ordering.

- The 2nd process during the lithiation of amorphous silicon appears to be associated with the highest volume expansion during the overall lithiation and most drastic phase transformation from Si matrix to amorphous lithiated silicides which translates into severe particle-particle contact loss. This results in major capacity loss and can be also minimized by using voltage cut-offs at 120 mV or half the theoretical capacity.

The characterization work presented in this study can also help in better understanding the lithiation of similar systems and the way we think about amorphous lithiated systems. Additional characterization experiments utilizing complex NMR sequences can be envisaged to provide the specific bonding and distances in Li nearby Si-Si clusters and Li nearby isolated Si. These assignments can be confirmed by Neutron PDF experiments with Reverse Monte-Carlo type simulations. Such experiments are currently in progress.

Formation of metallic lithium microstructures (dendrites/moss/foam) is also investigated in this work by using in-situ static NMR for the first time on actual working lithium-ion batteries. A simple and quantitative method is introduced to evaluate the effectiveness of different electrode/electrolyte systems in suppressing unsafe dendridic metal formations. The method may have high impact on Li-metal battery research.

References

Chapter 1

(1) Tarascon, J. M.; Armand, M. *Nature* **2001**, *414*, 359.

(2) Obrovac, M. N.; Christensen, L. *Electrochem. Solid-State Lett.* **2004**, *7*, A93.

(3) Li, H.; Huang, X.; Chen, L.; Zhou, G.; Zhang, Z.; Yu, D.; Mo, Y. J.; Pei, N. *Solid State Ionics* **2000**, *135*, 181.

(4) Hatchard, T. D.; Dahn, J. R. *J. Electrochem. Soc.* **2004**, *151*, A838.

(5) Breger, J., *Ph.D. Thesis*, Stony Brook University, NY, 2006.

(6) Bruce, P. G. *Chemical Communications* **1997**, 1817.

(7) Megahed, S.; Scrosati, B. *Journal of Power Sources* **1994**, *51*, 79.

(8) Epelboin, I.; Froment, M.; Garreau, M.; Thevenin, J.; Warin, D. *Proc. - Electrochem. Soc.* **1980**, *80*, 417.

(9) Sannier, L.; Bouchet, R.; Grugeon, S.; Naudin, E.; Vidal, E.; Tarascon, J. M. *J. Power Sources* **2005**, *144*, 231.

(10) Wang, C.; Wang, D. L.; Dai, C. S. *Journal of the Electrochemical Society* **2008**, *155*, A390.

(11) Xu, J. Q.; Yang, J.; NuLi, Y.; Wang, J. L.; Zhang, Z. S. *Journal of Power Sources* **2006**, *160*, 621.

(12) Ogasawara, T.; Debart, A.; Holzapfel, M.; Novak, P.; Bruce, P. G. *Journal of the American Chemical Society* **2006**, *128*, 1390.

(13) Orsini, F.; Du Pasquier, A.; Beaudoin, B.; Tarascon, J. M.; Trentin, M.; Langenhuizen, N.; De Beer, E.; Notten, P. *J. Power Sources* **1998**, *76*, 19.

(14) Saint, J.; Best, A. S.; Hollenkamp, A. F.; Kerr, J.; Shin, J. H.; Doeff, M. M. *J. Electrochem. Soc.* **2008**, *155*, A172.

(15) Howlett, P. C.; MacFarlane, D. R.; Hollenkamp, A. F. *Electrochemical and Solid State Letters* **2004**, *7*, A97.

(16) Yamaki, J.; Tobishima, S.; Hayashi, K.; Saito, K.; Nemoto, Y.; Arakawa, M. *Journal of Power Sources* **1998**, *74*, 219.

(17) Monroe, C.; Newman, J. *Journal of the Electrochemical Society* **2003**, *150*, A1377.

(18) Chazalviel, J. N. *Phys. Rev. A* **1990**, *42*, 7355.

(19) Armand, M.; Touzain, P. *Materials Science and Engineering* **1977**, *31*, 319.

(20) Arico, A. S.; Bruce, P.; Scrosati, B.; Tarascon, J.-M.; van Schalkwijk, W. *Nat. Mater.* **2005**, *4*, 366.

(21) Xu, K. *Chem. Rev. (Washington, DC, U. S.)* **2004**, *104*, 4303.

(22) Yamaura, J.; Ozaki, Y.; Morita, A.; Ohta, A. *J. Power Sources* **1993**, *43*, 233.

(23) Mabuchi, A. *Tanso* **1994**, *165*, 298.

(24) Dahn, J. R.; Zheng, T.; Liu, Y.; Xue, J. S. *Science (Washington, D. C.)* **1995**, *270*, 590.

(25) Azuma, H.; Imoto, H.; Yamada, S.; Sekai, K. *Journal of Power Sources* **1999**, *81*, 1.

(26) Tirado, J. L. *Materials Science & Engineering R-Reports* **2003**, *40*, 103.

(27) Li, J.; Christensen, L.; Obrovac, M. N.; Hewitt, K. C.; Dahn, J. R. *J. Electrochem. Soc.* **2008**, *155*, A234.

(28) Hochgatterer, N. S.; Schweiger, M. R.; Koller, S.; Raimann, P. R.; Woehrle, T.; Wurm, C.; Winter, M. *Electrochem. Solid-State Lett.* **2008**, *11*, A76.

(29) Obrovac, M. N.; Krause, L. J. *J. Electrochem. Soc.* **2007**, *154*, A103.

(30) Limthongkul, P.; Jang, Y.-I.; Dudney, N. J.; Chiang, Y.-M. *J. Power Sources* **2003**, *119-121*, 604.

(31) Chan, C. K.; Peng, H.; Liu, G.; McIlwrath, K.; Zhang, X. F.; Huggins, R. A.; Cui, Y. *Nat. Nanotechnol.* **2008**, *3*, 31.

(32) Holzapfel, M.; Buqa, H.; Hardwick, L. J.; Hahn, M.; Wuersig, A.; Scheifele, W.; Novak, P.; Koetz, R.; Veit, C.; Petrat, F.-M. *Electrochim. Acta* **2006**, *52*, 973.

(33) Nesper, R.; Von Schnering, H. G.; Curda, J. *Chem. Ber.* **1986**, *119*, 3576.

(34) Nesper, R.; Von Schnering, H. G. *J. Solid State Chem.* **1987**, *70*, 48.

(35) Nesper, R. *Prog. Solid State Chem.* **1990**, *20*, 1.

(36) Frank, U.; Mueller, W.; Schaefer, H. *Z. Naturforsch., Teil B* **1975**, *30B*, 10.

(37) Klemm, W.; Struck, M. *Z. Anorg. Allg. Chem.* **1955**, *278*, 117.

(38) Stearns, L. A.; Gryko, J.; Diefenbacher, J.; Ramachandran, G. K.; McMillan, P. F. *Journal of Solid State Chemistry* **2003**, *173*, 251.

(39) Grey, C. P.; Lee, Y. J. *Solid State Sciences* **2003**, *5*, 883.

(40) Lee, Y. J.; Grey, C. P. *Journal of Physical Chemistry B* **2002**, *106*, 3576.

(41) Grey, C. P.; Dupre, N. *Chem. Rev. (Washington, DC, U. S.)* **2004**, *104*, 4493.

(42) MacKenzie, K. J. D. *Multinuclear Solid-State Nuclear Magnetic Resonance of Inorganic Materials*, 2002.

(43) Key, B.; Bhattacharyya, R.; Morcrette, M.; Seznec, V.; Tarascon, J. M.; Grey, C. P. *Journal of the American Chemical Society* **2009**, *131*, 9239.

(44) Gerald, R. E.; Klingler, R. J.; Sandi, G.; Johnson, C. S.; Scanlon, L. G.; Rathke, J. W. *J. Power Sources* **2000**, *89*, 237.

(45) Chevallier, F.; Letellier, M.; Morcrette, M.; Tarascon, J. M.; Frackowiak, E.; Rouzaud, J. N.; Beguin, F. *Electrochem. Solid-State Lett.* **2003**, *6*, A225.

(46) Letellier, M.; Chevallier, F.; Morcrette, M. *Carbon* **2007**, *45*, 1025.

(47) Rietveld, H. M. *Journal of Applied Crystallography* **1969**, *2*, 65.

(48) Young, R. A.; Prince, E.; Sparks, R. A. *Journal of Applied Crystallography* **1982**, *15*, 357.

(49) Caglioti, G.; Paoletti, A.; Ricci, F. P. *Nuclear Instruments & Methods* **1958**, *3*, 223.

(50) Thompson, P.; Cox, D. E.; Hastings, J. B. *Journal of Applied Crystallography* **1987**, *20*, 79.

(51) Howard, C. J. *Journal of Applied Crystallography* **1982**, *15*, 615.

(52) Finger, L. W.; Cox, D. E.; Jephcoat, A. P. *Journal of Applied Crystallography* **1994**, *27*, 892.

(53) Stephens, P. W. *Journal of Applied Crystallography* **1999**, *32*, 281.

(54) McCusker, L. B.; Von Dreele, R. B.; Cox, D. E.; Louer, D.; Scardi, P. *Journal of Applied Crystallography* **1999**, *32*, 36.

(55) Egami, T. *Materials Transactions* **1990**, *31*, 163.

(56) Breger, J.; Dupre, N.; Chupas, P. J.; Lee, P. L.; Proffen, T.; Parise, J. B.; Grey, C. P. *Journal of the American Chemical Society* **2005**, *127*, 7529.

(57) Chupas, P. J.; Qiu, X. Y.; Hanson, J. C.; Lee, P. L.; Grey, C. P.; Billinge, S. J. L. *Journal of Applied Crystallography* **2003**, *36*, 1342.

(58) Chupas, P. J.; *Ph.D. Thesis*, Stony Brook University, NY, 2003.

(59) Egami, T.; Billinge, S. J. L.; *Underneath the Bragg Peaks: Structural Analysis of Complex Materials*, 2003.

Chapter 2

(1) Nesper, R.; Von Schnering, H. G. *J. Solid State Chem.* **1987**, *70*, 48.

(2) Nesper, R.; Von Schnering, H. G.; Curda, J. *Chem. Ber.* **1986**, *119*, 3576.

(3) Nesper, R. *Prog. Solid State Chem.* **1990**, *20*, 1.

(4) Frank, U.; Mueller, W.; Schaefer, H. *Z. Naturforsch., Teil B* **1975**, *30B*, 10.

(5) Klemm, W.; Struck, M. *Z. Anorg. Allg. Chem.* **1955**, *278*, 117.

(6) Stearns, L. A.; Gryko, J.; Diefenbacher, J.; Ramachandran, G. K.; McMillan, P. F. *Journal of Solid State Chemistry* **2003**, *173*, 251.

(7) Obrovac, M. N.; Christensen, L. *Electrochem. Solid-State Lett.* **2004**, *7*, A93.

(8) Morcrette, M.; Chabre, Y.; Vaughan, G.; Amatucci, G.; Leriche, J. B.; Patoux, S.; Masquelier, C.; Tarascon, J. M. *Electrochim. Acta* **2002**, *47*, 3137.

(9) Qiu, X.; Thompson, J. W.; Billinge, S. J. L. *J. Appl. Crystallogr.* **2004**, *37*, 678.

(10) Farrow, C. L.; Juhas, P.; Liu, J. W.; Bryndin, D.; Bozin, E. S.; Bloch, J.; Proffen, T.; Billinge, S. J. L. *J. Phys. Condens. Matter* **2007**, *19*, 335219/1.

(11) Key, B.; Bhattacharyya, R.; Morcrette, M.; Seznec, V.; Tarascon, J. M.; Grey, C. P. *Journal of the American Chemical Society* **2009**, *131*, 9239.

Chapter 3

(1) Obrovac, M. N.; Christensen, L. *Electrochem. Solid-State Lett.* **2004**, *7*, A93.

(2) Obrovac, M. N.; Krause, L. J. *J. Electrochem. Soc.* **2007**, *154*, A103.

(3) Hatchard, T. D.; Dahn, J. R. *J. Electrochem. Soc.* **2004**, *151*, A838.

(4) Li, J.; Smith, A.; Sanderson, R. J.; Hatchard, T. D.; Dunlap, R. A.; Dahn, J. R. *Journal of the Electrochemical Society* **2009**, *156*, A283.

(5) Danet, J.; Brousse, T.; Rasim, K.; Guyomard, D.; Moreau, P. *Physical Chemistry Chemical Physics* **2010**, *12*, 220.

(6) Key, B.; Bhattacharyya, R.; Morcrette, M.; Seznec, V.; Tarascon, J. M.; Grey, C. P. *Journal of the American Chemical Society* **2009**, *131*, 9239.

(7) Qiu, X.; Thompson, J. W.; Billinge, S. J. L. *J. Appl. Crystallogr.* **2004**, *37*, 678.

(8) Farrow, C. L.; Juhas, P.; Liu, J. W.; Bryndin, D.; Bozin, E. S.; Bloch, J.; Proffen, T.; Billinge, S. J. L. *J. Phys. Condens. Matter* **2007**, *19*, 335219/1.

(9) Carr, H. Y.; Purcell, E. M. *Phys. Rev.* **1954**, *94*, 630.

(10) Chevallier, F.; Letellier, M.; Morcrette, M.; Tarascon, J. M.; Frackowiak, E.; Rouzaud, J. N.; Beguin, F. *Electrochem. Solid-State Lett.* **2003**, *6*, A225.

(11) Li, J.; Christensen, L.; Obrovac, M. N.; Hewitt, K. C.; Dahn, J. R. *J. Electrochem. Soc.* **2008**, *155*, A234.

(12) Jiang, M.; Key, B.; Meng, Y. S.; Grey, C. P. *Chemistry of Materials* **2009**, *21*, 2733.

(13) Yamakawa, N.; Jiang, M.; Key, B.; Grey, C. P. *Journal of the American Chemical Society* **2009**, *131*, 10525.

(14) Breger, J.; Dupre, N.; Chupas, P. J.; Lee, P. L.; Proffen, T.; Parise, J. B.; Grey, C. P. *Journal of the American Chemical Society* **2005**, *127*, 7529.

(15) Breger, J.; Meng, Y. S.; Hinuma, Y.; Kumar, S.; Kang, K.; Shao-Horn, Y.; Ceder, G.; Grey, C. P. *Chemistry of Materials* **2006**, *18*, 4768.

(16) Grey, C. P.; Dupre, N. *Chem. Rev. (Washington, DC, U. S.)* **2004**, *104*, 4493.

(17) Meyer, B. M.; Leifer, N.; Sakamoto, S.; Greenbaum, S. G.; Grey, C. P. *Electrochem. Solid-State Lett.* **2005**, *8*, A145.

(18) Nesper, R. *Prog. Solid State Chem.* **1990**, *20*, 1.

(19) Li, H.; Huang, X.; Chen, L.; Zhou, G.; Zhang, Z.; Yu, D.; Mo, Y. J.; Pei, N. *Solid State Ionics* **2000**, *135*, 181.

(20) Hochgatterer, N. S.; Schweiger, M. R.; Koller, S.; Raimann, P. R.; Woehrle, T.; Wurm, C.; Winter, M. *Electrochem. Solid-State Lett.* **2008**, *11*, A76.

(21) Jamnik, J.; Maier, J. *Phys. Chem. Chem. Phys.* **2003**, *5*, 5215.

(22) Krawietz, T. R.; Murray, D. K.; Haw, J. F. *Journal of Physical Chemistry A* **1998**, *102*, 8779.

(23) Stearns, L. A.; Gryko, J.; Diefenbacher, J.; Ramachandran, G. K.; McMillan, P. F. *Journal of Solid State Chemistry* **2003**, *173*, 251.

(24) Peng, B.; Cheng, F.; Tao, Z.; Chen, J. *J. Chem. Phys.* **2010**, *133*, 034701/1.

Chapter 4

(1) Key, B.; Bhattacharyya, R.; Morcrette, M.; Seznec, V.; Tarascon, J. M.; Grey, C. P. *Journal of the American Chemical Society* **2009**, *131*, 9239.

(2) Obrovac, M. N.; Krause, L. J. *J. Electrochem. Soc.* **2007**, *154*, A103.

(3) Holzapfel, M.; Buqa, H.; Hardwick, L. J.; Hahn, M.; Wuersig, A.; Scheifele, W.; Novak, P.; Koetz, R.; Veit, C.; Petrat, F.-M. *Electrochim. Acta* **2006**, *52*, 973.

(4) Chan, C. K.; Peng, H.; Liu, G.; McIlwrath, K.; Zhang, X. F.; Huggins, R. A.; Cui, Y. *Nat. Nanotechnol.* **2008**, *3*, 31.

(5) Hatchard, T. D.; Dahn, J. R. *J. Electrochem. Soc.* **2004**, *151*, A838.

(6) Qiu, X.; Thompson, J. W.; Billinge, S. J. L. *J. Appl. Crystallogr.* **2004**, *37*, 678.

(7) Farrow, C. L.; Juhas, P.; Liu, J. W.; Bryndin, D.; Bozin, E. S.; Bloch, J.; Proffen, T.; Billinge, S. J. L. *J. Phys. Condens. Matter* **2007**, *19*, 335219/1.

(8) Meyer, B. M.; Leifer, N.; Sakamoto, S.; Greenbaum, S. G.; Grey, C. P. *Electrochem. Solid-State Lett.* **2005**, *8*, A145.

Chapter 5

(1) Armand, M.; Tarascon, J. M. *Nature (London, U. K.)* **2008**, *451*, 652.

(2) Tarascon, J. M.; Armand, M. *Nature* **2001**, *414*, 359.

(3) Epelboin, I.; Froment, M.; Garreau, M.; Thevenin, J.; Warin, D. *Proc. - Electrochem. Soc.* **1980**, *80-4*, 417.

(4) Sannier, L.; Bouchet, R.; Grugeon, S.; Naudin, E.; Vidal, E.; Tarascon, J. M. *J. Power Sources* **2005**, *144*, 231.

(5) Wang, C.; Wang, D. L.; Dai, C. S. *Journal of the Electrochemical Society* **2008**, *155*, A390.

(6) Xu, J. Q.; Yang, J.; NuLi, Y.; Wang, J. L.; Zhang, Z. S. *Journal of Power Sources* **2006**, *160*, 621.

(7) Orsini, F.; Du Pasquier, A.; Beaudoin, B.; Tarascon, J. M.; Trentin, M.; Langenhuizen, N.; De Beer, E.; Notten, P. *J. Power Sources* **1998**, *76*, 19.

(8) Saint, J.; Best, A. S.; Hollenkamp, A. F.; Kerr, J.; Shin, J. H.; Doeff, M. M. *J. Electrochem. Soc.* **2008**, *155*, A172.

(9) Howlett, P. C.; MacFarlane, D. R.; Hollenkamp, A. F. *Electrochemical and Solid State Letters* **2004**, *7*, A97.

(10) Yamaki, J.; Tobishima, S.; Hayashi, K.; Saito, K.; Nemoto, Y.; Arakawa, M. *Journal of Power Sources* **1998**, *74*, 219.

(11) Monroe, C.; Newman, J. *Journal of the Electrochemical Society* **2003**, *150*, A1377.

(12) Chazalviel, J. N. *Phys. Rev. A* **1990**, *42*, 7355.

(13) Key, B.; Bhattacharyya, R.; Morcrette, M.; Seznec, V.; Tarascon, J. M.; Grey, C. P. *Journal of the American Chemical Society* **2009**, *131*, 9239.

(14) Chevallier, F.; Letellier, M.; Morcrette, M.; Tarascon, J. M.; Frackowiak, E.; Rouzaud, J. N.; Beguin, F. *Electrochem. Solid-State Lett.* **2003**, *6*, A225.

(15) Letellier, M.; Chevallier, F.; Morcrette, M. *Carbon* **2007**, *45*, 1025.

(16) Gerald, R. E.; Klingler, R. J.; Sandi, G.; Johnson, C. S.; Scanlon, L. G.; Rathke, J. W. *J. Power Sources* **2000**, *89*, 237.

(17) Kittel, C. *Introduction to Solid State Physics. 5th Ed*, 1976.

(18) Lide, D. R.; Frederikse, H. P. R. *CRC Handbook of Chemistry and Physics, 78th Edition*, 1997.

(19) Chen, H.; Grey, C. P. *Adv. Mater. (Weinheim, Ger.)* **2008**, *20*, 2206.

(20) Lane, G. H.; Best, A. S.; MacFarlane, D. R.; Forsyth, M.; Hollenkamp, A. F. *Electrochimica Acta*, *In Press, Corrected Proof*.

(21) Egashira, M.; Kiyabu, T.; Watanabe, I.; Okada, S.; Yamaki, J. *Electrochemistry* **2003**, *71*, 1114.

(22) Sivakkumar, S. R.; MacFarlane, D. R.; Forsyth, M.; Kim, D. W. *Journal of the Electrochemical Society* **2007**, *154*, A834.

(23) Bhatt, A. I.; Best, A. S.; Huang, J. H.; Hollenkamp, A. F. *Journal of the Electrochemical Society* **2010**, *157*, A66.

(24) Seki, S.; Kobayashi, Y.; Miyashiro, H.; Ohno, Y.; Mita, Y.; Usami, A.; Terada, N.; Watanabe, M. *Electrochemical and Solid State Letters* **2005**, *8*, A577.

(25) Sakaebe, H.; Matsumoto, H. *Electrochemistry Communications* **2003**, *5*, 594.

(26) Slichter, C. P. *Principles of Magnetic Resonance. 2nd Ed*, 1978.

(27) Howlett, P. C.; MacFarlane, D. R.; Hollenkamp, A. F. *Journal of Power Sources* **2003**, *114*, 277.

(28) Kubo, A.; Spaniol, T. P.; Terao, T. *J. Magn. Reson.* **1998**, *133*, 330.